STUDIES OF MOLECULAR MOTIONS BY FLUORESCENCE MICROSCOPY AT SINGLE MOLECULE AND SINGLE FIBER LEVELS

by

JEFFREY J. LANGE

B.S., Truman State University, 2004

AN ABSTRACT OF A DISSERTATION

submitted in partial fulfillment of the requirements for the degree

DOCTOR OF PHILOSOPHY

Department of Chemistry
College of Arts and Sciences

KANSAS STATE UNIVERSITY
Manhattan, Kansas

2009

Abstract

In this dissertation, state-of-the-art fluorescence microscopy techniques are employed to probe unique nanoscale phenomena in poly(dimethylsiloxane) (PDMS) films and on single carbon nanofibers.

In one study, the mobility and physical entrapment of single dye molecules in dry and solvent-loaded PDMS films is explored. Experiments are performed under dry nitrogen and at various levels of isopropyl alcohol (IPA) loading from the vapor phase, as monitored by a PDMS-coated quartz-crystal microbalance. Single molecules are shown to be predominantly immobile under dry conditions and mostly mobile under IPA-saturated conditions. FCS is used to measure the apparent diffusion coefficient, yielding a mean that is virtually independent of IPA loading and sample class. An increase in the population of mobile molecules under high IPA conditions is attributed to the filling of film micropores with solvent, rather than by incorporation of molecularly dispersed solvent into the PDMS.

In a second study, the molecular mobility of both neutral and cationic molecules in cured PDMS films is studied as a function of oligomer extraction. Cross correlation and Bayesian burst analysis methods were used to quantify the populations of fixed and total molecules, respectively. The results show that the total concentration of dye increases with increased oligomer extraction, while the relative populations of fixed and mobile molecules decrease and increase, respectively. These results are relevant to the use of PDMS in microfluidics, nanofiltration and pervaporation membranes and solid phase microextraction fibers.

In a final study, molecular beacons (MBs) were immobilized onto the ends of single, sol-gel encapsulated vertically-alligned carbon nanofibers (VACNFs) attached to a silicon electrode. MB fluorescence was monitored as a function of the potential applied to the VACNF in a three-electrode electrochemical cell. Application of positive potentials attracts the negatively charged backbone of the MB, causing hybridization of the stem and a reduction in beacon fluorescence. Negative potentials cause dehybridization of the stem, and an increase in MB fluorescence. This study presents the first measurement of potential-dependent dehybridization/rehybridization of MBs attached directly to the end of a single VACNF. These studies will help to characterize the mechanism by which future lab-on-a-chip devices will detect harmful bio-organisms.

STUDIES OF MOLECULAR MOTIONS BY FLUORESCENCE MICROSCOPY AT SINGLE MOLECULE AND SINGLE FIBER LEVELS

by

JEFFREY J. LANGE

B.S., Truman State University

A DISSERTATION

submitted in partial fulfillment of the requirements for the degree

DOCTOR OF PHILOSOPHY

Department of Chemistry
College of Arts and Sciences

KANSAS STATE UNIVERSITY
Manhattan, Kansas

2009

Approved by:

Major Professor
Dr. Daniel A. Higgins

Abstract

In this dissertation, state-of-the-art fluorescence microscopy techniques are employed to probe unique nanoscale phenomena in poly(dimethylsiloxane) (PDMS) films and on single carbon nanofibers.

In one study, the mobility and physical entrapment of single dye molecules in dry and solvent-loaded PDMS films is explored. Experiments are performed under dry nitrogen and at various levels of isopropyl alcohol (IPA) loading from the vapor phase, as monitored by a PDMS-coated quartz-crystal microbalance. Single molecules are shown to be predominantly immobile under dry conditions and mostly mobile under IPA-saturated conditions. FCS is used to measure the apparent diffusion coefficient, yielding a mean that is virtually independent of IPA loading and sample class. An increase in the population of mobile molecules under high IPA conditions is attributed to the filling of film micropores with solvent, rather than by incorporation of molecularly dispersed solvent into the PDMS.

In a second study, the molecular mobility of both neutral and cationic molecules in cured PDMS films is studied as a function of oligomer extraction. Cross correlation and Bayesian burst analysis methods were used to quantify the populations of fixed and total molecules, respectively. The results show that the total concentration of dye increases with increased oligomer extraction, while the relative populations of fixed and mobile molecules decrease and increase, respectively. These results are relevant to the use of PDMS in microfluidics, nanofiltration and pervaporation membranes and solid phase microextraction fibers.

In a final study, molecular beacons (MBs) were immobilized onto the ends of single, sol-gel encapsulated vertically-alligned carbon nanofibers (VACNFs) attached to a silicon electrode. MB fluorescence was monitored as a function of the potential applied to the VACNF in a three-

electrode electrochemical cell. Application of positive potentials attracts the negatively charged backbone of the MB, causing hybridization of the stem and a reduction in beacon fluorescence. Negative potentials cause dehybridization of the stem, and an increase in MB fluorescence. This study presents the first measurement of potential-dependent dehybridization/rehybridization of MBs attached directly to the end of a single VACNF. These studies will help to characterize the mechanism by which future lab-on-a-chip devices will detect harmful bio-organisms.

Table of Contents

List of Figures

List of Tables

Acknowledgements

First and foremost I would like to thank Dr. Higgins and Dr. Culbertson for letting me start a new project which combines ideas from both of their specialties. Each of them has provided me with extraordinary guidance and help throughout my Ph.D. work. I would like to thank my family and (Missouri) friends who have remained patient with me while I spent so many years in Kansas pursuing this dream. I would also like to thank Tom Everett. All of the hunting and fishing trips, plus the morning coffee time has really made me enjoy my time in Kansas in and outside the lab. Finally, I would also like to thank Ron Jackson for his machining. He made many key parts for all aspects of the research presented here, which definitely made this research possible.

Dedication

I dedicate this work to my wife Jill. Without her, this would absolutely not be possible.

1 Background and Significance

1.1 Why Single Molecules?

Many researchers have tried to detect single molecules (SM); the question to answer now is why. Is there any information to be gained from detecting single molecules? If chemists deal with chemicals on bulk scale, then why is it necessary to learn about their behavior on a single molecule scale? Given these questions, it is easy for many people to quickly dismiss single molecule research as strictly an academic pursuit that holds no real world value. In many different samples the analytes of interest exist in extremely low concentrations. As the concentration of a species is reduced, at what point are heterogeneities in local environments important? What are the differences between bulk and SM properties of chemicals and will it be important to identify the different types of behavior? As science continues to trend toward lower limits of detection, it will become increasingly important to understand the SM behavior of analytes.

The main reason for studying single molecules is sample heterogeneity. As an example of this, one can consider a bulk fluorescence spectrum of one single fluorophore. Figure 1-1 shows a simulated bulk fluorescence spectrum in black. The obtained spectrum is due to the electronic properties of a fluorophore, mainly the energy gap between the excited and ground states. This electronic phenomenon is directly responsible for the center wavelength of the spectrum. However, the more interesting information about the fluorophore is contained in the peak width. If the spectrum was

acquired from condensed phase experiments, it is likely that there are many different environments found within the sample that are averaged together in a bulk experiment.

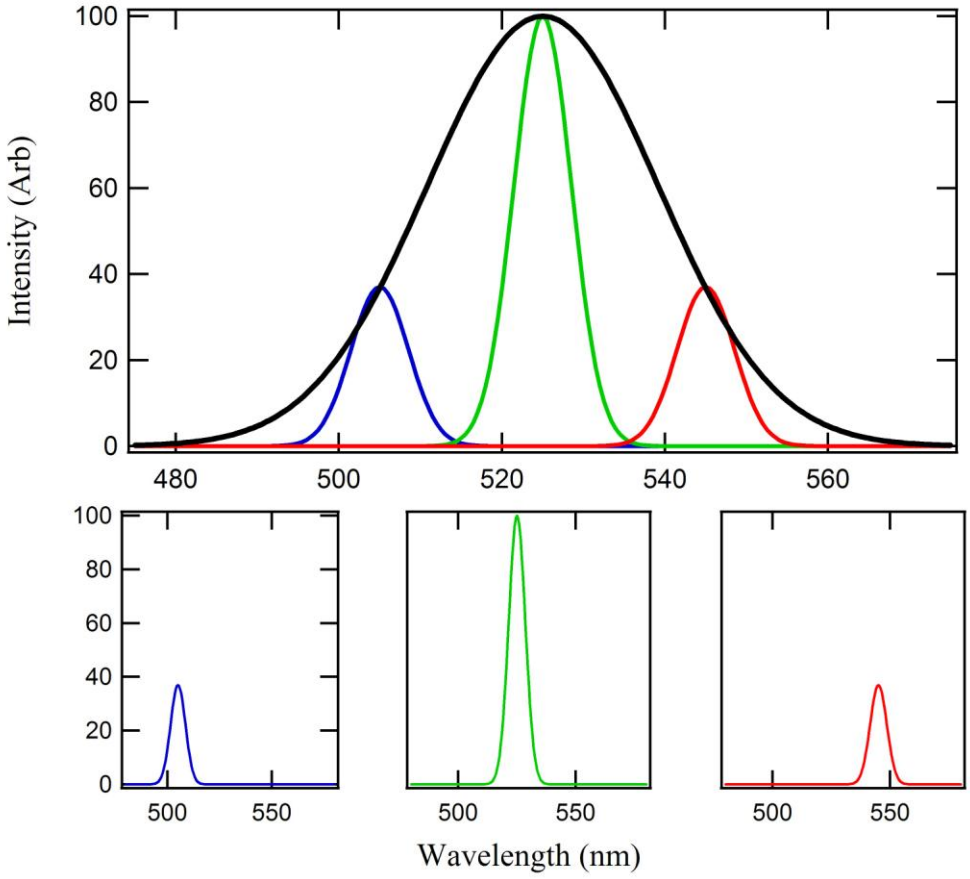

Figure 1-1 Here a diagram illustrating the primary motivation for single molecule research is presented. On top a bulk fluorescence spectrum is shown in black. This spectrum is actually a sum of signals from many different narrow fluorescence spectra from single molecules in different chemical environments. Each of the colored spectra corresponds to chemically identical single molecules. However, the local environment that each chemical resides in is slightly different from the others. The sum of the individual spectra results in the bulk spectrum.

In this case, it is likely that each SM exists in a slightly different chemical environment which results in slightly different spectra. These site specific spectra are shown as the red, green and blue spectra in Figure 1-1. If all of the individual spectra are

added together, the resulting spectrum would be the observed bulk spectrum. How important are these individual spectra? What about the chemical environments is different? Will these differences become important to chemists as the limits of detection for many techniques approach the SM level?

These arguments work well for samples where fluorophores are trapped inside or on solid phase materials. In these cases, the molecules are trapped in a particular chemical environment and are unable to quickly escape that particular environment. It would seem then that SM type experiments are not applicable to solution phase samples. Certainly a particular chemical environment that may occur is transient in the solution phase and has a very short lifetime. These environments then interconvert very quickly and yield the bulk spectrum (black) observed in Figure 1-1. SM methods allow observation of these different environments (blue, green and red spectra, Figure 1-1) without the additional step of having to synchronize all of the molecules to some initial state.[1]

The heterogeneities probed by single molecule methods can be very important in a number of different research areas. The work presented here can be classified as materials research where one hopes to gain information about polymer heterogeneities that other researchers can use to better engineer the materials for use in a variety of applications. However, the implications of SM research are not limited only to polymer films. Other members of our group have studied sol-gel materials for a variety of applications.[2,3] In addition, SM experiments are well suited to understanding the complex behavior of a multitude of biochemical systems.[4] In other applications, scientists have employed SM research to study the exact causes of band broadening in

high pressure liquid chromatography (HPLC).[5] Finally, these techniques are capable of determining the behavior of micro-organism sensing devices (Chapter 5).

1.2 How are Single Molecules Detected?

There are many techniques available that offer the sensitivity required to detect SMs.[6-10] Here, an overview of optical SM methods will be presented. In order to resolve single molecules, it is necessary to accomplish two things; the concentration of the analyte must be reduced and the volume in which the molecule may reside must be small. Reducing the concentration alone is not enough. For example, if one considers a theoretical system consisting of 1 mL of a solution that contains one fluorophore. To probe this volume, light is focused into the solution according to the Abbe diffraction limit (EQ 1-1).[11] Here, λ is the wavelength of excitation (488 nm) and NA is the numerical aperture of the objective (for example 1.3) used to focus the light. According to the equation, the probe volume will correspond to ~6 fL for the parameters shown.

$$s = \frac{0.61\lambda}{NA}$$

EQ 1-1

If one monitors the fluorescence signal over time, assuming no fluorescence contaminants, the probability that the single molecule will be detected in a reasonable time frame is miniscule. There is simply too much space for the molecule to occupy, with a very small fraction of that space being detected. To enhance the probability, it is also necessary to decrease the volume in which the molecule may exist. Consider the system again. This time, reduce the solution volume to ~0.4 pL. This volume corresponds to the volume of a 20x20x1 μm sample slice like the images presented in

Chapter 4. Now the probability that one single molecule will be detected in a reasonable time frame is high. Ultimately, the relationship between the probe volume and sample volume is the most important factor in determining if a SM can be detected in a reasonable time frame. The relationship of the probe volume (vol_{probe}) and sample volume (vol_{sample}) can be described as a ratio of the two (EQ 1-2).

$$\frac{vol_{probe}}{vol_{sample}}$$

EQ 1-2

Here, the smaller the ratio the more improbable it will be to detect one single molecule in a reasonable time. Unfortunately, in many cases, samples will contain much more than one molecule. Because of this, experimentally it is more common to use higher concentrations. The upper limit of useable concentrations is dependent on vol_{probe}. For simplicity in the rest of this discussion we will assume that infinitely thin films are investigated. This will allow us to simplify our probe volume to probe area. For example, if the intermolecular distance is 50 nm, then a large excitation diameter of 200 nm (Figure 1-2 left), like those obtained for high NA objectives according to the diffraction limit, many molecules will be excited simultaneously. On the other hand, a smaller excitation diameter of 20 nm (Figure 1-2 right), which is common for near field scanning optical microscopy (NSOM) discussed in section 1.3.4, will excite far fewer molecules simultaneously. Employing an exceedingly smaller excitation volume will allow higher concentrations to be used in SM experiments.

Alternatively, higher concentrations can be employed with large diameter probe volumes if the volume in which the molecules reside is restricted. This is easy to do if

nanofluidics are employed.[12] Using micromolar type concentrations in conjunction with nanometer sized channels will increase the intermolecular distance to a level (~ 1 μm) which allows for SM detection.

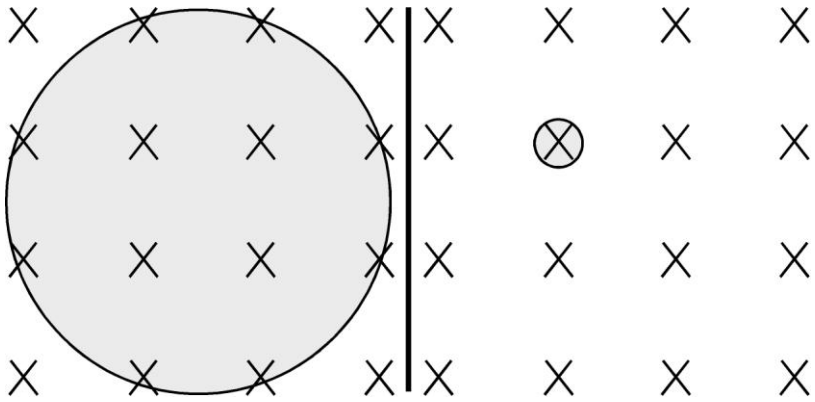

Figure 1-2 Shown here is a diagram illustrating the number of molecules (represented by X's) excited with a 200 nm diameter spot (left) and a 20 nm spot (right), with a constant intermolecular distance of 50 nm.

In addition to the parameters discussed here, a myriad of other instrumental feats are necessary to detect a single molecule. For example, a fluorophore must have a high quantum yield to ensure that many photons are obtained from one molecule. Monochromatic excitation is required to easily isolate the emitted fluorescence from the excitation light. The detection efficiency of an instrument must also be very high, since even the best fluorophores emit only so much light. Finally, the sample matrix in which the fluorophores are contained must be free of contaminants. This last parameter is often the most challenging parameter to fulfill. If all other parameters mentioned in this section are met, SMs may still not be detected because the background may swamp out the fluorescence. It is then necessary to decrease the background emission of the sample matrix to ensure detection of SMs. In most cases the signal of the fluorophore will be

constant and experimentally it cannot be adjusted. The magnitude of the background is the determining factor in obtaining a high signal to background (S/B) ratio. In a practical sense, the only way to improve the S/B, is to reduce the background. Only experimental systems with high S/B will allow for detection of SM. All of these things combine to yield instruments which are capable of SM detection.

1.3 Techniques

There are many techniques available to achieve SM detection. This section describes some of the relevant SM techniques, along with the advantages of each technique and how they can or cannot be applied to the research presented here.

1.3.1 Wide Field Excitation

In many instances, SM investigations are carried out by exciting multiple fluorophores simultaneously. Excitation in these experiments is accomplished through a variety of methods, some of which will be discussed here. The first method of wide field excitation is accomplished by focusing an excitation beam into the back aperture of a high NA objective.[13] The process, shown in Figure 1-3, yields a large excitation spot in the sample.

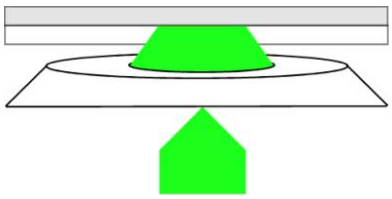

Figure 1-3 Shown here is one method of achieving wide field excitation for SM detection. Excitation is achieved by focusing the excitation beam at the back aperture of the objective.

Fluorescence is then collected back through the objective and sent into a detector. In all wide field experiments, the detector must be an array detector. Since many molecules are excited simultaneously and the fluorescence from all molecules is collected simultaneously, the only way to resolve them is to use a spatially resolved detector. In many cases, electron multiplied charge coupled devices (EM-CCD) are used. Integration times for images are typically on the order of milliseconds or shorter, and are only limited by the sensitivity of the detector. If the detector is very sensitive, the integration time required to detect SMs is very short and thus images can be collected very quickly. Unfortunately, these types of experiments do not allow for depth resolved imaging in thick samples. The excitation beam penetrates and excites fluorophores throughout the entire depth of the sample; therefore, depth resolution is precluded.

1.3.1.1 Total Internal Reflection

Another common method of exciting many fluorophores simultaneously is termed Total Internal Reflection Fluorescence Microscopy (TIRF).[14,15] Figure 1-4 shows a common TIRF set-up. Here a high NA objective is used to send excitation light into a sample mounted onto a substrate, usually a cover slip.

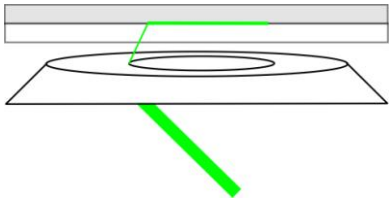

Figure 1-4 This figure shows a typical total internal reflection set-up. The sample (gray) is cast onto a coverslip (white) and excited by an objective. The angle of the excitation beam (green) is modified until total internal reflection is achieved.

The angle of the excitation beam is altered until the beam achieves total internal reflection at the substrate/sample interface. This occurs when the incident angle is greater than the critical angle of the system. At the sample-substrate interface, an evanescent wave is found which extends a short distance (~1 μm) into the sample and is the source of excitation in these experiments. An inherent advantage to TIRF experiments is the depth discrimination they afford. Unlike wide field set-ups like those in section 1.3.1, since the evanescent wave decays quickly away from the sample-substrate interface, sampling extremely thin slices of a thick sample is possible. However, since the evanescent wave exists only at the interface, sampling thin slices from different depths of a sample is impossible.

1.3.1.2 Single particle tracking

Finally, the most important advantage of wide field techniques is their ability to perform single particle tracking (SPT) experiments.[16] Since wide field experiments collect images very quickly, with integration time for fluorescence typically being the limiting factor, movies of molecular motions can be captured. To accurately determine the mean displacement of a single molecule from one frame to another, the diffraction limited fluorescence spot is typically fit to a two-dimensional Gaussian distribution. This fitting routine allows for the determination of the centroid of the single molecule to approximately 10 nm.[1] This process is repeated for each frame in an image sequence until the pixel locations of a particular single molecule are determined throughout the image sequence. Calculating the mean squared displacement of each step of the image sequence, while also accounting for the time between images, allows one to calculate the diffusion coefficient of each single molecule. While this technique is powerful, there are

some important criteria that have to be fulfilled to faithfully track single molecules. The most important criterion is the magnitude of the diffusion coefficient (D). Slow moving single molecules ($D < 10^{-10}$ cm^2/s, depending on the integration time) are easily tracked from one frame of an image sequence to another, because the mean square displacement of the SM from one frame to another is likely small. However, as the D value increases and SMs diffuse more quickly, the mean square displacement of a SM from one frame to another can become quite large. If the displacement is too large, it becomes difficult to be certain that the same molecule is being tracked from one frame to another. In the work presented here, the D values of the diffusing species are too large to allow for SPT experiments with our existing instrumentation.

1.3.2 Confocal microscopy

In contrast to the wide field detection schemes presented above, confocal microscopy collects data using a scanning motion and a single point detector. As pictured in Figure 1-5 a confocal set-up consists of a high NA objective like the ones used in wide field configurations. However, rather than focusing or altering the angle of the excitation beam as it enters the back aperture of the objective, the excitation light is collimated. This set-up yields a diffraction limited focal spot in the sample, according to EQ 1-1. Fluorescence is then collected back through the same objective and through a lens. This lens provides a means of focusing the collected light onto a pinhole which serves as a spatial filter. This process prevents out of focus fluorescence from traveling to the detector. This set-up allows for samples that are thicker than the longitudinal dimension of the focal spot. The depth of focus achieved by the objective in these types of experiments is defined here when the intensity of the beam falls to $1/e^2$ of its initial

value. At this point, the full depth of the spot is estimated by EQ 1-3[17,18], thus yielding information in the z-dimension of the sample. Conversely, this set-up is not necessary for samples that are thinner than the depth of focus.

$$s_{axial} = \frac{1.4\lambda\eta}{NA^2}$$

EQ 1-3

Here, λ is the wavelength of light (488 nm), η is the refractive index of the sample (~1.3) and NA is the numerical aperture of the objective (1.3). For the parameters listed, the axial standard deviation is ~520 nm. Chapter 3 of this dissertation describes experiments on thin samples which do not require the use of a pinhole, while Chapter 4 describes studies of thicker samples where a pinhole is employed.

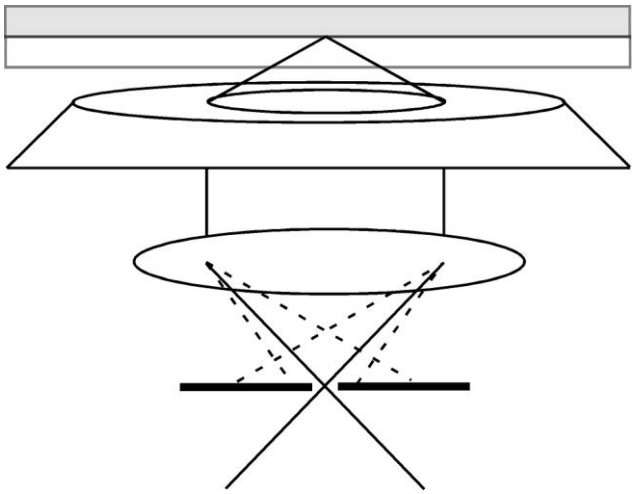

Figure 1-5 This diagram shows a typical confocal set-up. The light collected from the objective is cast through a lens and focused to a point. The in-focus light (solid) passes through the spatial filter, while out of focus light (dashed) is blocked.

Since the focal spot in the sample is diffraction limited, only a small fraction of the image area is excited. To collect an image from a sample, it is necessary to employ a scanning stage. A piezo driven nanopositioning stage is used to scan the sample back and

forth over the excitation region in a raster scanning type motion. Typically, a line of an image is collected by moving the stage in discrete steps. These steps make up the pixels of an image. For much of the work presented here, 200 pixels per line were collected. This simple scanning motion is the major drawback of this type of set-up. Since the sample must be scanned back and forth over the excitation spot, image collection takes a longer time than is typical in wide field experiments. Also, since the scanning time is longer than in wide field type experiments, diffusing species are more difficult to image. Often, the fluorophores diffuse at a rate that is faster than the pixel time of the image. When this happens, streaks appear in an image. Determining a diffusion coefficient for diffusing molecules is difficult in this system and requires the use of different techniques, which will be discussed later (section 1.3.3).

Alternatively, it is possible to scan the excitation beam around the sample and not the sample around the beam as presented above. This type of experiment is called beam-scanning confocal microscopy[19] and is a powerful tool in sample imaging. Typically the excitation beam's angle is altered as it enters the back of the objective to create a raster scanning type motion in the sample. This technique allows for extremely fast (near video rate) sample scanning. However, this technique is not often used in SM experiments because the limiting factor in many SM experiments is the signal level of the fluorophore. An image can be collected at near video rate, but the integration time per pixel is too short to detect the SM.

1.3.3 Fluorescence Correlation Spectroscopy

As discussed above (section 1.3.2) raster scanning type experiments and wide field experiments with quickly diffusing species are often limited in their ability to image

diffusing molecules. Since this is the case, alternative techniques were employed to overcome this obstacle. Fluorescence correlation spectroscopy (FCS), invented in 1974[20], is a technique in which a diffraction-limited laser beam, is focused into a sample, which contains diffusing fluorophores at a low concentration (nM). A diagram of an FCS experiment is shown in Figure 1-6.

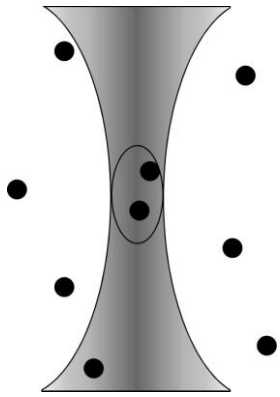

Figure 1-6 Focal volume of a high N.A. microscope objective showing dye molecules (dots) doped into a sample at a single molecule level.

The fluorescence intensity is recorded over time to yield a time transient. An example time transient is shown in Figure 1-7. Fluctuations in the fluorescence intensity result from a Poisson distribution of single molecules that diffuse into and out of the laser beam. The most important experimental factor in these experiments is the fluorophore concentration. It is preferred, but not necessary to ensure that the concentration of analyte molecules is low enough that on average there is less than one molecule in the focal volume at any given time.

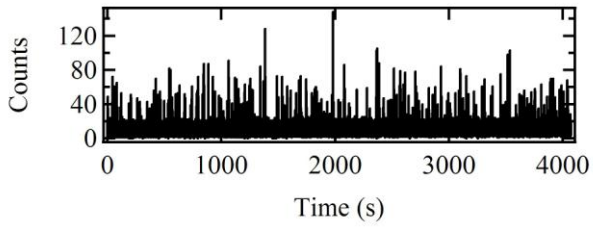

Figure 1-7 Here a time transient obtained from monitoring Poisson distributed fluctuations in a fluorescence signal over time is displayed.

It is necessary to ensure that this is the case, because if more than one molecule is in the focal volume at the same time, it becomes difficult to determine when one molecule leaves or another enters. For example, if a molecule emits 100 counts in a burst as it moves through the focal volume, the shot noise associated with those 100 counts is 10. The molecule is then detected with a signal to noise ratio of 10. These conditions make SM detection very easy. However, if there are 9 molecules in the focal volume, the signal is 900 and the noise is 30. If one molecule enters or leaves the change in signal is 100 and that change is detected with a signal to noise of 3. These conditions make the detection of movement of a SM very difficult.

Data is obtained by recording the fluorescence signal over time with a given integration or bin time. This bin time is also very important to the success of an FCS experiment. Let's consider a group of molecules with diffusion coefficient of $1x10^{-8}$ cm^2/s. Let's also assume that the diffraction-limited focal spot in our sample has a diameter of 200 nm. The time a single molecule will take to diffuse through the excitation volume is calculated by the following equation (EQ 1-4)[20,21].

$$t = \frac{r_o^2}{4D}$$

EQ 1-4

Here r_o is the radius of the focal spot and D is the diffusion coefficient. According to EQ 1-4, it will take approximately 2.5 ms for a molecule to diffuse across the focal spot. If the bin time of the experiment is too large, (anything greater than 500 μs) then the molecule will yield a spike that is only a few pixels wide. Essentially this makes the time transient data useless since the actual molecular processes that are occurring are under sampled. Conversely, if the bin time is very small compared to the diffusion time, then the data is over sampled. This is also detrimental because oversampling will induce extra bit noise into the data while also containing many stretches of time where there are no molecules moving through the detection volume creating excessively large data files.

Once the data is collected, a mathematical process is performed on the time transient. This process is termed an autocorrelation and is shown in EQ 1-5.[21]

$$C(\tau) = \frac{\langle \delta F(t) \cdot \delta F(t+\tau) \rangle}{\langle F(t) \rangle^2}$$

EQ 1-5

Here, the autocorrelation function $C(\tau)$ is the normalized variance of the fluctuating fluorescence signal F(t) at time t, to the signal at time $F(t + \tau)$. This equation transforms the time transient (Figure 1-7) into an autocorrelation decay. A typical decay is shown in Figure 1-8.

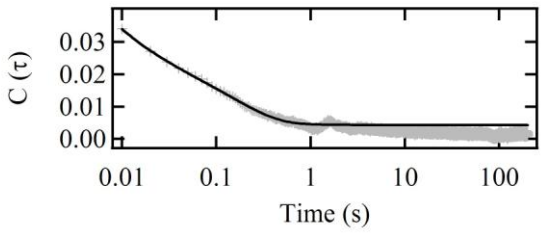

Figure 1-8 Here an autocorrelation decay is shown in gray with a corresponding model fit (black line).

In all actuality the autocorrelation function is complicated and cryptic. A simpler explanation can easily show what the autocorrelation function actually does. If we consider a time transient, like that shown in Figure 1-7, and plot that data versus itself, (consider Figure 1-9) a straight line (Figure 1-9 left) is obtained. This graph represents a perfect correlation between the two data sets, which at this point are identical, and a linear fit to the data has a correlation coefficient of 1. This correlation coefficient makes up the first point of an autocorrelation decay. Data at time t is perfectly correlated to data at time $t + \tau$, where τ is zero. Next, one copy of the data is shifted in time by one data point. The original data is then plotted against itself. Now, there is not a perfect correlation between the data and a spread is obtained (Figure 1-9 middle). Fitting these data to a line yields a correlation coefficient of 0.45. This value is the second point of the autocorrelation decay. This process continues, with every possible shift until every point in the data set has been correlated to every other point in the data set. At longer time shifts like 30 pixels (Figure 1-9 right) low correlation values are obtained. A new graph representing a collection of the correlation values for each shift constitutes an autocorrelation decay.

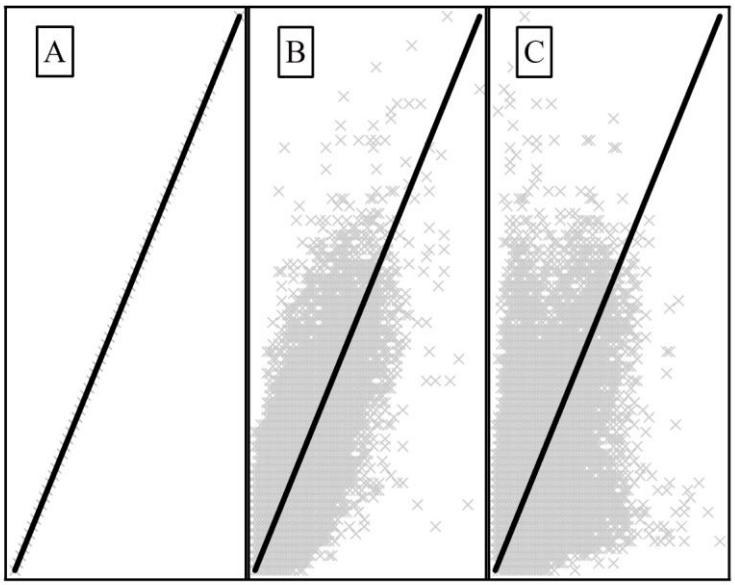

Figure 1-9 This figure shows, in a simplified sense, an autocorrelation. If the raw data is plotted against itself, a straight line is obtained (A). Fitting this data set to a line yields a perfect correlation (ρ=1). This correlation constitutes the first point in an autocorrelation decay. Next, the data set is shifted by one point, and plotted against the original data set a scatter is obtained (B). Fitting this data to a line yields a lower correlation (ρ=0.45). This correlation value then makes the second point in an autocorrelation decay. This process continues for every pixel shift possible. The correlation continues to decrease as shown by a 30 pixel shift plot (C) and corresponding fit, which yields a correlation of (ρ=0.29).

Once an autocorrelation decay (Figure 1-8) is obtained, it can be fit to a number of different models. In our experiments, equations like EQ 1-6[2], employed in Chapter 3, and EQ 1-7[22], employed in Chapter 4, best describe the autocorrelations obtained and allow a number of different molecular parameters to be determined. These equations take into account two and three dimensional diffusion with entrapment, respectively.

$$C(\tau) = \frac{A_d}{1 + D\tau / s^2} + A_e \exp(-\tau k)$$

EQ 1-6

In EQ 1-6 D represents the diffusion coefficient, s is the standard deviation of the focal volume, A_d is the contribution to the autocorrelation amplitude from diffusing species, A_e is the contribution to the autocorrelation amplitude from entrapped species, τ is the time lag or bin time and *k* is the rate constant of desorption.

$$C(\tau) = \frac{A_d}{1 + D\tau/s^2} \frac{1}{\sqrt{1 + D\tau/z^2}} + A_e \exp(-\tau k)$$

EQ 1-7

Here, most of the variables are the same as in EQ 1-6 with the addition of z, which corresponds to the standard deviation of the focal volume in the axial dimension defined by EQ 1-3. Fitting the autocorrelation decay to the appropriate equation will yield diffusion coefficients, and rate constants of desorption among other properties, depending on the equation employed. Many other equations are often employed in the analysis of FCS data, as described in available review articles.[21] It is also worth noting here that FCS becomes inconvenient at some value of D (perhaps 10^{-10} cm^2/s). This is due to the fact that the molecules move at a very slow rate and the length of bursts in a time transient approach the photobleaching time of the molecule. If the molecules start to bleach while in the excitation volume, an apparent D will be calculated which will be significantly different from the actual D. In this case, care must be taken to ensure that the average photobleaching time is not affecting the data. If it is determined that this is the case, then SPT experiments are most likely more appropriate.

1.3.4 Near Field Scanning Optical Microscopy

Another, less common method employed for SM detection is called Near Field Scanning Optical Microscopy (NSOM). This method is used by many researchers to

study a variety of samples.[23-25] It works, as shown in Figure 1-10, by bringing a small light source or tip into the near field (< 10 nm) of the sample. To achieve high resolution, very small probe areas are employed. These types of tips are usually made from fiber optics. The fiber optic is etched or pulled to achieve a very small aperture at the end of the tip.[26] The tip is then coated in metal to ensure total internal reflection inside the fiber and to provide some mechanical stability. Finally a feedback circuit brings the tip into the near field of the sample. Excitation light that is coupled into the fiber excites fluorophores in the sample. The emitted light is collected by a microscope objective positioned directly below the light source (not shown). The sample is then raster-scanned underneath the tip while a feedback circuit keeps the tip in the near field. There are a variety of methods to achieve this, but commonly the feedback circuit responds to topographical features of the sample and keeps the tip within the near field. The feedback information is used to map the topographical information of the sample along with the fluorescence data.

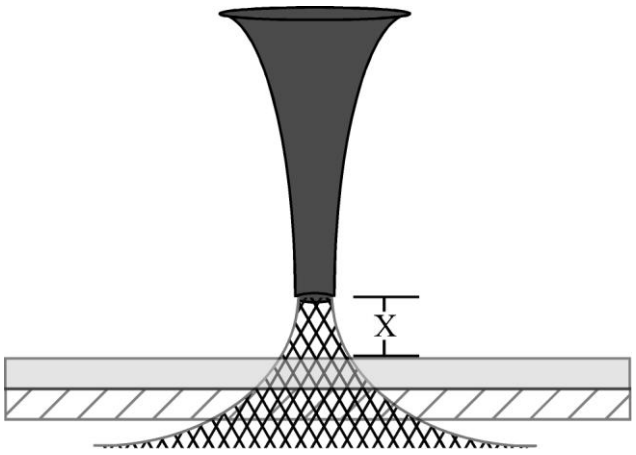

Figure 1-10 Shown here is a diagram of a near field experimental set-up. The tip (dark gray), through which the excitation light is passed (grid pattern), is a fiber

optic coated with metal. The tip is brought to the sample surface (light gray) until it is in the near-field, where X is usually 10 nm or less.

This method is powerful since it has the ability to correlate topography with chemical information from the fluorophores.[25] However, in single molecule research, samples are often very thin and flat to help ensure that the concentrations of analytes are at an acceptable level. This sample property renders the topographical information of the system extraneous. Also, this technique works very well, but is tricky to set-up. Often times, tip fabrication is difficult and tedious but essential to the success of an NSOM experiment. Since the tip is responsible for the achievable resolution, fabrication of a small aperture tip is crucial. While, NSOM is perfectly acceptable for SM investigations, system set-up often prohibits its use.

1.3.5 Super Resolution Techniques

Recent advances in SM techniques employ instrumental set-ups that are distinctly different from any of the apparatus discussed so far. In 1994, Hell et. al. introduced a new technique termed Stimulated Emission Depletion Microscopy (STED).[27] This technique is a far field technique that works to reduce the size of the excitation region. In typical far field experiments like those discussed in section 1.3.2, the size of the diffraction-limited focal spot is governed by the Abbe diffraction limit (EQ 1-1), but a unique combination of multiple lasers can reduce the size of the excited region which is termed the effective spot size. In a typical STED experiment, one laser is passed through a spatial phase modulator, which works to force opposite points of a circular beam to be 180^{o} out of phase with respect to one another. This process yields a doughnut shaped focus. The size of the hole, also called a singularity, in the middle of the doughnut can be

controlled to yield different dimensions. However, the effective spot size can be calculated using EQ 1-8.

$$d \approx \frac{\lambda}{2NA\sqrt{1+I/I_s}}$$

EQ 1-8

Here, λ is the wavelength of the STED beam, NA is the numerical aperture of the objective used, I is the intensity of the doughnut and I_s is the intensity of light needed to deplete half the fluorescence. Increasing I decreases the diameter of the effective spot size, which can be theoretically reduced to molecular scale dimensions. In addition, a second laser beam is overlaid with the STED beam. In order for the two laser beams to yield a sub diffraction-limited focal volume, accurate timing of the beams in the sample is required. First, the diffraction-limited excitation beam is pulsed into the sample to excite molecules from the ground state to the excited state. The STED beam is then pulsed into the sample to cause stimulated emission of many molecules. The length of this pulse is important to these experiments. Typically, the STED beam pulse has duration of only 200 ps, or one tenth of a typical fluorescence lifetime. Any molecule which is contained in the doughnut of the STED beam is forced back to the ground state where they will no longer be able to fluoresce. Finally, fluorescence is collected from the effective spot with all beams turned off. The fluorescence is collected back through the objective and focused onto a single point detector like an avalanche photodiode detector. Raster scanning the sample over the excitation volume builds up an image as in previously discussed techniques.

This technique promises to be very effective for biological applications where fluorophores are usually contained at much higher concentrations than are typically used in SM investigations.[28,29] Unfortunately, the apparatus is complicated which limits its use in many laboratories. Interestingly, the set-up is not much more expensive than a typical single molecule apparatus. The only additional components required for these experiments are an additional laser for use as a STED beam and a spatial phase modulator which can be simple to manufacture.[30]

1.3.6 Quartz crystal microbalance

Finally, a non optical method that provides SM resolution is a quartz crystal microbalance (QCM). Several groups have begun to report SM sensitivity in QCM experiments[31], but typically QCMs are used to measure extremely small (1×10^{-9} g) mass loadings. A QCM consists of an AT cut quartz crystal in which shear vibrations are excited by application of an electrical potential at the appropriate frequency. This potential causes a shear wave in the crystal, which has a specific fundamental frequency. Masses are measured by determining a reduction in the fundamental frequency of the shear wave. The frequency attenuation, Δf, is proportional to a mass change through the Sauerbrey Equation (EQ 1-9)[32].

$$\Delta m = -\frac{\Delta f A \sqrt{\rho_q \mu_q}}{2 f_o^2}$$

EQ 1-9

Here, A is the area of the crystal, ρ_q is the density of quartz, μ_q is the shear modulus of quartz and f_o is the fundamental frequency of the crystal. Films or adsorbates that follow a gravimetric response as calculated using EQ 1-9 must adhere to a strict set

of guidelines. First, the material must be tightly bound to the crystal face. If the material is loosely bound, or just sitting on the face of the crystal, the wavelength of the shear motion could cause the material to shake or roll around the film out of phase with the fundamental frequency. This type of behavior will not allow for mass determinations. Also, the material must be rigid. For example, if a polymer film is attached to the crystal and it is non-rigid, then the top of the polymer film may move independently from the bottom of the film. The entire material must move as a single cohesive unit with the crystal for a gravimetric response to occur.

In the work presented in Chapter 3, the QCM allows for the detection of the amount of solvent loaded into a film. In the past, researchers have investigated systems that had been loaded with solvent vapor but they were unable to determine if the sample was at equilibrium before performing their analyses. Here, a QCM coated with a film that is identical to the one investigated optically, is used to determine not only how much solvent is loaded into a film, but also the time scale over which the sample takes up the solvent. The combination of QCM and SM detection allows investigators to absolutely know the condition of their sample before performing analyses.

1.4 Poly(dimethylsiloxane) History and Motivation

Now that the techniques and some applications of SM detection have been discussed, it is important to provide a background for the research presented here. Here, poly(dimethylsiloxane) or PDMS is investigated using SM methods. This material is important to everyone as it is used for a number of applications. Because of its low cost, flexibility and ability to be cast in a variety of shapes using molds, PDMS has found widespread use in the field of microfluidics. In addition, many environmental chemists

are familiar with PDMS as a membrane through which waste water streams can be purified.[33] PDMS is also employed in solid phase microextraction (SPME) fibers[34] as a material to sample and preconcentrate analytes for further analysis. Finally, it is even used in house construction as silicone caulk. In these applications, the ability of PDMS to absorb and adsorb organic materials makes it ideal for use in some applications, while greatly affecting its use in others.[35] In the research presented here, the goal is to understand the interactions that lead to this behavior.

In order for the properties of PDMS to be tuned to better suit a specific application, the material is often extracted of unreacted low molecular weight oligomers (LMWO). This process takes place by submerging a PDMS device in a highly swelling solvent.[36] Over time, the LMWOs are removed from the bulk of the PDMS. In microfluidics chips, this process makes the PDMS more hydrophilic, which helps to increase the separation performance.[35,37,38] In other applications, such as PDMS stamping[39], the LMWOs are removed to ensure that only the applied "ink" is stamped onto the substrate. Much is known about the bulk effects of extraction on PDMS devices, like an increase in the hydrophilicity of the material, but little is known about how this process effects SM interactions in the bulk and on the surface of the PDMS. The goal then is to understand how this extraction process affects the structure of the resultant PDMS device. In this section, each of the applications mentioned and the suitability of PDMS for these applications will be discussed.

1.4.1 Microfluidics

The field of microfluidics involves using micron scale channels etched or molded into a substrate to perform capillary electrophoresis separations.[40] Commonly,

microfluidics chips (see Figure 1-11) have channels that are several hundred microns wide and a few tens of microns deep. The overall size of the chip is usually on the order of a couple of inches in each dimension. Separations are achieved by filling the channels with aqueous buffer. A separate solution containing the sample dissolved in buffer or a compatible solvent is added to one reservoir (circles). Fluid movement and separations occur via a variety of methods including electrophoresis and pressure-driven flow. In all cases, the molecule surface interactions are important in optimizing the separation. For electrophoretic separations, it is important that the channel walls are hydrophilic in order to carry the surface charge needed for electrophoresis.37 In pressure-driven flow separations, the molecule-wall interactions are the means by which the separation occurs.[41]

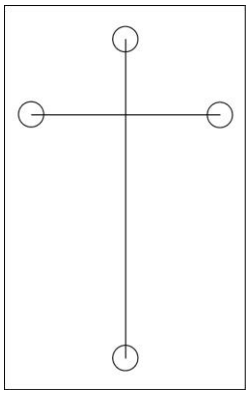

Figure 1-11 This figure shows a simple diagram of a microfluidic chip. The channels (lines) and reservoirs (circles) are usually filled with aqueous buffer. Analyte solutions which are added through a reservoir (right) are injected into a separation channel (cross of chip down) where they are separated by electrophoresis.

Chips are commonly made from glass, however the chemicals involved in etching channels, the high temperatures required to bond the chips and the need for clean environments, make glass an inconvenient material. Ideally, a material suitable for

microfluidics devices should be easily moldable, relatively cheap and still carry enough surface charge to perform well as a microfluidic device. PDMS fulfills these requirements. It is relatively cheap and many papers have been published that show PDMS is a suitable material to achieve high efficiency microfluidic separations.[37,40] However, the absorption and adsorption of organic molecules is a serious drawback.

In a number of recent publications, several authors have discussed the extent to which PDMS absorbs different molecules[22,35,42], their effect on the achievable separations from a device[42] and how it may be possible to block this behavior.[42-44] Unfortunately, a detailed investigation of how molecules are taken up by PDMS has not been published. By understanding the fundamental interactions between single molecules and the PDMS material, other scientists should be able to better engineer PDMS for microfluidics devices. In addition, it is likely that the inclusion of molecules from running buffers or injection plugs will alter the behavior of a chip over time leading to its fouling.[35,42] Increasing the lifetime of PDMS devices by increasing their resistance to uptake of organic molecules will ultimately make PDMS even more cost effective than it already is. Finally, this behavior also restricts the achievable limits of detection for microfluidic devices. Since the bulk of the PDMS chip takes up organic species from any solution it is in contact with, many of the analyte molecules in an injection plug may be lost to the bulk of the material. Obviously, this reduction in throughput of analytes will hurt figures of merit for these devices. Finally, it is necessary to understand these molecule matrix interactions to ensure that this behavior does not bias injections for one type of chemical over another. Since PDMS is a hydrophobic material, nonpolar organic species may absorb more easily into the PDMS than polar species. Understanding the fundamental

interactions between molecules and PDMS will ultimately provide answers to these problems and many more.

1.4.2 Pervaporation

In a completely different application, PDMS is used as pervaporation membranes for a variety of applications[45-47] including contaminant removal from waste water streams.[33] Pervaporation is a process that derives its name from the two steps involved in the associated chemical separation: permeation and evaporation. An apparatus like that shown in Figure 1-12 is employed. One side of a supported PDMS membrane is exposed to an aqueous waste stream.

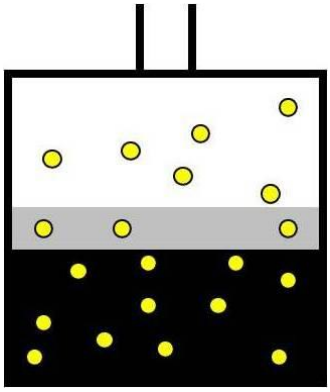

Figure 1-12 This figure shows a pervaporation set-up for fluid purification. A permeable membrane (gray) such as PDMS is exposed to an aqueous feed solution (black) containing some contaminant (circles). A slight vacuum is applied (white) to the other side of the membrane. The contaminants permeate into the membrane and to the vacuum side of the membrane by diffusion. At the other side of the membrane, the contaminants evaporate into the evacuated chamber and are removed. This process leaves a purified aqueous solution on the feed side of the membrane.

This aqueous stream (black) contains some contaminant molecules (circles). The contaminant molecules permeate into the membrane from the aqueous solution. A chemical gradient inside the membrane causes the molecules to migrate to the opposite side of the membrane from which they entered. On this side of the membrane, a slight vacuum is applied (white). As the contaminant molecules migrate to the surface of the PDMS membrane they evaporate into the vacuum and are removed to waste collection. Over time, the aqueous stream is purified. Since the PDMS is hydrophobic, aqueous streams are easily purified of organic contaminants. Ideally, PDMS would be able to quickly and completely remove all contaminants from a waste stream. However, in a practical sense, the PDMS can absorb only a finite amount of organic content at a time, which ultimately limits the speed with which this process can occur. By understanding the fundamental interactions of organic molecules with PDMS a scientific basis for better materials engineering will be provided. Additionally, as with the microfluidics discussion, a membrane may preferentially remove some species from the waste stream while leaving others behind. A better understanding of the full range of possible molecule-matrix interactions will allow for better predictions of membrane properties, and hence a better understanding of pervaporation. Also, examining the effect of LMWO extraction may lead to significant alterations of the PDMS material.

1.4.3 Solid Phase Microextraction

Finally, the last application of PDMS discussed here are solid phase microextraction (SPME) fibers. Typically, syringes like those shown in Figure 1-13 are obtained from any number of vendors. The syringe consists of a tough metal tip, inside which is a fragile fiber that is coated in a material which absorbs organic analytes, in this

case, the material is PDMS. The syringe is first placed into a solution[48] or headspace[49], the fiber is then extended from the metal tip and allowed to equilibrate with the sample for some time.

Figure 1-13 Here, a diagram of a solid phase microextraction syringe is shown. The coating, found on the smallest part of the syringe on the left, can be made of PDMS.

After some time has passed, the fiber is retracted and the whole syringe is removed from the sample. This syringe can then be placed directly into the injector of a gas chromatograph and heated to remove the content. The result is a pre-concentrated plug of analyte. As with pervaporation, the PDMS can absorb a finite amount of material and it can only do so at a given rate. Understanding the interactions of the molecules and material will help to elucidate how SPME sampling occurs. In addition, the PDMS may inherently bias the pre-concentrated plug for non-polar organic species. Finally, the effect of oligomer extraction could be very important to these devices. It is difficult to say whether or not these fibers are extracted during the manufacturing process, since most of the pretreatment steps are trade secrets. It is believed the effects of oligomer extraction on the behavior of these devices may be significant. Understanding the fundamental interactions of PDMS and organic molecules will answer these questions.

1.5 Potential Dependent Dehybridization of Single Stranded DNA

Motivation

The last of the work presented in this dissertation deals with a completely different aspect of fluorescence microscopy and is described in Chapter 5. These

experiments focus on the use of fluorescence to study electrochemical processes occurring at the ends of single carbon nanofibers. Fluorescence microscopy proves to be a powerful tool in understanding the behavior of these processes.

Microfluidics provide a platform through which a variety of analyses can be performed. As discussed above, microfluidic chips can be used for separations of components from a variety of systems, typically consisting of charged molecules. However, the concepts of microfluidic separations can be applied directly to small objects such as beads or even cells.[50] Again, PDMS is an ideal material for these types of studies, especially due to its gas permeability, which allows for manipulation of live cells.[51] In addition, the ability to move cells through a device has become a well known practice. However, detecting the cells remains an area of active research. The goal then is to characterize a new method of cell sensing on microfluidics devices. This research is important, due to the rise in accidental outbreaks of harmful bio-organisms like E. Coli. These outbreaks have caused many people to become ill or, in some cases, die. In addition, the economic impact of an outbreak can be quite significant. One of the most recent outbreaks was an E. Coli outbreak from spinach that caused a loss of 50 – 100 million dollars for the company responsible.[52] In 2001, the USDA estimated that five major foodborne diseases cost the nation at least 6.9 billion dollars each year in productivity losses, medical treatments and premature deaths.[53] It is reasonable to assume that a testing program that can provide early detection of such pathogens, the number of outbreaks and economic losses should at the very least stay constant, if not increase in the near future. Additionally, terrorism is a constant threat in the global community and intentional contamination of our food supply is a possibility. To

minimize the economic losses and health hazards associated with accidental or intentional contamination of the food supply, techniques that detect small amounts (even 10 cells)[54] of bio-organisms must be developed.

The approach developed here is to create a stand-alone lab-on-a-chip device which incorporates many different sample handling and analysis steps. Briefly, foodstuff samples will be loaded onto a microfluidic chip. Sample preparation will first take place followed by two different analysis schemes, which include an immunoassay and a nucleic acid assay. The devices consist of an array of encapsulated vertically aligned carbon nanofibers (VACNFs) which have been functionalized with single stranded DNA (ssDNA) molecules. The ssDNA serves as a selective tether for micro-organism DNA. Applying potentials to the VACNF will dehybridize or unfold the ssDNA so that its exposed bases capture micro-organism DNA. The potentials serve two purposes, they dehybridize the ssDNA functionalized onto the ends of the CNFs and it draws DNA strands from solution down to the electrodes. Understanding the process through which this dehybridization occurs is crucial to ensuring the proper function of the chip. Fluorescence microscopy is employed to characterize the behavior of the ssDNA under different fields and field strengths.

1.6 Chapter 1 References

(1) Moerner, W. E.; Fromm, D. P. *Rev. Sci. Instrum.* **2003**, *74*, 3597-3619.

(2) Fu, Y.; Ye, F.; Sanders, W. G.; Collinson, M. M.; Higgins, D. A. *J. Phys. Chem. B* **2006**, *110*, 9164-9170.

(3) Ye, F.; Higgins, D. A.; Collinson, M. M. *J. Phys. Chem. C* **2007**, *111*, 6772-6780.

(4) Knemeyer, J. P.; Herten, D. P.; Sauer, M. *Anal. Chem.* **2003**, *75*, 2147-2153.

(5) Zhong, Z.; Geng, M. L. *Anal. Chem.* **2007**, *79*, 6709-6717.

(6) Fan, F.-R. F.; Bard, A. J. *Science* **1995**, *267*, 871-874.

(7) Fan, F.-R. F.; Kwak, J.; Bard, A. J. *J. Am. Chem. Soc.* **1996**, *118*, 9669-9675.

(8) Reed, J.; Mishra, B.; Pittenger, B.; Magonov, S.; Troke, J.; Teitell, M. A.; Gimzewski, J. K. *Nanotechnology* **2007**, *18*, 044032-044031;044032-044015.

(9) Kirchhausen, T.; Staunton, D. E.; Springer, T. A. *Journal of Leukocyte Biology* **1993**, *53*.

(10) Xie, X. S.; Dunn, R. C. *Science* **1994**, *265*, 361-364.

(11) Abbe, E. *Archiv. f. Mikr. Anat.* **1873**, *9*.

(12) Foquet, M.; Korlach, J.; Zipfel, W. R.; Webb, W. W.; Craighead, H. G. *Anal. Chem.* **2004**, *76*, 1618-1626.

(13) Schuster, J.; Cichos, F.; von Borzcyskowski, C. *Eur. Polym. J.* **2004**, *40*, 993-999.

(14) Schuster, J.; Cichos, F.; von Borczyskowski, C. *Eur. Phys. J. E: Soft Matter and Biological Physics* **2003**, *12*, S75-S80.

(15) Wayment, J. R.; Harris, J. M. *Anal. Chem.* **2009**, *81*, 336-342.

(16) Dietrich, C.; Yang, B.; Fujiwara, T.; Kusumi, A.; Jacobson, K. *Biophys. J.* **2002**, *82*, 274-284.

(17) Wilson, T.; Sheppard, C. *Theory and Practice of Scanning Optical Microscopy*; Academic Press: New York, 1984.

(18) Spring, K. R.; Fellers, T. J.; Davidson, M. W. *Theory of Confocal Microscopy: Resolution and Contrast in Confocal Microscopy*, http://www.olympusconfocal.com/theory/resolutionintro.html, 2009.

(19) Carlsson, K.; Danielsson, P. E.; Lenz, R.; Liljeborg, A.; Majlbf, L.; Aslund, N. *Optics Letters* **1985**, *10*, 53-55.

(20) Elson, E. L.; Magde, D. *Biopolymers* **1974**, *13*, 1-27.

(21) Schwille, P.; Haustein, E. *Biophysics Textbook Online*.

(22) Lange, J. J.; Culbertson, C. T.; Higgins, D. A. *Anal. Chem.* **2008**, *80*, 9726–9734.

(23) Koopmana, M.; Cambib, A.; Bakkera, B. I. d.; Joostenb, B.; Figdorb, C. G.; Hulsta, N. F. v.; Garcia-Parajo, M. F. *FEBS Lett.* **2004**, *573*, 6–10.

(24) Garcia-Parajo, M. F.; de Bakker, B. I.; Koopman, M.; Cambi, A.; de Lange, F.; Figdor, C. G.; van Hulst, N. F. *NanoBiotechnology* **2005**, *1*, 113-120.

(25) Dunn, R. C. *Chem. Rev.* **1999**, *99*, 2891-2927.

(26) Burgos, P.; Lu, Z.; Ianoul, A.; Hnatovsky, C.; Viriot, M. L.; Johnston, L. J.; Taylor, R. S. *Journal of Microscopy* **2003**, *211*, 37-47.

(27) Hell, S. W.; Wichmann, J. *Optics Letters* **1994**, *19*, 780-782.

(28) Sieber, J. J.; Willig, K. I.; Heintzmann, R.; Hell, S. W.; Lang, T. *Biophysical J.* **2006**, *90*, 2843–2851.

(29) Willig, K. I.; Rizzoli, S. O.; Westphal, V.; Jahn, R.; Hell, S. W. *Nature* **2006**, *440*, 935-939.

(30) Yao, X.; Ito, T.; Higgins, D. A. *Langmuir* **2008**, *24*, 8939-8943.

(31) Wang, J.; Nielsen, P. E.; Jiang, M.; Cai, X.; Fernandes, J. R.; Grant, D. H.; Ozsoz, M.; Beglieter, A.; Mowat, M. *Anal. Chem.* **1997**, *69*, 5200-5202.

(32) Sauerbrey, G. *Z. Phys. A: Hadrons Nucl.* **1959**, *155*, 206-222.

(33) Yeom, C. K.; Kim, H. K.; Rhim, J. W. *J. Appl. Polym. Sci.* **1999**, *73*, 601–611.

(34) Kaur, V.; Malik, A. K.; Verma, N. *J. Sep. Sci.* **2006**, *29*, 333 – 345.

(35) Mukhopadhyay, R. *Anal. Chem* **2007**, *79*, 3248-3253.

(36) Briseno, A. L.; Roberts, M.; Ling, M.-M.; Hyunsik Moon; Nemanick, E. J.; Bao, Z. *JACS* **2006**, *128*, 3880-3881.

(37) Vickers, J. A.; Caulum, M. M.; Henry, C. S. *Anal. Chem.* **2006**, *78*, 7446-7452.

(38) Lee, J. N.; Park, C.; Whitesides, G. M. *Anal. Chem.* **2003**, *75*, 6544-6554.

(39) Deng, T.; Wu, H.; Brittain, S. T.; Whitesides, G. M. *Anal. Chem.* **2000**, *72*, 3176-3180.

(40) McDonald, J. C.; Whitesides, G. M. *Acc. Chem. Res.* **2002**, *35*, 491-499.

(41) Rush, B. M.; Dorfman, K. D.; Brenner, H.; Kim, S. *Ind. Eng. Chem. Res.* **2002**, *41*, 4652-4662.

(42) Toepke, M. W.; Beebe, D. J. *Lab Chip* **2006**, *6*, 1484–1486.

(43) Roman, G. T.; Culbertson, C. T. *Langmuir* **2006**, *22*, 4445-4451.

(44) Roman, G. T.; Hlaus, T.; Bass, K.; Seelhammer, T.; Culbertson, C. T. *Anal. Chem* **2005**, *77*, 1414-1422.

(45) Nguyen, Q. T.; Bendjama, Z.; Clement, R.; Ping, Z. *Phys. Chem. Chem. Phys.* **2000**, *2*, 395-400.

(46) Vane, L. M. *J Chem Technol Biotechnol* **2005**, *80*, 603–629.

(47) Bakhshi, A.; Mohammadi, T.; Aroujalian, A. *J. Appl. Polym. Sci.* **2008**, *107*, 1777-1782.

(48) Akapo, S. O.; McCrea, C. M. *J. Pharm. Biomed. Anal.* **2008**, *47*, 526-534.

(49) Wejnerowska, G.; Gaca, J. *Toxicol. Mech. Methods* **2008**, *18*, 543-550.

(50) Abkarian, M.; Faivre, M.; Stone, H. A. *PNAS* **2006**, *103*, 538-542.

(51) Lee, J. N.; Jiang, X.; Ryan, D.; Whitesides, G. M. *Langmuir* **2004**, *20*, 11684-11691.

(52) Associated Press. In *MSNBC*, 2006.

(53) Dyckman, L. J.; Office, Gen. Acc., Ed., 2001.

(54) Wolter, A.; Niessner, R.; Seidel, M. *Anal. Chem.* **2008**, *80*, 5854–5863.

2 Experimental

2.1 Microscope Set-up

2.1.1 Solvent-Dependent Diffusion and Entrapment-Chapter 3

The single molecule microscope used for all single molecule imaging and spectroscopy experiments discussed in Chapter 3 is shown in Figure 2-1. The system is built upon an inverted epi-illumination microscope (Nikon TE-300). The sample sits atop a closed-loop X,Y-scanning stage (Sifam Instruments) mounted on this microscope. In all experiments, sample excitation was accomplished using light from an argon ion laser (514.5 nm). The laser light was first passed through a 514.5 nm laser line filter to ensure removal of other plasma lines. The light then passed through a polarizer, ½ wave plate and another polarizer, oriented 90^{o} with respect to the first, to control the incident power. The excitation light was subsequently reflected from a dichroic beamsplitter (Chroma Z514RDC) into the back aperture of an oil immersion objective (Nikon Plan Fluor, 1.3 numerical aperture, 100x magnification).

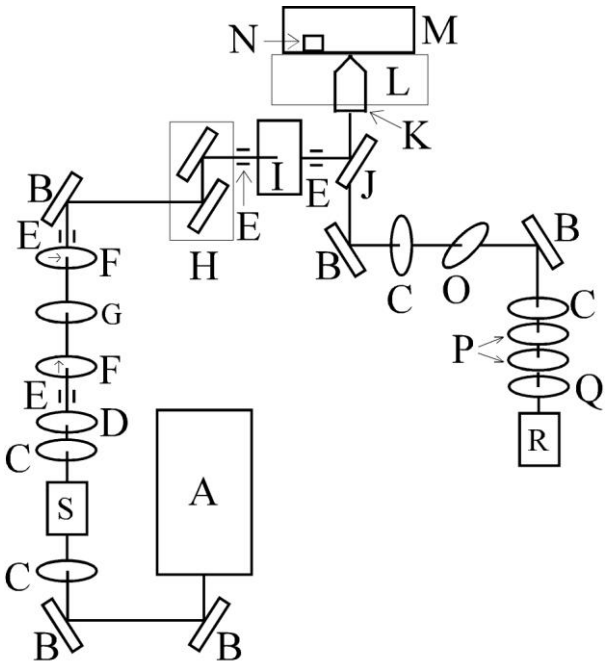

Figure 2-1 Shown here is the microscope set-up used in the solvent dependent diffusion experiments. Laser (A), mirror (B), lens (C), laser line filter (D), aperture (E), polarizer (F), ½ wave plate (G), periscope (H), electronic shutter (I), dichroic beam splitter (J), objective (K), nanopositioning stage (L), Plexiglas chamber (M), quartz crystal microbalance (N), holographic notch (O), 530 nm long pass filter (P), 580-40 bandpass filter (Q), avalanche photodiode detector (R), Pockel's Cell (S).

This objective produced a nearly diffraction limited focus of ≈ 300 nm $1/e^2$ radius in the sample and was also used to collect the resulting single molecule fluorescence. In all experiments, the incident laser power was maintained at 2 μW (estimated from measurements made external to the microscope). An electronic shutter was used to control illumination of the sample. Fluorescence collected from the sample was isolated from the excitation light by passage back through the dichroic beamsplitter, 514.5 nm holographic notch filter, two 530 nm long pass filters, and a 580 nm bandpass filter having a 40 nm passband. The order of the filters here is important. It is necessary to position the holographic notch filter first in order to prevent reflected laser light from

exciting chromophores in the long pass filters and causing emission. A single-photon-counting avalanche photodiode (Perkin-Elmer) was used as the detector. For all experiments except the polarization modulation experiments, the Pockel's Cell was in the beam path, but not turned on.

The same microscope set-up was employed for polarization modulation experiments. These experiments were performed in order to better understand the rotational motions of single molecules entrapped in dry Poly(dimethylsiloxane) (PDMS) films. The Pockel's cell was employed to modulate the excitation polarization through 180^{o} in these experiments. The cell was driven by a waveform generator and an amplifier. The waveform generator was programmed to output a triangle wave with the following parameters: frequency 20 Hz, amplitude 10 V, symmetry 5 % with no offset. These parameters yield a waveform similar to a sawtooth. This was the only way to mimic a spinning half wave plate with the employed function generator. The output was set to drive a 50 Ω load. Using this set-up, fluorescence from a single molecule is collected over time, with modulated excitation. The fluorescence signal is then fit to a sine wave and the phase angle is calculated. The excitation light is polarized, but the detected emission is not. In doing this, molecules are excited and therefore emit light only when the polarization of the excitation light matches the orientation of the transition dipole of the molecule. Slow rotations and molecular flip flops are observed in these samples by gradual changes and large jumps in the phase angle. However, these phenomenon cannot be related to the absolute orientation of the molecule.

2.1.2 Extraction Dependent Uptake of Small Organics-Chapter 4

In order to understand the effects of oligomer extraction in PDMS devices, Chapter 4, the system described above was used with the following changes. In all experiments, sample excitation was accomplished using light from a solid state laser (488 nm). A 488 nm laser line filter was used to ensure the removal of other lines. An appropriate dichroic beamsplitter (Chroma Z505RDC) was employed. The same objective produced a nearly diffraction limited focus of ≈ 300 nm $1/e^2$ radius in the sample. In all experiments, the incident laser power was maintained at 3 μW (estimated from measurements made external to the microscope). Finally, a 488 nm holographic notch filter and a 100 μm pinhole (serving as a spatial filter) were added.

2.1.3 Potential Dependent Dehybridization of ssDNA-Chapter 5

In order to study the electrochemical dehybridization of carbon-nanofiber-supported ssDNA, described in Chapter 5, the microscope described in section 2.1.2 was employed with the following changes. The objective employed was an air objective (Nikon fluor, 0.55 numerical aperture, 50x magnification), which produced a nearly diffraction limited focus of ≈ 540 nm $1/e^2$ radius in the sample. For imaging and time transients, the light also passed through a 535 nm bandpass filter having a 50 nm passband instead of the long pass and bandpass filters mentioned previously. For these experiments the single-photon-counting avalanche photodiode described above was used as the detector. For spectra, the light passed only through the holographic notch filter before entering the spectrograph (Acton Research Corp.) and liquid nitrogen cooled CCD (Princeton Instruments).

2.2 Synthesis of BPPDI

In all PDMS experiments, a neutral organic fluorophore was employed as a probe molecule. The perylene diimide dye, bis-N,N'-(butoxypropyl)-perylene-3,4,9,10-tetracarboxylic diimide (BPPDI) was synthesized following a previously described procedure.[1] All starting materials and solvents were obtained from Aldrich and were used as received. Briefly, BPPDI was synthesized by refluxing *n*-butoxypropylamine with perylene-3,4,9,10-tetracarboxylic dianhydride in a small volume of pyridine. The product was purified by column chromatography using a silica gel stationary phase and a 20:1:0.1 chloroform/ethanol/triethylamine mixture as the mobile phase. The product was verified by ^{1}H NMR. The bulk fluorescence spectrum of BPPDI, obtained from a highly doped PDMS slide in the microscope described in section 2.1.1, is shown in Figure 2-2.

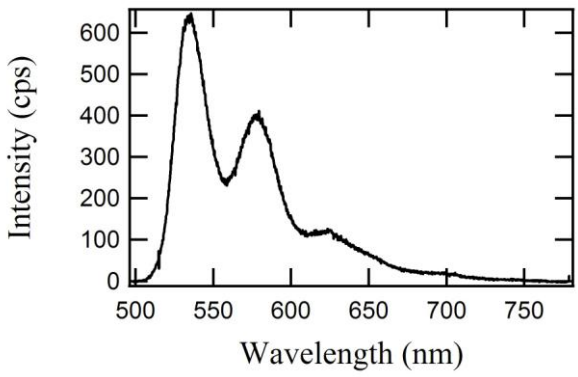

Figure 2-2 Spectrum of BPPDI molecules used in all studies in Chapter 3. This spectra was obtained with the microscope described in section 2.1.1.

2.3 PDMS Sample Preparation

PDMS prepolymer and curing agent were obtained from Dow Corning (Sylgard 184) and were used as received. PDMS was prepared by mixing the prepolymer and curing agent in the prescribed 10:1 ratio. In one pair of studies, we worked to determine

the differences between molecules that were contained near the surface of PDMS films, with those contained throughout the sample depth. In a separate study, we worked to identify molecule matrix interactions of samples that more closely mimic real-world conditions.

2.3.1 Thin films - "On-film Samples"

Thin films containing dye near the PDMS surface were prepared by spin casting the dye on top of the cured PDMS. The details of experiments involving these samples are discussed in Chapter 3. In preparation of these samples, the uncured PDMS mixture was diluted to 3% by weight with hexanes and spin cast (2000 rpm, 2 min) onto air-plasma (Harrick) cleaned (5 min) microscope coverslips (Fisher Premium). The slides were then cured at 80^{o} C for 24 h. Dye was added to these films by spinning (2000 rpm, 30 s) 200 µL of a 10 nM solution of BPPDI in isopropanol (IPA) onto the film. In addition to adding dye to the films, the dye addition step also served to remove contaminants, oligomers and silica from the PDMS films, which was the only way to allow for single molecule experiments. These samples are referred to as "on-film samples" in Chapter 3.

2.3.2 Thin films – "In film Samples"

Thin films containing dye throughout the PDMS were prepared by spin casting a PDMS/dye solution. Results of experiments involving these samples are also discussed in Chapter 3. In preparation of these samples, the uncured PDMS mixture was diluted to 3% by weight with a 0.1 nM solution of BPPDI in hexanes. The solution was spin cast (2000 rpm, 2 min) onto air-plasma (Harrick) cleaned (5 min) microscope coverslips

(Fisher Premium). The slides were then cured at 80^{o} C for 24 h. In order to remove oligomers, silica and contaminants from the film, a spin extraction was employed. This treatment step was identical to that used in preparing the "on film" samples (with the exception of excluding the dye) and was required to achieve the low spot counts (in blanks) necessary for single molecule investigations. Spin extraction was accomplished by spinning off a 200 µL (2000 rpm, 30 s) aliquot of IPA.

2.3.3 Thick films

In a separate study, the effect of extraction on single molecule behavior in PDMS films was examined. Thick samples were prepared to measure molecule-matrix interactions in films that more closely mimic real-world devices. Experiments using these samples are discussed in Chapter 4. In preparation of thick samples, the uncured PDMS mixture was diluted to 26% by weight with hexanes and spin cast (2000 rpm, 2 min) onto air-plasma (Harrick) cleaned (5 min) microscope coverslips (Fisher Premium). The slides were then cured at 80^{o} C for 24 h. Spin extraction was accomplished by spinning off 200 µL (2000 rpm, 30 s) of IPA. This process was repeated 5, 10 and 20 times for "5x", "10x" and "20x" samples. Dye was then added to the films by spinning off a 200 µL (2000 rpm, 30 s) aliquot of a 100 nM BPPDI or 10 nM 9-(2-(ethoxycarbonyl)phenyl)-3,6-bis(ethylamino)-2,7- dimethyl chloride (R6G) solution in IPA. Different concentrations of fluorophore were used in the different sample preparations to achieve similar concentrations in the cured PDMS films.

2.3.4 PDMS Monoliths

In addition to the thick film studies, the effect of extraction was verified in "real world" size PDMS monoliths using bulk spectroscopic methods. Results of experiments using these samples are discussed in Chapter 4. Preparation of these samples was accomplished by pouring the uncured PDMS mixture over a 10 x 10 cm glass plate. The PDMS was then cured at 80 ^{o}C for 24 h. The monolith was then cut into 2.54 cm squares. The monoliths were then placed into a beaker containing IPA. The IPA was continuously stirred during the extraction process. After 15 min, one set (4 pieces) of PDMS monoliths were removed. Fresh IPA was placed in the beaker and stirring continued. After 30 min, another set (4 pieces) of PDMS monoliths were removed. The IPA in the beaker was replaced and stirring continued. Finally, after 1 h total time, the last monoliths were removed from the beaker. The monoliths were placed into an 80 ^{o}C oven for 3 hours. Next, the monoliths were placed into beakers containing a 9 μM aqueous R6G solution. An aqueous solution was employed here to avoid further extraction of the oligomers. R6G was chosen as the probe species because it is water soluble, strongly fluorescent, and, unlike the water soluble species also tested, unlikely to aggregate at the concentrations employed. In addition, R6G is cationic and we sought to ensure that the behavior observed in single molecule experiments found in Chapter 4 also applied to cationic species. The monoliths were submerged for ~18 h. The pieces were then pulled from solution and rinsed with ~ 4mL of clean water on each side. After drying under a N_2 flow, the fluorescence spectra were obtained. Fluorescence spectra obtained from the monoliths, were recorded on a commercial fluorometer (Spex) with excitation at 488 nm and emission collection from 500 - 700 nm. Slits were maintained

at 5 nm each. Data points were collected with a 1 nm emission wavelength increment and 0.1 s integration.

2.3.5 Quartz Crystal Microbalance Preparation

In Chapter 3, the samples prepared were exposed to a nitrogen atmosphere containing varying partial pressures of IPA vapor. In order to understand how much IPA the PDMS films could uptake, a quartz crystal microbalance (QCM) was employed. To make these measurements, the QCM was also coated with a PDMS film. Unfortunately, it was discovered that the quartz discs were significantly rougher than the substrates employed in SM studies. To prepare a surface that more closely approximated that of the substrates, and to which the PDMS film would properly adhere, the quartz discs employed were first coated with a silica film. The silica film was prepared using sol-gel chemistry. The sol, prepared by Fangmao Ye, was prepared by mixing 0.8 mLTetramethoxysilane, 1.6 mL ethanol, 1.6 mL water and 0.32 mL 0.1M HCl (in water). The sol was stirred gently for 30 min. After mixing, the sol was aged for 72 hours. Before spin casting the sol onto a quartz crystal (6 MHz, Leybold Inficon), a small piece of conductive copper tape was attached to the top of the crystal. After the tape was attached the crystal was plasma cleaned. The copper tape was used as an electrode to the top of the crystal. Electrical connection to the quartz crystal could not be achieved if the conductive tape was added after silica/PDMS coating. Next, 86 μL of the sol described above was spin cast onto an air plasma (Harrick) cleaned (5 min) quartz crystal. The coated crystal was then stored in a vacuum desiccator overnight. Finally, a PDMS film was coated onto the sol-gel coated QCM in the same manner as described in Section 2.3.1.

2.4 Ellipsometry

Spectroscopic ellipsometry was used to measure the thickness of the thin films used in Chapter 3. To measure the film thickness, PDMS solutions prepared as in section 2.3.1, except without dye, were cast onto silicon wafers. Ellipsometry data was collected using an α-SE (J.A. Woollam Co., Inc.) spectroscopic ellipsometer. The parameters used for fitting the data are shown in Table 2-1). The bottom layer is simply a silicon substrate. The middle layer is assumed to be a thin layer of SiO_2 with thickness of 1.5 nm. Finally, the top layer is the PDMS layer. The spline model accounts for many different parameters simultaneously, including the refractive index n, and the extinction coefficient k. The resolution of the data fit is adjustable and a sufficient resolution should be used. Too high a resolution and the fitting of the data is extremely slow. Also, the obtained fits do not seem to get better with extremely high resolutions. The optical constant, n is fit to ensure that the data fitting yields a refractive index that is within range of published values for PDMS. Finally, it is necessary to not assume that the film is transparent.

Layer Parameters				General Settings		
Top Layer	Spline	n = 1.47	k = 0	Resolution = 0.05 eV	Fit optical constant, on	Assume Transparent, off
Middle Layer	SiO_2	1.5 nm				
Bottom Layer	SI_Jaw					

Table 2-1 Displayed here are the fit parameters for ellipsometry data analysis. These results are discussed in Chapter 3.

In order to fit the data properly, it was necessary to give good guesses for the film thickness and to let the program fit only one parameter at a time. Such an iterative fitting

procedure was found to be the only way to reduce the mean squared error (MSE) to an acceptable level, while also yielding sensible optical constants. Only fits that had a low MSE and optical parameters that made sense were used. See Figure 3-1 for an example of ellipsometry data and its fit.

2.5 Carbon Nanofiber Array Preparation

All of the chip preparation for studies of the potential dependent dehybridization of ssDNA was performed by Qin Li and Lateef Syed from the Li group. The details of the sample preparation are found below. The results of experiments using these devices are described in Chapter 5.

2.5.1 Metal Catalyst Deposition

The first step in the fabrication of CNF-supported ssDNA involves sputter coating a silicon wafer with chromium and nickel. This was accomplished with a Gatan ion beam sputter coater. Clean silicon wafers were coated with 50 nm of chromium and 22.5 nm of nickel, using an ion beam with an energy of 10.0 keV. The sample was rotated at 35 rpm, tilted at 5^{o} and rocked at a rate of 12 ^{o}/s. This produced a coating rate of 1.2 Å/s for chromium and 0.6 Å/s for nickel.

2.5.2 Carbon Nanofiber Growth

After the metals were deposited, vertically aligned carbon nanofibers (VACNFs) were grown on the coated silicon wafer. Fiber growth was accomplished using an Aixtron Black Magic plasma enhanced chemical vapor deposition (PECVD) system. First, the nickel catalyst coated in the previous step was annealed at 500 ^{o}C for 60s. Then, the wafer was exposed to C_2H_2 and NH_3 with flow rates of 63 and 250 sccm,

respectively. The sample was then heated to 800 ^{o}C while the plasma was started (40 W drive). Once at temperature, fiber growth occurred for 15 min. This process yielded a VACNF array with fiber diameters of 50 – 100 nm and lengths of ~5 μm, as verified by SEM.

2.5.3 SiO_2 Encapsulation

In order to provide mechanical stability to the array and to insulate the fibers, except for the ends, the fibers were coated with SiO_2 using a home built chemical vapor deposition (CVD) system using a tube furnace from Thermo Electron Corporation. After evacuating the chamber to <100 mTorr, the chamber was heated to 715 ^{o}C. Tetraethoxysilane (TEOS) was bled into the chamber at ~400 mTorr. Deposition occurs for 6 h to yield carbon nanofibers that were fully encapsulated in TEOS.

2.5.4 Molecular Beacons

The probe molecules used in these studies are a combination of a fluorophore, a quencher and ssDNA. On the 5' end, a molecule of 9'-(9H)xanthene)-6-carboxylic acid (FAM 6) is attached. On the 3' end, an amide/$(CH_2)_7$ group is present to provide a means to attach the MB to a VACNF. Also on this end, the Dabcyl dT is included as a quencher for the FAM 6. In order to fine tune the dehybridization of the MBs on single VACNFs, several different molecular beacons were used. The loop portions of the different MBs are identical, while the probe regions (underlined portion) contain different numbers of bases. The sequence of each strand is shown in Figure 2-3.

6-FAM-AAGAACAGCAAAGAGCAAGCTTCTT-Dabcyl-dT-AminoC7-3'
6-FAM-AAGAAGAAGACAGCAAAGAGCAAGTCTTCTTCTT-Dabcyl-dT-AminoC7-3'
6-FAM-AAGAAGAAGAAGAAGCAGCAAAGAGCAAGCCTTCTTCTTCTTCTT-Dabcyl-dT-AminoC7-3'

Figure 2-3 Shown here are the sequences of the MB employed in the potential dependent dehybridization studies. The underlined portions indicate the complimentary sections that comprise the stem regions.

Once the VACNF arrays have been prepared, MBs are attached using well-known linking chemistry.[2,3,4] To do this, the silica coated VACNF array is polished with 1 μm alumina particles for 3-4 h. After rinsing with DI water, the chip is chemically etched with 1M NaOH, while applying 1.5 V for ~30 s. This process is necessary to expose the end of the carbon nanofibers. Once this is accomplished, a solution is prepared of 52.2 mM 1-ethyl-3-(3-dimethylaminopropyl) carbodiimide hydrochloride (EDC) and 23.0 mM sulfo-N-hydroxysulfosuccinimide (NHS) dissolved in 0.01 M phosphate buffered saline (1x PBS) containing 0.138 M NaCl, 2.7 mM KCl with pH 7.4. Then, 25 μL of 10 μM MB in PBS was mixed with 25 μL of the PBS/NHS/EDC solution. Functionalization was accomplished by placing this solution on the chip, which was kept in the dark at 40 ^{o}C for 24 hours. Following the functionalization, the chip was rinsed with deionized water. The spectrum of FAM 6 used in these experiments is shown in Figure 2-4. This spectrum was recorded from immobilized FAM 6 labeled ssDNA in a complete device.

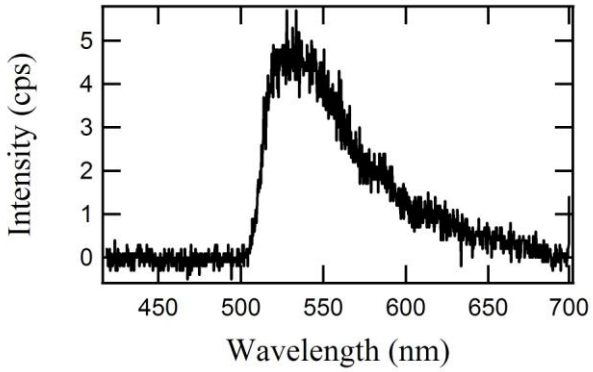

Figure 2-4 Fluorescence Spectrum of the FAM 6 dye used in the potential dependent dehybridization studies. The spectrum shown here was recorded from dye labeled ssDNA functionalized onto a single VACNF.

2.6 Bulk MB Fluorescence and Melting Curves

In order to verify the dehybridization of the MB, melting curves were obtained. A commercial fluorometer (Fluoromax, Spex) was used to monitor the fluorescence of MB while the temperature was changed. Excitation light, centered at 488 nm, and emission slit widths (passbands) were set to 2 nm. Spectra of a 100nM MB solution in 0.2x PBS buffer with 1mM $MgCl_2$ were obtained from 500-800 nm, with 1 nm increment and 0.1 s integration per data point. The temperature was altered using a water bath (Neslab), which was pumped into a home built cuvette holder and water jacketed cuvette. Fluorescence resulting from a temperature range of ~80 ^{o}C (7 ^{o}C to ~85 ^{o}C) were examined.

2.7 Chapter 2 References

(1) Xie, A.; Liu, B.; Hall, J. E.; Barron, S. L.; Higgins, D. A. *Langmuir* **2005**, *21*, 4149-4155.

(2) Wei, F.; Qu, P.; Zhai, L.; Chen, C.; Wang, H.; Zhao, X. S. *Langmuir* **2006**, *22*, 6280-6285.

(3) Wolter, A.; Niessner, R.; Seidel, M. *Anal. Chem.* **2008**, *80*, 5854–5863.

(4) Wei, F.; Sun, B.; Guo, Y.; Zhao, X. S. *Biosens. Bioelectron.* **2003**, *18*, 1157-1163.

3 Single Molecule Studies of Solvent-Dependent Diffusion and Entrapment in Poly(dimethylsiloxane) Thin Films

Published as J.J. Lange, C.T. Culbertson, and D.A. Higgins, *Anal. Chem.* **2008**, 80, 9726-9734.

3.1 Introduction

PDMS materials are now widely employed in microfluidics devices[1] and for patterned transfer (i.e., "stamping) of materials onto a variety of substrates.[2,3] Factors that frequently limit the utility of PDMS in these applications include its microporosity and hydrophobicity, which cause it to readily adsorb and absorb organic compounds.[4-6] In the case of microfluidics, such effects can result in fouling of the device, limiting its useful lifetime. Time dependent changes in the surface charge can also result from uptake of organics, leading to variations in electroosmotic flow.[7] Finally, adsorption of analytes on to the channel wall reduces the analyte concentration and effectively raises the detection limits of PDMS microchips.[5] To overcome such problems, many groups[8,9] have explored methods to block the uptake of organics by PDMS, most notably by modifying the surface with silica to make it more hydrophilic and less permeable to organics.[8-10] Others have explored ways to clean PDMS chips to remove adsorbed molecules.[5]

Conversely, the permeability of PDMS materials to organics can also represent an important advantage in some applications. For example, PDMS membranes are now

being widely employed for the separation and collection of organic vapors from gaseous waste streams.[11] Similar materials are also being used as pervaporation membranes,[12] allowing organic components to be extracted from aqueous solutions. These gas and liquid phase extraction processes are very important from an industrial perspective in that they allow for organic wastes to be recovered and more readily recycled. The ability of PDMS to absorb organics is also utilized in solid phase micro extraction fibers.[13] In these applications, a thin coating of PDMS is cast onto a fiber, which is placed inside a syringe and subsequently used to remove a fraction of adsorbable content from the headspace of a solution,[14] or from the solution itself.[15] The fiber can then be placed into the injection port of a gas chromatograph and heated to remove the absorbed content, thus resulting in a preconcentrated injection from which a quantitative analysis can be performed.

To take full advantage of PDMS materials in these and other applications, a complete understanding of the permeability of PDMS to organics must be obtained. To this end, more complete knowledge of the mechanisms by which organics diffuse through PDMS is required, along with a better understanding of the contributions of molecule-matrix interactions to mass transport processes. PDMS permeability to small organic molecules (i.e., solvents) has been predominantly investigated in the past by bulk methods. For example, the permeability of PDMS membranes can be explored by measuring their mass uptake in concert with the flux of a given solvent through the membrane.[16-21] It has been shown that the diffusion of "good" organic solvents such as chloroform, toluene, and so forth through PDMS follows the expected Fickian behavior and exhibits an increase in the diffusion coefficient with solvent uptake.[16] In contrast, poor solvents and solvent mixtures usually exhibit much more complex behavior

reflective of different solvent-matrix interactions.[16] These latter systems provide clear evidence that heterogeneity is lost in most bulk experiments because only average signals are obtained.

To better probe materials heterogeneity in PDMS and other polymeric materials, researchers have since begun to employ microscopic methods for monitoring diffusion. For example, the Culbertson group employed widefield fluorescence microscopy to monitor the migration of rhodamine 6 g (R6G) into the walls of microfluidic chips formed from both native and silica-modified PDMS.[10] The results clearly demonstrated that R6G uptake could be virtually eliminated by silica modification.

In a quantitative study of R6G diffusion in PDMS films, Santore and Kaufman employed total internal reflection fluorescence methods to monitor dye diffusion normal to the film interface.[22] These authors found that the dye followed a simple Fickian model on short time scales. The diffusivity of the dye in most cases was also found to be smaller in films than in solvent-filled PDMS monoliths. On longer time scales, the behavior observed was found to be more complex because of the presence of a slower diffusional component. It was concluded that this slow component arose from a gradient in the solvent content of the film, with less solvent present near the film/substrate interface. It was also noted that the slower component could result from "diffusion-competitive processes such as gel-dye complexation or dye adsorption onto the glass."[22]

The issues raised in many of the aforementioned studies demonstrate that much remains to be learned about the diffusion of organic molecules through PDMS films. In particular, the actual rate of diffusion through these materials is difficult to determine in the presence of molecule-matrix interactions using bulk techniques alone. Furthermore,

the extent to which molecule-matrix interactions actually occur, their chemical/physical origins, the relevant timescales of these interactions, and the impacts of any incorporated solvents are also frequently unknown. Single molecule imaging and spectroscopic methods[23-25] can be used to directly observe and characterize diffusion phenomena and the effects of molecule-matrix interactions in PDMS films. The methods employed are similar to those used in a number of recent publications from the Higgins group on single molecule studies of sol-gel-derived silica thin films.[25-27] However, to our knowledge, such methods have not yet been implemented in studies of cross-linked PDMS films like those used in microfluidics devices and gas and liquid separations membranes, although they have been employed in investigations of uncured liquid PDMS.[28,29]

In this chapter, single molecule fluorescence imaging and fluorescence correlation spectroscopy (FCS)[23,25] are employed to probe the translational diffusion and entrapment of an uncharged perylene diimide dye (BPPDI) within cured PDMS thin films. Films in which the dye is dispersed throughout the film ("in film" samples) are compared to those in which the dye is predominantly on its surface ("on film" samples). The experiments are performed as a function of film loading by isopropyl alcohol (IPA) from the vapor phase. The extent of IPA loading is followed quantitatively by using a PDMS-coated quartz crystal microbalance. In dry films, the vast majority of molecules are found to be immobile, while under saturated IPA vapor, the molecules are predominantly mobile. A method for counting the spots found in fluorescence images of the samples is used as a means to determine the number of molecules entrapped at fixed locations under each set of conditions. The results show that a nonzero population of fixed molecules exists in all films, even under saturated IPA. Interestingly, the number of immobile molecules also

exhibits a nonlinear dependence upon IPA loading. FCS studies show that the dye diffusion coefficient is largely insensitive to solvent content at all IPA loadings. These same data show that dye molecule mobility is also occasionally interrupted (i.e., the dye molecules briefly become immobile). The FCS analysis shows that the length of these latter events is dependent on the IPA content of the films. The IPA dependence of molecular diffusion and entrapment is interpreted to arise from the filling of PDMS micropores with IPA at high loadings, rather than by solvent-induced swelling of the matrix.[16] The IPA-filled micropores provide a solvent phase that frees the dye molecules from their encapsulating environments and allows them to become mobile.

3.2 Experimental

PDMS prepolymer and curing agent were obtained from Dow Corning (Sylgard 184) and were used as received. PDMS was prepared by mixing the prepolymer and curing agent in the prescribed 10:1 ratio. Two different classes of samples were prepared.

3.2.1 On-film

The uncured PDMS mixture was diluted to 3% by weight with hexanes and spin cast (2000 rpm, 2 min) onto plasma cleaned (5 min) microscope coverslips (Fisher Premium). The slides were then cured at 80^{o} C for 24 h. Dye was added to these films by spinning (2000 rpm, 30 s) 200 µL of a 10 nM solution of BPPDI in IPA onto the film.

3.2.2 In-film

The uncured PDMS mixture was diluted to 3% by weight with a 0.1 nM solution of BPPDI in hexanes and spin cast (2000 rpm, 2 min) onto plasma cleaned (5 min)

microscope coverslips (Fisher Premium). The slides were then cured at 80^{o} C for 24 h. Spin extraction occurred by spinning off a 200 µL (2000 rpm, 30 s) aliquot of IPA. With the exception of dye content, this treatment step was identical to that used in preparing the "on film" samples and was required to achieve the low spot counts (in blanks) necessary for single molecule investigations.

3.2.3 Film Treatment

The spin extraction with IPA serves a similar purpose to the extraction treatments used by other groups to remove low molecular weight oligomers and to make their PDMS materials more hydrophilic.[30] Studies performed on samples treated multiple times showed that a single spin extraction was sufficient for this purpose. All films were stored in a vacuum desiccator until they were used.

3.2.4 Thickness Measurement

Film thickness was determined for films prepared in a similar fashion on silicon substrates. A spectroscopic ellipsometer was employed in this determination; the results yielded a mean PDMS layer thickness of 218(±9) nm. Figure 3-1 shows representative ellipsometry data and the model fit. See chapter 2 for details of the model used to fit the ellipsometry data.

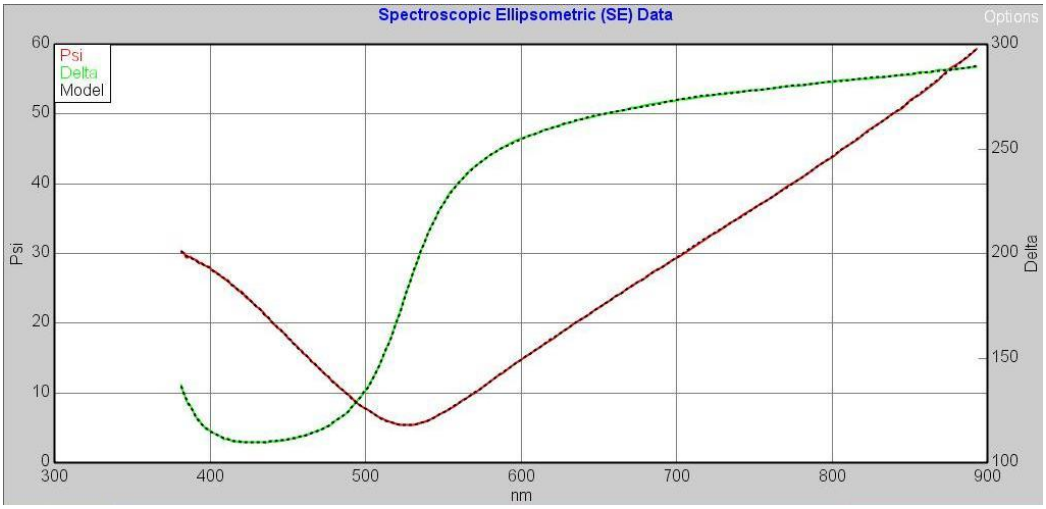

Figure 3-1 Ellipsometry data and model fit

3.2.5 QCM

For the purposes of determining the mass of IPA uptake, PDMS was also coated onto the AT-cut quartz crystals for use with the quartz crystal microbalance (QCM). Gold-coated quartz crystals (6 MHz) were obtained from Leybold Inficon (East Syracuse, NY). Prior to use, the plasma cleaned (5 min) crystals were coated with a ~400 nm thick layer of nonporous silica. This was accomplished by spin casting (6000 rpm, 30 s) the slides with an 85 µL aliquot of an acid-catalyzed tetramethoxysilane-based sol. Preparation of the sol is detailed in Chapter 2. The sols used for spin coating were obtained from Fangmao Ye. The silica film coating was found to be necessary to reduce the roughness of the quartz crystals and enhance adhesion of the PDMS.

3.2.6 BPPDI

The perylene diimide dye, bis-N,N'-(butoxypropyl)-perylene-3,4,9,10-tetracarboxylic diimide (BPPDI) employed was synthesized by others in the Higgins lab following a previously described procedure.[31] All starting materials and solvents were

obtained from Aldrich and were used as received. Briefly, BPPDI was synthesized by refluxing *n*-butoxypropylamine with perylene-3,4,9,10-tetracarboxylic dianhydride in a small volume of pyridine. The product was purified by column chromatography using a silica gel stationary phase and a 20:1:0.1 chloroform/ethanol/triethylamine mixture as the mobile phase. The product was verified by ^{1}H NMR. The structure of BPPDI is shown in Figure 3-2

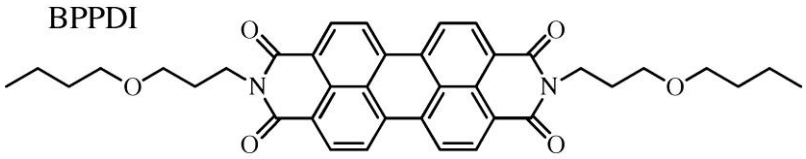

Figure 3-2 The structure of BPPDI

3.3 Imaging

Fluorescence images were acquired by raster scanning the sample above the focused laser spot. A detailed description of the microscope employed and the imaging procedures are given in chapter 2. The fluorescence signal was integrated for 10 ms per pixel in 200 x 200 pixel images of 20 x 20 μm^2 sample regions.

3.4 FCS

Single-point fluorescence time transients for use in fluorescence correlation spectroscopy (FCS) studies were obtained by positioning selected sample regions in the laser focus and recording the spectrally integrated fluorescence in time. Individual transients were recorded for ~ 1 h duration with a dwell time of 10 ms.

3.5 Atmospheric Conditions

All single molecule experiments were performed under controlled atmospheric conditions. In studies of dry PDMS films, the 0.85 L Plexiglas chamber covering the sample was first purged with dry nitrogen (~30 L/h) for a period of ~45 min. Equilibration of the film with the surrounding atmosphere was monitored using the aforementioned QCM (Leybold Inficon) with PDMs-coated quartz crystals. Samples loaded with isopropyl alcohol (IPA) were obtained by purging the Plexiglas enclosure with appropriate mixtures of dry and IPA-saturated nitrogen (~30 L/h) for an equivalent period of time. The nitrogen flow was maintained at a constant rate throughout all experiments.

3.6 Results & Discussion

3.6.1 QCM Measurements of IPA Mass Loading

The frequency shifts observed from PDMS-coated quartz crystals were used to follow loading of the PDMS films when exposed to IPA vapor and to monitor IPA evaporation when the films were exposed to dry nitrogen. The time dependence of the frequency shift was used to ensure the films had reached equilibrium with the surrounding environment prior to performing single molecule experiments.

Interpretation of the QCM frequency shift as a change in film mass during IPA loading or evaporation requires that the QCM response be gravimetric, as described by the Sauerbrey Equation (EQ 3-1).[33]

$$\Delta m = -\frac{\Delta f A \sqrt{\rho_q \mu_q}}{2 f_o^2}$$

EQ 3-1

Here Δf is the change in frequency, A is the area of the quartz crystal, ρ_q is the density of quartz, μ_q is the shear modulus of quartz and f_o is the fundamental frequency of the crystal. This is a reasonable assumption for thin, cross-linked PDMS films. PDMS (specifically cured Sylgard 184) is generally thought of as a rubbery polymer, having a shear modulus of ~1.7 MPa at low frequencies.[34] However, at the relatively high frequencies employed (~6 MHz), the film should exhibit glassy behavior, with a shear modulus closer to that estimated from Brillouin Scattering experiments (i.e., > 100 MPa).[35] In addition, use of the low frequency shear modulus quoted above indicates the film thickness (218 ± 9 nm) is at most 3.4% of the shear wavelength in PDMS. Thus, the films employed are well within the thin-film limit in which a gravimetric response is expected.[36] Unfortunately, because of the different geometric surface areas presented by the relatively rough quartz crystals and smooth glass substrates, the QCM data could only be used to determine relative IPA mass loadings under different conditions. Figure 3-3 depicts a representative time trace observed from a PDMS-coated quartz crystal during IPA loading and subsequent drying. Fitting of each phase of the QCM loading/drying cycle required the use of a double exponential function. The results indicate film loading and drying occur on both short (~1 min) and long (~10 min) time scales with nitrogen flow rates in the ~30 L/h range. Since it takes ~2 min to fully exchange the atmosphere in the 0.85 L sample chamber, it is likely the faster process is limited by this exchange rate. While it is difficult to determine the exact origins of the two timescales observed, these data provide useful information on the time scale for equilibration between the chamber atmosphere and the PDMS film. Because of these results, all PDMS films were

exposed to either dry nitrogen or IPA vapor for at least 45 min prior to beginning single molecule experiments.

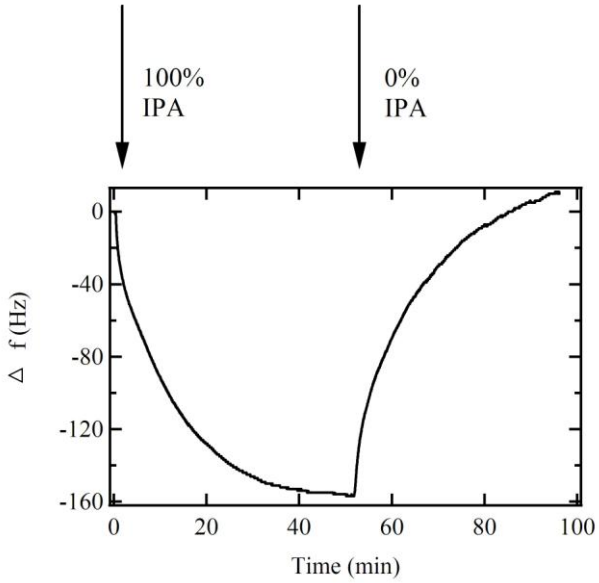

Figure 3-3 Representative QCM trace showing IPA loading, indicated by the decrease in QCM frequency after exposure to IPA-saturated nitrogen, and drying, shown by the increase in QCM frequency after exposure to dry nitrogen

3.6.2 Fluorescence Images

Initial information on the mobility of BPPDI molecules in dry and IPA-loaded PDMS films can be obtained by recording fluorescence images of samples doped to very low (i.e., nanomolar) dye concentrations. Such low concentrations yield well-separated single molecules that can easily be distinguished from each other in the fluorescence images.

Figure 3-4 depicts 20 x 20 μm^2 images obtained from dye-doped "in film" and blank (dye free) samples recorded under equilibrium conditions in dry and IPA-saturated nitrogen environments.

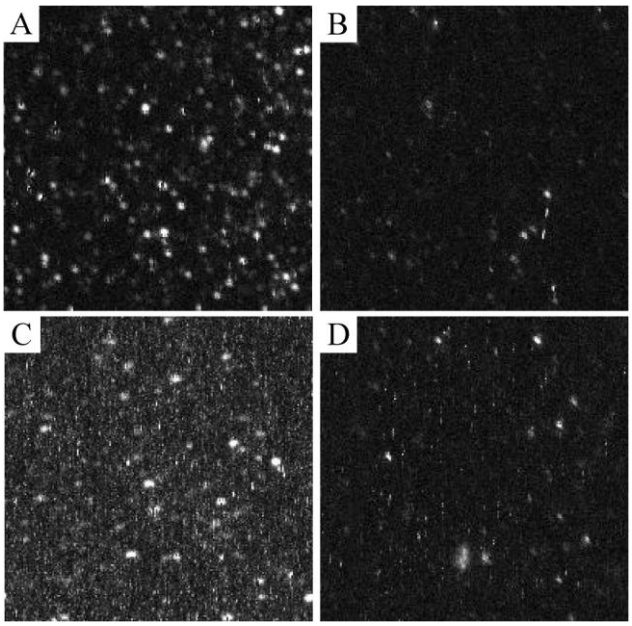

Figure 3-4 (A) Single molecule image showing many fluorescent spots in a dye doped PDMS film under dry nitrogen. (B) A blank (undyed) PDMS film under identical conditions showing significantly fewer spots. (C) A dye doped "in film" sample showing significantly fewer spots and clear image "streaks" under an IPA-saturated atmosphere. (D) a blank under identical conditions showing far fewer spots and streaks. The appearance of streaks in image (C) indicates that the BPPDI molecules are diffusing on a time scale faster than the fast scan axis (vertical on the images) of the system (~2 s/line). All images are plotted on the same intensity scale, with the grayscale depicting a range of 2-102 counts/pixel.

Figure 3-4A and Figure 3-4B show representative images obtained from dry dye-doped and blank samples, respectively. As demonstrated in the image of the dye-doped sample, well-separated, round fluorescent spots exhibiting Gaussian intensity profiles are observed. Virtually indistinguishable images were obtained from dry "on film" samples.

Significantly fewer fluorescent spots are observed from the blank sample, indicating the vast majority (~80%) of spots in dye-doped dry samples are due to emission from BPPDI molecules at the concentrations employed. The sample preparation procedures (see the Experimental section) ensured that the blank counts were as low as possible. Unfortunately, under IPA saturated conditions, up to 50% of the spots observed could be due to impurities (see below).

The appearance of these images (incorporating round fluorescent spots), provides important qualitative evidence that the BPPDI molecules are entrapped in and/or on the dry PDMS films at fixed locations, on the imaging time scale (~2 s/line). Repeated imaging of the same sample region provides further evidence in support of this conclusion, with the majority of spots appearing in identical positions in subsequent images (the time between images is ~7 min).

Under IPA-saturated conditions, the images take on a distinctly different appearance. As shown in Figure 3-4C, far fewer Gaussian spots are observed and a large number of fluorescent "streaks" appear, oriented along the fast-scan direction (vertical on the images). "On film" samples again yield images that are indistinguishable by eye. As with the dry sample, images of blanks (Figure 3-4D) once again yield far fewer spots and streaks, indicating the vast majority of such features in images of dye-doped samples arise from BPPDI fluorescence. As has been previously shown,[37] image streaks are caused by the occasional passage of mobile BPPDI molecules through the detection volume of the microscope as the sample is being scanned. Comparison of the images obtained from dry (Figure 3-4A) and IPA-loaded (Figure 3-4C) samples provides strong evidence that the BPPDI molecules become mobile when the PDMS film is loaded with

IPA. The time transient data discussed below provides additional evidence that the molecules exhibit facile translational diffusion under these latter conditions. Interestingly, it is also clear from these images that some BPPDI molecules remain in fixed locations even under IPA-saturated conditions, as reflected by the presence of round fluorescent spots in the images. Some of these molecules are even found to remain immobile over very long time periods (~40 min) under these conditions. An image sequence depicting the presence of these fixed molecules is provided in Figure 3-5. The entrapment of molecules in fixed locations is discussed further, below.

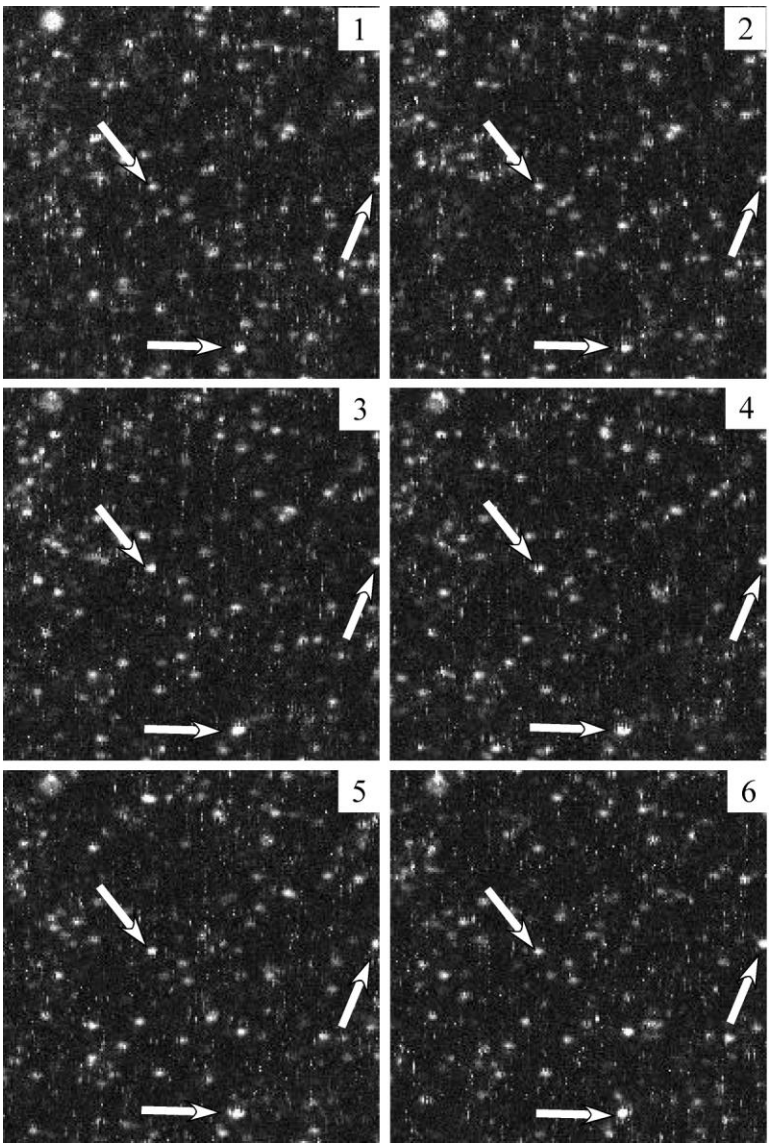

Figure 3-5 An image sequence taken in the same area of a PDMS film under an IPA-saturated atmosphere. Time progresses from image 1 to 6 and covers ~45 min. The arrows show some of the molecules that are immobile over the full length of the image sequence.

3.6.3 Fluorescence Time Transients

Time transients obtained from individual fluorescent spots found in images of the dry dye-doped films provide further evidence the dye molecules are predominantly immobile under these conditions. Figure 3-6 presents representative data.

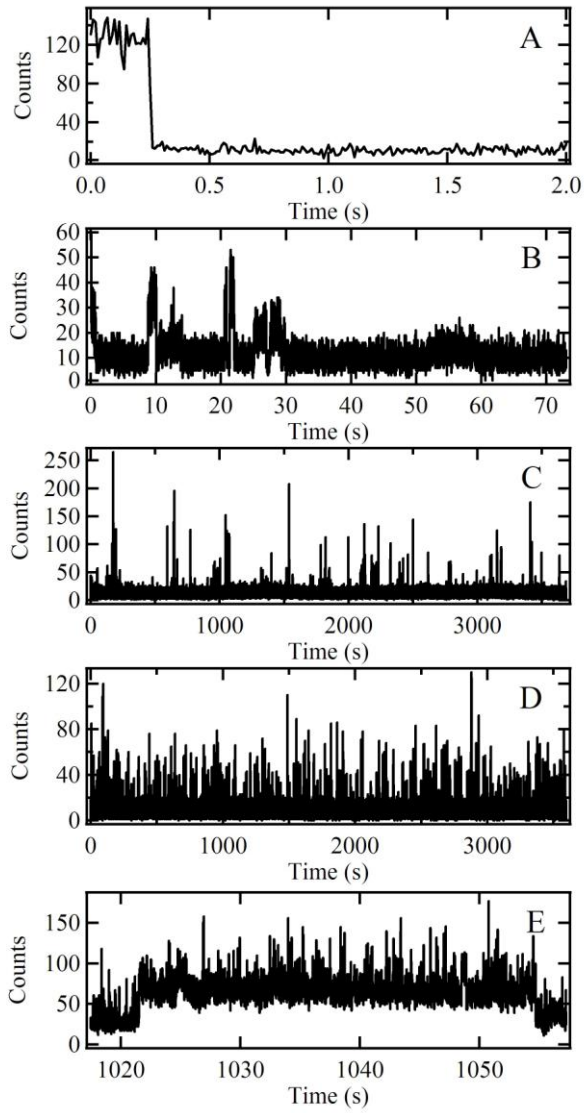

Figure 3-6 Representative time transients for (A) a single fluorescent spot in dry PDMS showing a single molecule bleaching event, (B) a single fluorescent spot in a dry PDMS film with signal fluctuations attributed to reorientation, (C) a single point in a dry PDMS film showing fluorescence bursts attributed to rare single

molecule diffusion, (D) a single point in IPA-saturated PDMS showing fluorescence bursts from BPPDI translational diffusion, and (E) fluorescence during a representative long-term entrapment event (with superimposed diffusive bursts). Such entrapment events were found to be common in these experiments.

As shown in Figure 3-6A, on short time scales, the fluorescence from these spots is frequently found to remain approximately constant (aside from shot noise) for the initial portion of the transient, prior to dropping in a discrete and irreversible transition to the background level. Such observations are consistent with the detection of single molecules entrapped at fixed locations and in fixed orientations in/on the films.

For transients obtained from dry samples over longer periods of time, some evidence of molecular mobility is obtained. Figure 3-6B,C depicts representative transients recorded in just over 1 min and over the course of ~1 h, respectively. These transients show relatively rare bursts of fluorescence above the background level. These bursts may reflect "blinking"[38] behavior from some molecules. The appearance of repeated bursts over much longer periods of time (i.e., Figure 3-6C) suggests that these events may also result from the presence of relatively rare, translationally mobile dye molecules in the films.

Under IPA saturated conditions, the time transients obtained from single points in the PDMS films show clear evidence for translational mobility of the BPPDI molecules. Figure 3-6D depicts a representative transient obtained under such conditions. Comparison of Figure 3-6C and Figure 3-6D demonstrates that there are significantly more fluorescence bursts observed over a similar period of time when the film is loaded with IPA. Importantly, no events clearly attributable to bleaching (as in Figure 3-6A) are observed in such transients. In this case, the bursts are concluded to result almost

exclusively from the passage of different single molecules through the detection volume of the microscope. These results indicate the BPPDI molecules become mobile under IPA saturated conditions and that some dye molecules may be mobile even under dry conditions.

The time transients obtained at high IPA loadings also provide clear evidence for relatively common reversible interruption of dye molecule mobility. While most of the fluorescence bursts produced by diffusing molecules are of relatively short duration (i.e., <<1s), much longer transit time events are also observed in the transients. Figure 3-6E depicts a representative example of such an event in which the signal abruptly rises and remains constant for a period of ~30 s. Fluorescence bursts from diffusing molecules are superimposed on top of this long event. Previous observations of such events in/on silica surfaces have been attributed to reversible molecular adsorption at fixed sites.[26,27,41,42] Here, they are attributed to a more general reversible entrapment of the molecules (see below).

3.6.4 Polarization Modulation

In addition to the single point time transients mentioned above, polarization modulated time transients were also recorded to determine if the molecules are rotating under dry conditions.

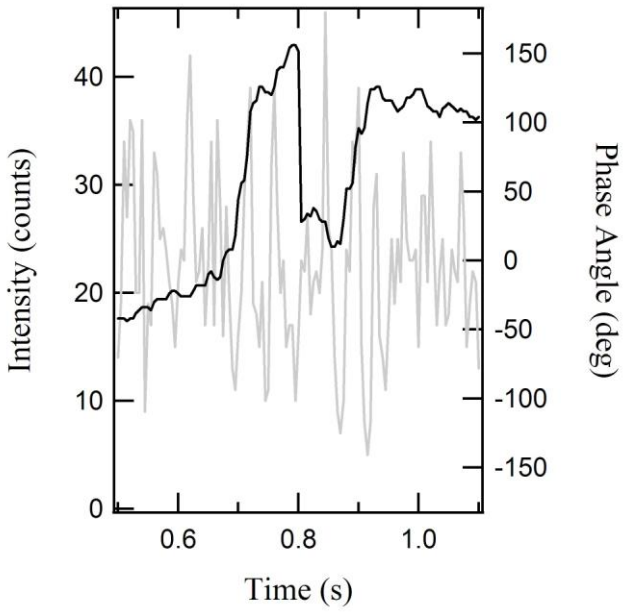

Figure 3-7 Polarization modulation data showing the orientational motion of a single molecule. The fluorescence data in light gray shows an oscillation that corresponds to the frequency of the Pockel Cell modulation (induced by a Pockels cell). Fitting this fluorescence data to a sine wave, allows the calculation of the phase angle (black line) of the fit. Large jumps in the phase angle, correspond to orientational jumps (0.88 - 0.92 s) while portions with continuous changes in phase angle would correspond to slow molecular rotations (0.5 - 0.72 s).

Slow reorientation or orientational jumps of the single molecules are common and have been shown in the literature.[39,40] Single molecule fluorescence data acquired using polarization-modulated incident laser light provided evidence of both. Figure 3-7 shows representative data from these experiments. Experimental details are given in chapter 2.

In the figure, a slow reorientation of the molecule is observed from ~0.5 – 0.72 s, while an orientational jump is observed from ~0.88 – 0.92 s.

3.6.5 Population of Fixed Molecules

The population of immobile BPPDI molecules in the PDMS films was found to exhibit a clear dependence on the level of IPA loading. Again, these fixed molecules are evidenced primarily by the observation of round fluorescent spots in the images. Qualitatively, the number of such spots was observed to decrease with increasing IPA loading. To quantify the numbers of spots observed in each image, an automated template matching routine available with the ImageJ software package was employed.[43] In this procedure, each image was first cross-correlated with a 9 x 9 template comprised of a 2-dimensional Gaussian profile having standard deviation s = 1.6 pixels.[26] A normalized cross-correlation image was obtained, yielding correlation coefficients ranging from -1 (anticorrelated features) to +1 (correlated features). A thresholded version of the cross-correlation image was then used as a means to determine the number of Gaussian spots present. For this purpose, a correlation coefficient threshold of 0.5 was selected (i.e., only those pixels exceeding this value were counted). Furthermore, to be counted as a fluorescent spot, a particular region of interest was required to include 3-30 contiguous pixels exceeding the aforementioned threshold.

Figure 3-8 depicts a representative image obtained from a dry dye-doped PDMS sample and its cross-correlation image. The boxes appended to Figure 3-8B designate the spots counted in the associated raw image (Figure 3-8A).

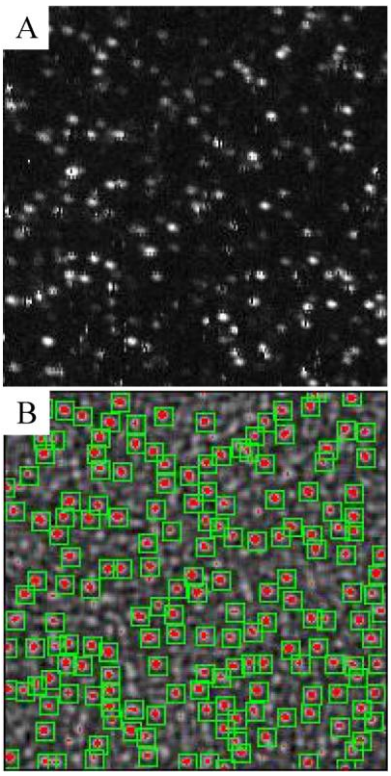

Figure 3-8 (A) Representative raw fluorescence image of a dye-doped PDMS films and (B) cross-correlation image obtained with the ImageJ software[43] depicting regions exceeding the correlation coefficient threshold (0.5) and incorporated from 3 to 30 pixels above threshold. The boxes show all spots that satisfy these criteria. The image is of a 20 x 20 μm^2 sample region.

Tests of the template matching routine performed on simulated images[44] incorporating only diffusing molecules at concentrations similar to those found in the imaging experiments and having similar signal/background ratios yielded spot counts equivalent to ~4% of the actual concentration. In simulations incorporating both fixed and diffusing molecules, the routine yielded mean spot counts identical to the expected values, to

within the Poisson-distributed variations in spot counts expected for finite sample regions. These simulated results indicate that the template matching routine provides an accurate measure of the number of fixed spots in a given image and that it is not significantly biased by false positives resulting from image streaks of other noise.

The dependence of the population of fixed molecules on IPA loading is best depicted by comparing the mean spot densities obtained in images of both dry and IPA-saturated films. Figure 3-9 depicts the results obtained from a series of different samples.

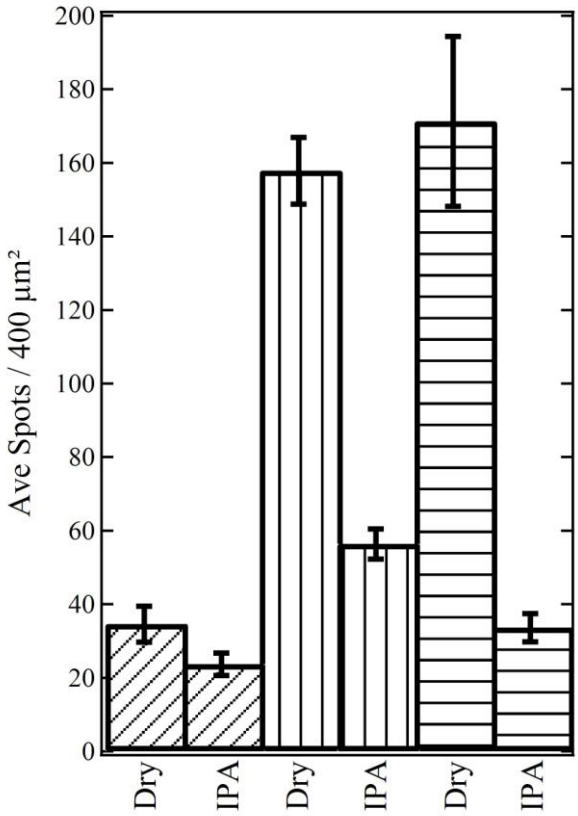

Figure 3-9 Measured spot densities for different samples. Shown are values obtained for blank samples (diagonal pattern), "in film" dye-doped samples (vertical pattern), and "on film" dye-doped samples (horizontal pattern). The error bars depict the 90% confidence intervals on each value, determined from multiple

images in each case. Blank spot counts have not been subtracted from the "in film" and "on film" data.

In these experiments, at least 12 different images of each sample were recorded under dry and IPA-saturated conditions. The images were then analyzed as described above. In all cases, the samples were each subjected to two or three drying and IPA loading cycles. Several general observations can be drawn from these data. First, both "in film" and "on film" samples exhibit spot counts that are statistically much greater than those observed in the blank (diagonal pattern) films. Second, the mean spot count drops dramatically from the dry state upon saturation with IPA for both "in film" (vertical pattern) and "on film" (horizontal pattern) samples. The spot counts under IPA-saturated conditions were found to be statistically independent of the number of drying and IPA loading cycles (Figure 3-10) to which each film was subjected.

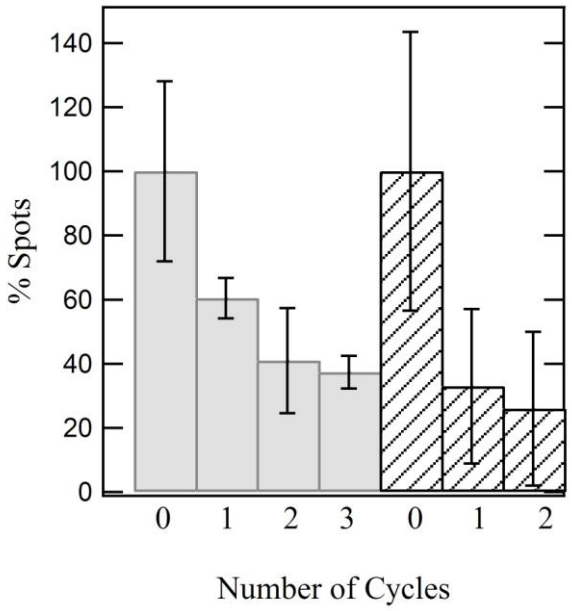

Figure 3-10 Shown here are the % Spots for "in film" (gray bars) and "on film" (diagonal patter) samples. The first bar (0) for each data set is at 0% IPA loading

and each of the next bars (1, 2 etc.) are at successive 100% IPA loadings. The error bars represent the 90% confidence intervals.

Finally, the "in film" samples exhibit statistically greater spot counts under IPA-saturated conditions than do the "on film" samples.

The observation that the dye-doped samples yield greater spot counts than the blanks under most conditions indicates that there is a nonzero population of BPPDI molecules in these films that are entrapped at fixed locations on the imaging time scale. This observation reflects clear molecular scale heterogeneity in the PDMS films and may have any of several different origins. For example, it is possible that the molecules form hydrogen bonds to silanol sites on the silica particles found with the PDMS matrix. The manufacturer's data on Sylgard 184 indicates these materials are 30-60% by weight silica, in the form of silica particles. However, these particles are modified with trimethylsilane groups during the manufacturing process and are believed to be fully passivated. Experiments which will explore the possibility that rare silanol sites are present[41] and participate in hydrogen bonding will be left to future studies. Alternatively, the fixed molecules may be found at the PDMS-glass interface, where they can also form hydrogen bonds with silanol sites on the glass surface. This possibility is discounted because of the large fraction (~24%) of molecules that must then be present at the PDMS/glass interface for the "in film" samples. While preferential partitioning of dye to the PDMS/glass interface is possible, the "on film" results suggest this is not the dominant source of fixed molecules. Were such partitioning to occur, the spot counts for IPA loaded "on film" samples would tend toward the "in film" results as the films were repeatedly dried and reloaded with IPA over the course of hours. No such trend was observed. As proposed previously,[22] it is also possible that there is a gradient in IPA

content within the films, with the lowest IPA concentration occurring near the PDMS/glass interface and the greatest at the PDMS/air interface. While consistent with the observed results, this explanation is deemed unlikely since the "in film" and "on film" results would again be expected to converge in time. Again, no such trend was found in the data. Finally, the molecules may simply be entrapped within small micropores in the PDMS from which they cannot easily escape. These micropores may form around the dye molecules as the PDMS is cured during preparation of the "in film" samples. Deposition of the dye after curing of the PDMS, as is done in preparation of the "on film" samples, would result in fewer such entrapment events. This expectation is consistent with the data obtained (see Figure 3-9). It is therefore concluded that physical entrapment of the dye molecules in PDMS micropores is the cause of molecular immobility.

More detailed studies of the spot counts of a series of intermediate IPA loadings were also performed. Figure 3-11 depicts the relative spot counts observed over the full range of IPA loadings for the two sample types. To better show

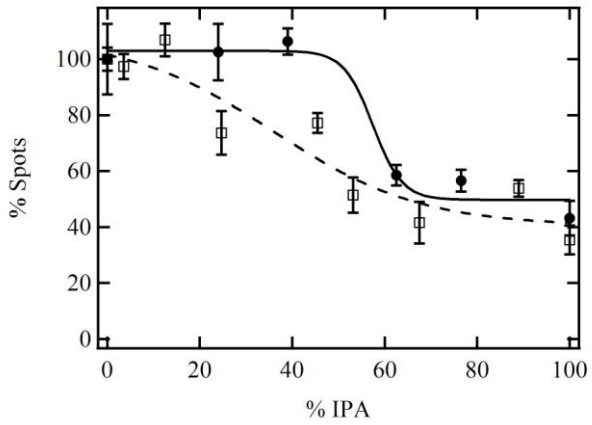

Figure 3-11 Normalized mean spot counts versus IPA loading. Fractional IPA loading values were obtained by QCM measurements, as discussed in the text. The

data appear to show a nonlinear dependence in the spot count on IPA loading, suggestive of a phase transition occurring in the PDMS at intermediate solvent loading. Blank spot counts have not been subtracted. The solid and dashed lines are shown only to better depict the trends in the "on film" (circles) and "in film" (squares) data respectively. The error bars depict the 90% confidence intervals obtained from four replicate images at each IPA loading.

the trend in these data, the spot counts are reported as a percentage of the spot counts observed in similar regions of the same films under dry conditions. Each data point depicts the mean value obtained from four replicate images. As is readily apparent, the spot count decreases as the IPA loading increases. Interestingly, the fraction of fixed molecules appears to decrease nonlinearly with IPA loading, remaining approximately constant at low and high IPA loadings while dropping most rapidly at intermediate values. This observation suggests that something similar to a phase transition may be occurring in the PDMS as it is loaded with IPA.

3.6.6 Molecular Diffusion Coefficients and Mean Entrapment Time

Quantitative data on the rate of molecular motions and the time scales over which the molecules remain entrapped can be obtained from the single point time transients described above. Such information is obtained by autocorrelation of the transients.[45] The correlation functions ($C(\tau)$) obtained provide information on the time scales over which signal fluctuations occur. To obtain quantitative data from the correlation functions, they must be fit to a model that appropriately describes the expected origins of the signal fluctuations. In the present studies, it is clear that the fluctuations could have at least four sources: (i) translational diffusion of single molecules through the microscope detection volume, (ii) occasional entrapment and release of molecules within the detection volume,

(iii) molecular reorientation, and (iv) permanent photobleaching. As a result, the correlation functions obtained were fit to the following model:[27]

$$C(\tau) = \frac{A_d}{1 + D\tau / s^2} + A_e \exp(-\tau k)$$

EQ 3-2

Here, the first term on the right describes dye diffusion in the films and the second term describes molecular entrapment in and release from film micropores, along with any possible reorientation and bleaching dynamics. Within EQ 3-2, D represents the diffusion coefficient for the dye, s^2 defines the excitation area (2.6×10^{-10} cm^2),[26] and *k* represents the combined rate constant for fluctuations due to release of entrapped species, as well as bleaching and reorientation. Finally, A_d and A_e are the amplitudes of the two components of the decay. A representative time transient, its autocorrelation, and its fit to eq 3-1 are shown in Figure 3-12.

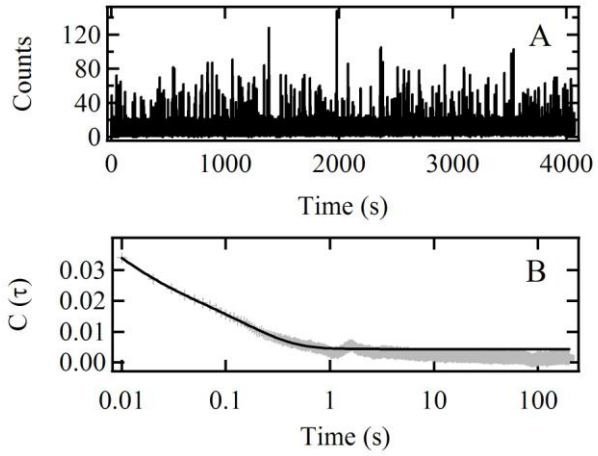

Figure 3-12 (A) A representative time transient and (B) its autocorrelation (data points) and fit to (solid line) Eqn. 1.

Autocorrelation results obtained from the full range of IPA loadings (dry to saturated) yield diffusion coefficients (D) that are statistically indistinguishable from each other. The average D obtained is 1.4(±0.4) x 10^{-8} cm^2/s. The average fluctuation time associated with the exponential component was determined to be 6 ± 4 s under dry nitrogen and 1.1 ± 0.6 s for 100% IPA loading. Bleaching, reorientation, and trap escape are difficult to conclusively distinguish in single molecule time transients. While widefield imaging may be better suited to differentiating bleaching events from trap escape, such methods were not employed because dye motion was too rapid to faithfully track using our available instrumentation. Nevertheless, the average bleaching time was obtained in bulk experiments (at higher BPPDI concentrations). Exhibiting a complex nonexponential decay, the results obtained in dry PDMS films yielded average photobleaching times of 80 ± 20 s. These results suggest that, on average, bleaching does not significantly bias the results obtained. However, molecular reorientation within individual trap sites may still be a factor. As a result, it is concluded that 6 and 1.1 s represent lower limits for the entrapment time.

The lack of a dependence of D on IPA loading may have several origins. It is possible that the change in D from dry to IPA saturated conditions is simply too small to detect in these experiments. If IPA loading results exclusively in swelling of the film, the relatively small quantity of solvent in the film may only produce a small change in the mobility of the PDMS chains (i.e., the local viscosity), and hence, a small change in dye mobility. Alternatively, dye mobility may instead be facilitated by the filling of film micropores (i.e., open volume) with solvent.[16] In that case, translational diffusion would involve movement of molecules through a confining matrix of relatively constant solvent

composition, and D would not change much with solvent loading. This latter model is supported by previously published bulk studies of diffusion in PDMS materials in which it has been observed that the rate of self-diffusion for relatively poor solvents (i.e., alcohols similar to IPA) is only marginally dependent upon solvent loading.[16] Interestingly, the diffusion coefficients measured in this previous work were actually concluded to decrease slightly with increasing solvent content for poor solvents.[16] This apparently anomalous solvent dependence was concluded to result from the filling of film micropores by solvent "clusters", with little associated change in the viscosity of the PDMS matrix because of swelling by molecularly dispersed solvent. Indeed, ellipsometric measurements performed on the present PDMS samples under dry and IPA-saturated conditions showed no detectable differences in film thickness to within the ~10% experimental error, indicating little swelling of the PDMS occurs.

The decrease in the average molecular entrapment time with increasing film IPA content may also be explained by the above model. At low concentrations of IPA, few solvent-filled micropores are present. Although the solvent filling these micropores is mobile, there is a low probability that any particular molecule will be near a solvent-filled pore at any instant in time. Hence, there is little chance it will be released and become mobile. At high IPA loadings, solvent-filled micropores are present in much greater numbers. As a result, the dye molecules spend a proportionately shorter time entrapped in "dry" pores and more time migrating through the film.

3.6.7 Model for Diffusion and Entrapment in PDMS Films

Figure 3-13 presents a model for the dry and solvent filled PDMS matrix, developed based on the experimental observations and interpretations described above.

At all IPA loadings, a nonzero fraction of single molecules in the film are physically entrapped inside at least a few film micropores. These pores are believed to arise from the random clustering of PDMS chains, forming a film of variable PDMS density, on molecule length scales.

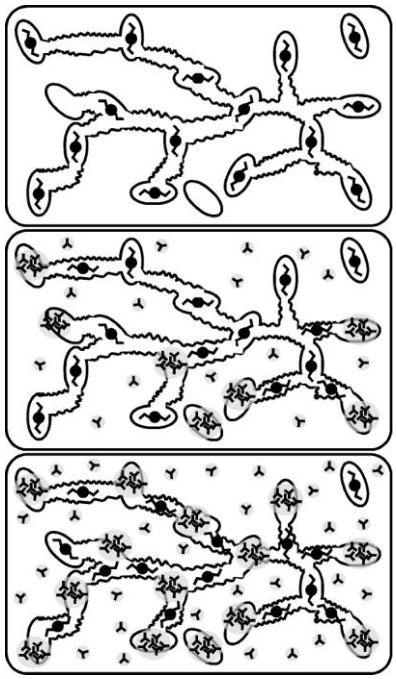

Figure 3-13 Model for PDMS film micropores. In the top panel, the PDMS film is shown under dry nitrogen. The dye molecules are physically entrapped in dry micropores that originate from the random clustering of PDSM polymer chains. In the middle panel, the film is shown under low-intermediate IPA loadings. At low loading, the IPA is dispersed throughout the matrix as isolated solvent molecules and has little impact on film properties and dye mobility. At intermediate loadings, the solvent molecules begin to condense within the micropores, filling them with solvent and freeing some dye molecules, while others remain entrapped. The bottom panel depicts the filling of most film pores at 100% IPA loading. Under these conditions, most of the molecules are free to move through the micropores and interconnecting channels found within the film.

In dry films, (Figure 3-13, top) the BPPDI molecules are physically entrapped in predominantly dry pores and are immobile, yielding images like those shown in Figure 3-4A, where many round spots and few streaks are observed. At low IPA loadings, (Figure 3-13, middle) the IPA enters the PDMS film as molecularly dispersed IPA molecules, having little impact on the mobility of BPPDI. As the IPA content increases further, the solvent molecules condense and IPA-filled pores[16] begin to form (also Figure 3-13, middle), which results in formation of something akin to a two-phase system with separate IPA and PDMS domains. At this point, some of the BPPDI molecules are released from their encapsulating pores and become mobile, diffusing through any solvent-filled channels to neighboring pores. Occasionally, they become briefly entrapped in the pores as the solvent migrates at a greater rate than the dye. Finally, at high IPA loadings (Figure 3-13, bottom), the film micropores and interconnecting channels are largely filled with solvent and even more molecules are freed, leading to a dramatically increased population of diffusing BPPDI molecules. It is important to note that not all molecules may be able to escape their encapsulating pores, even if those pores are solvated. For example, some pores (Figure 3-13, bottom panel, top right pore) may not be connected to others, providing no path for the molecule to escape. The appearance of fixed molecules, even at 100% IPA loading (see Figure 3-5) is consistent with the presence of such isolated pores, as is the greater population of fixed molecules found in the "in film" samples.

Interestingly, the molecules in the "in film" and "on film" samples become mobile over different ranges of IPA loading (compare traces in Figure 3-11). While we continue to study this phenomenon, we believe it arises from differences in the nature of

the occupied pores in these samples. The molecules in "on film" samples are likely entrapped in larger pores found near the film surface. Molecules entrapped in the "in film" samples likely occupy pores having a broader range of sizes and different solvent accessibilities. A broader transition range is observed in Figure 3-11 (dashed line) because IPA condensation occurs at different IPA loadings in the range of pores probed.

3.6.8 Conclusions

Single molecule imaging and single point fluorescence time transient measurements have been used to characterize the diffusion and entrapment of the uncharged dye BPPDI in cured PDMS films under dry and IPA loaded conditions. The results show that the population of mobile BPPDI molecules is strongly dependent upon IPA loading but that the rate of molecular motions, as reflected in the diffusion coefficients obtained, is not. Furthermore, a nonzero population of immobile molecules is found in the films even at the highest IPA loadings. The population of immobile molecules is also shown to depend upon whether the dye was originally cast with the PDMS precursor, prior to curing or added to the film after curing. These observations are attributed to physical entrapment of the dye within PDMS film micropores under dry conditions. Dye mobility at intermediate and high IPA loadings results not from a solvent-induced decrease in PDMS film viscosity but rather from the formation of solvent-filled micropores. However, even under IPA saturated conditions, some BPPDI molecules are found to be immobile, reflecting the presence of some isolated micropores within the PDMS.

The results obtained provide a better understanding of how dye molecules move through and interact with the PDMS matrix. Along with the methods employed, they

promise to aid in the development of PDMS chips for microfluidic separations, PDMS membranes for vapor phase extraction and pervaporation processes, and PDMS fibers for solid phase microextraction. Future work will include exploration of ionic interactions between charged molecules with the PDMS matrix and investigation of ways in which to block the adsorption of small organics, perhaps by filling the open pore volume of the matrix.

3.7 Chapter 3 References

(1) McDonald, J. C.; Whitesides, G. M. *Acc. Chem. Res.* **2002**, *35*, 491-499.

(2) Kumar, A.; Whitesides, G. M. *Appl. Phys. Lett.* **1993**, *63*, 2002-2004.

(3) Deng, T.; Wu, H.; Brittain, S. T.; Whitesides, G. M. *Anal. Chem.* **2000**, *72*, 3176-3180.

(4) Lee, J. N.; Park, C.; Whitesides, G. M. *Anal. Chem.* **2003**, *75*, 6544-6554.

(5) Toepke, M. W.; Beebe, D. J. *Lab Chip* **2006**, *6*, 1484–1486.

(6) Mukhopadhyay, R. *Anal. Chem.* **2007**, *79*, 3248-3253.

(7) Liu, Y.; Fanguy, J. C.; Bledsoe, J. M.; Henry, C. S. *Anal. Chem.* **2000**, *72*, 5939-5944.

(8) Roman, G. T.; Culbertson, C. T. *Langmuir* **2006**, *22*, 4445-4451.

(9) Abate, A. R.; Lee, D.; Do, T.; Holtze, C.; Weitz, D. A. *Lab Chip* **2008**, *8*, 516–518.

(10) Roman, G. T.; Hlaus, T.; Bass, K.; Seelhammer, T.; Culbertson, C. T. *Anal. Chem.* **2005**, *77*, 1414-1422.

(11) Merkel, T. C.; Bondar, V. I.; Nagai, K.; Freeman, B. D.; Pinnau, I. *J. Polym. Sci., Part B:Polym. Phys.* **2000**, *38*, 415-434.

(12) Yahaya, G. O. *J. Membr. Sci.* **2008**, *319*, 82-90.

(13) Kaur, V.; Malik, A. K.; Verma, N. *J. Sep. Sci.* **2006**, *29*, 333 – 345.

(14) Wejnerowska, G.; Gaca, J. *Toxicol. Mech. Methods* **2008**, *18*, 543-550.

(15) Akapo, S. O.; McCrea, C. M. *J. Pharm. Biomed. Anal.* **2008**, *47*, 526-534.

(16) Favre, E.; Schaetzel, P.; Nguygen, Q. T.; Clement, R.; Neel, J. *J. Membr. Sci.* **1994**, *92*, 169-184.

(17) Watson, J. M.; Baron, M. G. *J. Membr. Sci.* **1996**, *110*, 47-57.

(18) Robinson, J. P.; Tarleton, E. S.; Millington, C. R.; Nijmeijer, A. *J. Membr. Sci.* **2004**, *230*, 29-37.

(19) Liang, L.; Dickson, J. M.; Jiang, J.; Brook, M. A. *J. Appl. Polym. Sci.* **2006**, *100*, 2075-2084.

(20) Shi, E.; Huang, W.; Xiao, Z.; Li, D.; Tang, M. *J. Appl. Polym. Sci.* **2007**, *104*, 2468-2477.

(21) Bakhshi, A.; Mohammadi, T.; Aroujalian, A. *J. Appl. Polym. Sci.* **2008**, *107*, 1777-1782.

(22) Santore, M. M.; Kaufman, M. J. *J. Polym. Sci., Part B: Polym. Phys.* **1996**, *34*, 1555-1568.

(23) Moerner, W. E.; Fromm, D. P. *Rev. Sci. Instrum.* **2003**, *74*, 3597-3619.

(24) Walter, N. G.; Huang, C.-Y.; Manzo, A. J.; Sobhy, M. A. *Nat. Methods* **2008**, *5*, 475-489.

(25) Higgins, D. A.; Collinson, M. M. *Langmuir* **2005**, *21*, 9023-9031.

(26) Ye, F.; Higgins, D. A.; Collinson, M. M. *J. Phys. Chem. C* **2007**, *111*, 6772-6780.

(27) Fu, Y.; Ye, F.; Sanders, W. G.; Collinson, M. M.; Higgins, D. A. *J. Phys. Chem. B* **2006**, *110*, 9164-9170.

(28) Schuster, J.; Cichos, F.; von Borzcyskowski, C. *Eur. Polym. J.* **2004**, *40*, 993-999.

(29) Casoli, A.; Schonhoff, M. *Biol. Chem.* **2001**, *382*, 363-369.

(30) Vickers, J. A.; Caulum, M. M.; Henry, C. S. *Anal. Chem.* **2006**, *78*, 7446-7452.

(31) Xie, A.; Liu, B.; Hall, J. E.; Barron, S. L.; Higgins, D. A. *Langmuir* **2005**, *21*, 4149-4155.

(32) Wang, H.; Bardo, A. M.; Collinson, M. M.; Higgins, D. A. *J. Phys. Chem. B* **1998**, *102*, 7231-7237.

(33) Sauerbrey, G. *Z. Phys. A: Hadrons Nucl.* **1959**, *155*, 206-222.

(34) Wilder, E. A.; Guo, S.; Lin-Gibson, S.; Fasolka, M. J.; Stafford, C. M. *Macromolecules* **2006**, *39*, 4138-4143.

(35) Stevens, L. L.; Orler, E. B.; Dattelbaum, D. M.; Ahart, M.; Hemley, R. J. *J. Chem. Phys.***2007**, *127*, 104906.

(36) Lucklum, R.; Behling, C.; Hauptmann, P. *Anal. Chem.* **1999**, *71*, 2488-2496.

(37) Martin-Brown, S. A.; Fu, Y.; Saroja, G.; Collinson, M. M.; Higgins, D. A. *Anal. Chem.***2005**, *77*, 486-494.

(38) Ha, T.; Enderle, T.; Chemla, D. S.; Selvin, P. R.; Weiss, S. *Chem. Phys. Lett.* **1997**, *271*, 1-5.

(39) Ha, T.; Glass, J.; Enderle, T.; Chemla, D. S.; Weiss, S. *Phys. Rev. Lett.* **1998**, *80*, 2093-2096.

(40) Gilliland, J. W.; Yokoyama, K.; Yip, W. T. *Chem. Mater.* **2004**, *16*, 3949-3954.

(41) Wirth, M. J.; Swinton, D. J.; Ludes, M. D. *J. Phys. Chem. B* **2003**, *107*, 6258-6268.

(42) Zhong, Z.; Lowry, M.; Wang, G.; Geng, L. *Anal. Chem.* **2005**, *77*, 2303-2310.

(43) O'Dell, W. *Template Matching*, http://rsbweb.nih.gov/ij/plugins/template-matching.html, 2005.

(44) Ye, F.; Collinson, M. M.; Higgins, D. A. *Anal. Chem.* **2007**, *79*, 6465-6472.

(45) Elson, E. L.; Magde, D. *Biopolymers* **1974**, *13*, 1-27.

4 Single Molecule Studies of Oligomer Extraction and Uptake of Dyes in Poly(dimethylsiloxane) Films

Submitted as J.J. Lange, M.C. Collinson, C.T. Culbertson and D.A. Higgins to *Anal. Chem.* May 2009

4.1 Introduction

Poly(dimethylsiloxane) (PDMS) monoliths, films and membranes are now widely employed in a variety of applications, including microcontact printing,[1] microfluidic separations,[2] solid phase microextraction,[3] pervaporation[4] and nanofiltration.[5] In most cases, the PDMS employed is obtained from commercial sources. PDMS is prepared by mixing a prepolymer incorporating vinyl-terminated dimethylsiloxane oligomers with a curing agent comprised of siliconhydride-terminated dimethylsiloxane and a platinum catalyst. Commercial PDMS precursors also incorporate vinyl- and methyl-terminated silica particles. The resulting liquid precursor mixture is polymerized (i.e., cured via hydrosilation) at elevated temperatures to form a rubbery polymer. The curing process causes crosslinking of the prepolymer components to form a complex polymer network incorporating bound and unbound PDMS chains of variable molecular weights. The unbound PDMS chains that remain are commonly referred to as "low molecular weight oligomers" and are found throughout the bulk of the PDMS.

The residual low molecular weight oligomers tend to make PDMS surfaces "tacky," they can also contaminate contacting surfaces and solutions, and they make the

PDMS more hydrophobic than is frequently desired. As a result, many researchers take steps to remove these oligomers from cured PDMS.[6] The procedures reported vary but almost always involve soaking the PDMS in one or more solvents. The solvents employed cause swelling,[7] which allows the low molecular weight oligomers to diffuse out of the PDMS via a chemical gradient.

A variety of application-specific reasons for removing the low molecular weight oligomers from cured PDMS have been described in the literature. In PDMS-based microfluidic separations, it is now well-known that increased PDMS hydrophilicity leads to more efficient separations.[6, 8, 9] Increased hydrophilicity can be achieved by extraction of the oligomers alone,[8] or the extraction process can be followed by oxidative treatment of the PDMS in an air plasma.[6, 8] Greater hydrophilicity allows for the microfluidic channels to be more easily filled with aqueous solution and increases the charge density on the PDMS surface,[10] facilitating electro-osmotic separations. In other applications, such as in cell culturing, extraction of the low molecular weight oligomers can alter cell adhesion and growth characteristics.[11, 12] In PDMS-based microcontact printing, the extraction of oligomers from the PDMS stamp ensures that the oligomers are not transferred to the substrate along with the desired printing chemical.[13] Finally, in pervaporation, solid phase microextraction and nanofiltration using PDMS-based films and membranes, it is readily apparent that the presence of low molecular weight oligomers should have a profound effect on relevant materials characteristics. For example, the oligomers in these cases may serve as a solvent phase, leading to enhanced solubility and transport of hydrophobic species, or they may serve to block pathways through the materials,[5] limiting uptake of the desired organic species.

While oligomer extraction is commonly performed during fabrication of many of the PDMS materials mentioned above, very little is known about how oligomer extraction alters the physical and chemical properties of PDMS. It is well known that oligomer extraction leads to a decrease in PDMS density. Commonly, a 3-5% decrease in mass has been reported with no apparent change in sample volume for complete oligomer extraction.[6, 8, 14-16] Therefore, it is expected that the open void volume within a PDMS film or monolith will increase significantly after extraction of oligomers. At present, it remains unclear how this density change affects the uptake of small organics.[9] For example, the size of molecules that can partition into PDMS is likely to be different for extracted and unextracted materials.[5] It is also possible that hydrophilic molecules will be taken up more efficiently with the associated reduction in PDMS hydrophobicity. Finally, depending on the specific role played by the oligomers in solvating intercalated species, the rate at which molecules diffuse through the matrix may increase or decrease with oligomer extraction.

Extraction dependent behavior is made even more complex by the manner in which oligomer extraction is believed to occur. Specifically, it is believed that oligomers are most readily extracted from near-surface regions. A gradient in the oligomer concentration along the depth dimension results, leading to a corresponding gradient in PDMS chemical and physical properties. The presence of such gradients is evidenced by the usual reversion of hydrophilic PDMS surfaces to their original hydrophobic state, via diffusion of unextracted low molecular weight oligomers to the surface, some time after oligomer extraction.[8]

In this study, depth-resolved single molecule microscopy is used to probe the chemical and physical consequences of oligomer extraction in PDMS films. To the best of our knowledge, there have been no previous studies that correlate single molecule behavior to the extent of oligomer extraction in PDMS. Samples were extracted 5, 10, 20 and 40 times, using a previously-developed spin extraction process,[17] to yield four different sample types (referred to below as 5x, 10x, 20x and 40x samples). These films were loaded with nanomolar concentrations of BPPDI (a neutral, hydrophobic dye) and R6G (a cationic, hydrophilic dye) for single molecule studies. Images of the different samples incorporate fixed, round fluorescent spots that are attributed to entrapped single molecules. They also incorporate fluorescent streaks that are attributed to diffusing molecules. The population of fixed molecules were quantified by applying a cross-correlation "spot-counting" technique to the images. A unique "burst-counting" routine, employing Bayesian statistics,[18] was used to determine the total population of molecules in each image, while the difference between the total and fixed populations yields a measure of the mobile population. The results show that the absolute population of molecules in the films increases with increasing oligomer extraction. Bulk fluorescence studies of R6G-loaded PDMS monoliths also show an increase in dye loading with oligomer extraction. Simultaneously, the single molecule results depict an extraction-dependent decrease and increase in the relative populations of fixed and mobile molecules, respectively. These results are indicative of a clear increase in the uptake and mobility of organic dyes, as a function of oligomer extraction within PDMS films. Fluorescence autocorrelation data provide measurements of the BPPDI diffusion coefficient, which also reflects an increase in mobility with oligomer extraction. A

model is proposed to describe the role played by PDMS oligomers in governing molecular uptake, entrapment and mobility, and the physical/chemical changes that occur in the PDMS matrix upon oligomer extraction.

These results suggest that oligomer extraction is an effective way to increase the amount of material PDMS films and membranes can absorb or transport when employed in microextraction, pervaporation or filtration processes. Conversely, this same treatment is likely to result in greater loss of analyte in microfluidic devices, affecting relevant figures of merit for chemical separations.[10]

4.2 Experimental

4.2.1 Materials

PDMS was obtained from Dow Corning (Sylgard 184) and used as received. Samples were prepared by mixing the components in the suggested 1:10 (curing agent to polymer) ratio. This mixture was then diluted to ~26 % PDMS by weight in hexanes (ACS grade, Aldrich), mixed thoroughly and spin cast onto plasma-cleaned coverslips (Fisher Premium) at 2000 rpm for 120 s. The slides were then cured at 80 ^{o}C for 24 h. This preparation yielded films with thicknesses of ~1.4 μm, as verified by profilometry. The slides were then spin extracted by repeatedly dropping 200 μL aliquots of spectrophotochemical grade isopropyl alcohol (IPA, Aldrich) on the films and then spinning them at 2000 rpm for 30 s per spin extraction. Each sample was spin extracted 4, 9, 19 or 39 times with pure IPA alone. After spin extracting, dye was added to each sample by dropping a 200 μL aliquot of a nanomolar dye solution in IPA onto each film. The dye-doped IPA was then spun off the films at 2000 rpm for 30 s. Aside from

addition of dye to the films, this latter step also served as the final extraction step, yielding samples extracted 5, 10, 20 and 40 times (i.e., 5x, 10x, 20x and 40x samples). All samples were then stored in a vacuum desiccator until used (minimum of ~15 h).

Two different dyes were employed to probe the dependence of molecular mobility and entrapment on oligomer extraction. A neutral perylene diimide, bis-N,N'-(butoxypropyl)-perylene-3,4,9,10-tetracarboxylic diimide (BPPDI), was employed to probe hydrophobic interactions and physical entrapment in the PDMS matrix. BPPDI was synthesized as described previously.[17, 19, 20] Rhodamine 6G (R6G), a cationic dye was employed to explore the influence of hydrophilic effects and ionic interactions with the matrix. R6G was obtained from Aldrich and used as received. BPPDI-doped samples for single molecule studies were loaded from 100 nM dye solution while R6G was loaded from 10 nM solution.

Samples for bulk dye uptake experiments were prepared by mixing the Sylgard components in a 1:10 ratio, degassing, pouring over a glass plate and curing at 80 ^{0}C for 24 h. The PDMS slabs were then cut into small monoliths (25 mm x 25 mm x 0.4 mm). Oligomers were extracted from the monoliths by immersing them in a beaker of stirred, spectrophotochemical grade IPA. The samples were removed from the IPA at different intervals to vary the level of oligomer extraction. Groups of four monoliths were removed in batches after 15 min, 30 min and 1 h of total extraction time. The IPA in the beaker was replaced with fresh IPA and stirring resumed after each group of monoliths was removed. These samples were subsequently dried for 3 h at 80 ^{o}C and were then placed in separate beakers, each of which was filled with a 9 µM aqueous solution of

R6G. The samples were stored in R6G solution for ~20 h, and were then removed, rinsed with ~4 mL of water on each side and dried under nitrogen.

4.3 Methods

All single molecule spectroscopic measurements were performed on a home-built sample scanning confocal microscope that has been described previously.[21] Briefly, this system is built upon an inverted epi-illumination microscope (Nikon TE-300). The sample sits atop a closed loop X,Y-scanning stage (Sifam Instruments) mounted on this microscope. In all single molecule experiments, fluorescence excitation was accomplished using 488 nm light from a diode laser (Spectra-Physics Cyan Scientific). The laser light was first passed through appropriate filters and optics to ensure a spectrally clean excitation source and to control the incident power. The excitation light was subsequently reflected from a dichroic beamsplitter (Chroma 500DCLP) into the back aperture of an oil immersion objective (Nikon Plan Fluor, 1.3 numerical aperture, 100x magnification). The objective was mounted on a closed-loop positioner (Polytec PI) to allow for depth dependent imaging within the sample. It produced a nearly diffraction limited focus of $\approx$ 300 nm $1/e^2$ transverse radius and $\approx$ 600 nm depth of focus. This same objective was also used to collect the resulting single molecule fluorescence. In all experiments, the incident laser power was maintained at 3 μW (estimated from measurements made external to the microscope). An electronic shutter was used to control illumination of the sample. Fluorescence collected from the sample was isolated from the excitation light by passage back through the dichroic beamsplitter, an appropriate holographic notch filter, two 530 nm longpass filters, and a 580 nm bandpass filter having a 40 nm passband. A 100 μm diameter pinhole placed in the primary image

plane of the microscope was used to achieve confocal detection. A single-photon-counting avalanche photodiode was used as the detector.

Fluorescence images were acquired by raster scanning the sample above the focused laser spot. The fluorescence signal was integrated for 10ms per pixel in 200 x 200 pixel images of 20 x 20 μm^2 sample regions. Images were collected at different depths separated by 0.5 μm increments from the sample surface, yielding four images along the depth dimension in each film. Single-point fluorescence time transients for use in fluorescence correlation spectroscopy (FCS) studies were obtained by positioning selected sample regions in the laser focus and recording the spectrally integrated fluorescence in time. Individual time transients were recorded for ~ 1 h duration with dwell times of 10 ms.

All single molecule experiments were performed under controlled, dry atmospheric conditions. This was achieved by purging a 0.85 L Plexiglas chamber covering the sample with dry nitrogen (flow rate ~30 L/h) for a period of ~45 min before starting the experiments. This atmosphere was maintained throughout the duration of all experiments. Images obtained from identical sample regions over the course of several hours showed no detectable trends in molecular mobility, indicating the time was sufficient for equilibration with the dry atmosphere.

Bulk R6G uptake in PDMS monoliths was evaluated by recording fluorescence spectra of these samples on a commercial fluorometer (SPEX Fluoromax 2). In these experiments, 488 nm light was employed for sample excitation and the resulting fluorescence was collected between 500 and 800 nm, after passing through appropriate longpass filters. The samples were mounted at 45^o to the incident beam, with

fluorescence collected from the front face. To quantify the fluorescence from each sample, the fluorescence peak was fit to a Gaussian distribution and then integrated.

4.4 Results

4.4.1 Fluorescence Images

Fluorescence images of samples doped with nanomolar concentrations of BPPDI were found to incorporate both well-separated round fluorescent spots and fluorescent streaks. Figure 1 shows representative images obtained from 5x, 10x and 20x samples (Figure 4-1A-C, respectively) and corresponding blank (i.e., undoped) films (Figure 4-1D-F). Qualitatively similar results were obtained for R6G-doped samples. However, these latter images show a greater density of round spots, along with a significant reduction in the number of streaks (relative to BPPDI). Comparison of the images obtained from dye-doped samples and blanks demonstrates that virtually all of the fluorescent features observed in the sample images result from the presence of dye. The observation of round fluorescent spots in images of the dye-doped samples is consistent with the presence of single dye molecules (BPPDI or R6G) that are entrapped in fixed locations on the imaging time scale (i.e. ~ 2.5 s/line). The fluorescent streaks observed are all oriented along the fast-scan direction (i.e., vertical on the images) and reflect the presence of molecules that are mobile on the imaging time scale, as described previously.[22] Images acquired at different depths in these films are qualitatively indistinguishable from one another.

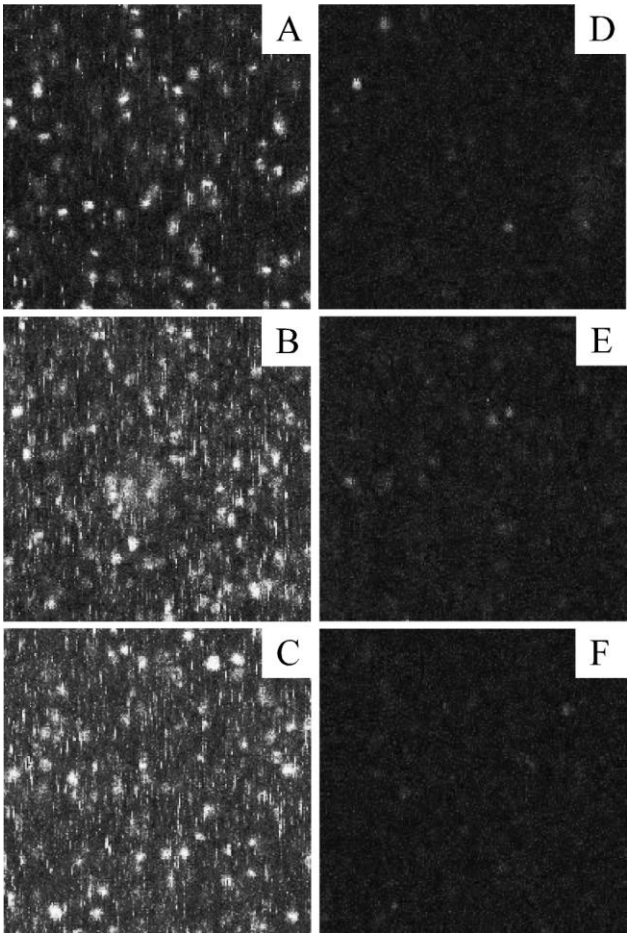

Figure 4-1 Fluorescence images of (A-C) PDMS films loaded with BPPDI and (D-F) blank (undoped) PDMS films. The three pairs of doped- and blank-film images correspond to samples extracted 5, 10 and 20 times, respectively. Images of the dye-doped films show diffraction limited fluorescent spots attributed to excitation of single molecules entrapped at fixed locations. The fluorescent streaks shown in these same images are attributed to fluorescence from diffusing molecules. All images are of 20 x 20 μm^2 regions. The full range of the grayscale in each is 0 counts to 58 counts.

While qualitatively similar, a clear trend is observed in the fluorescence images of films that have been spin extracted different numbers of times (compare Figure 4-1A-C). This series of images appears to show a degradation in the signal to background ratio with increasing oligomer extraction. The apparent reduction in image quality comes

from a significant increase in the prevalence of fluorescent streaks in images of films that have been spin extracted greater numbers of times. The increase in fluorescent streaks does not arise from sample contamination as the blank films show no such trend. Instead, this observation reflects an increase in the population of mobile molecules and/or an increase in their mobility. Since all films were prepared in identical fashion, except for the number of spin extractions employed, this trend suggests the extraction process has an important impact on the ability of small organic molecules to partition into and move through the PDMS films.

4.4.2 Image Analysis

More quantitative information on the impact of PDMS oligomer extraction was obtained by further analyzing the fluorescence images. Two different methods of analysis were employed. The first is identical to that employed in our earlier study of IPA-loaded PDMS thin films[17] and provides a quantitative measure of the number of fixed molecules in a given image area. The necessary routines are available as part of the Image J software package.[23] The analysis involves cross-correlating each image with an idealized Gaussian kernel having a standard deviation of 1.6 pixels.[22] The cross correlation image obtained consists of values ranging from -1 (anticorrelated features) to +1 (perfectly correlated features). The number of Gaussian shaped spots (i.e. fixed molecules) is then obtained by specifying thresholds for both the correlation values and the number of contiguous pixels comprising each spot. Spots that meet the selected criteria are counted as fixed molecules. Here, the image spots counted were required to have correlation values falling between 0.5 and 1 over an area of greater than 5 but fewer than 30 pixels. These parameters were selected by first applying the analysis to

simulated images. These same simulations were also used to verify the dynamic range and integrity of the analysis under conditions that closely mimicked those of the experiments.[17]

In the second method of analysis, the total number of fluorescent "bursts" above background was counted along the fast-scan direction in each image. Bayesian statistical methods were employed to ensure proper counting of the bursts. Bursts from both fixed and mobile molecules were counted, with the burst count yielding a measure of the total population of molecules in a given image (see below). The Bayesian analysis specifically involves calculation of the following probability for each image pixel:[18]

$$P(B \mid N) = \frac{P(N \mid B)P(B)}{P(N)}$$

EQ 4-1

Where $$P(N) = P(N \mid B)P(B) + P(N \mid notB)P(notB)$$

EQ 4-2

Briefly, the probability, P(B|N), that a given pixel of N photon counts corresponds to the image background (B) is calculated via EQ 4-1. Normal distributions were assumed for background and signal counts (i.e., approximating the expected Poisson distributions). P(N|B) represents the conditional probability that N counts would be observed, assuming the pixel is background, while P(B) represents the empirically-determined prior probability that a pixel is background (i.e., reflecting the prevalence of background pixels in the neighborhood). Here, a 15 pixel moving window was employed in determining the prior probability. Finally, P(N) represents the marginal probability of measuring N counts, based on the assumption the pixel must represent either background

or not (notB). A similar Bayesian calculation was also performed to determine P(S|N), the probability that a given pixel corresponds to signal. In order for a pixel to be considered signal, the probability P(B|N) was required to be ≤ 1 % while P(S|N) was required to be ≥ 90 %. Initial signal and background determination was accomplished by adding individual pixels of ever increasing counts to the background calculation, until the next highest count rate had <0.1 % probability of being background. Representative image data and analysis results are shown in Figure 4-2. The image data is shown in black, while the gray trace shows the Bayesian interpretation of the data set, with each pixel assigned as signal (high) or background (low).

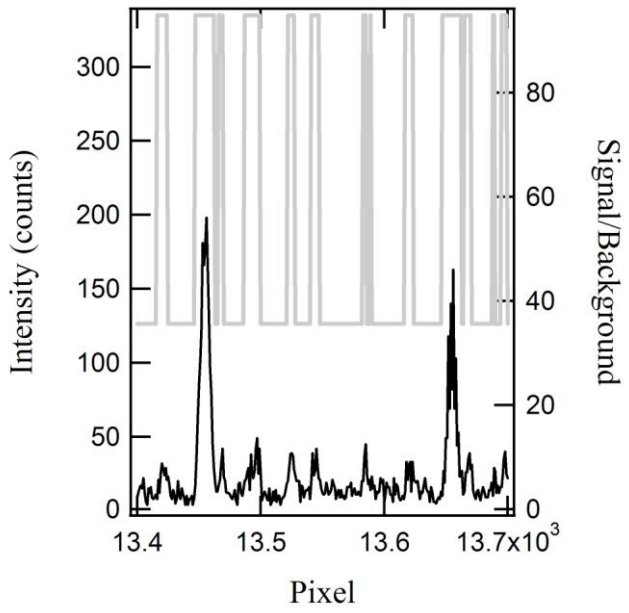

Figure 4-2 Representative data from the Bayesian "burst count" analysis used to determine the number of fluorescent bursts in each image. The image data is plotted in black while the Bayesian interpretation of each pixel as signal (high) or background (low) is shown in gray. The analysis provides a quantitative means for determining the total population of molecules in a given image.

In order to relate the number of bursts in a given image to the total population of molecules present, the number of bursts produced by both fixed and moving molecules must be approximately the same and must be known. Simulated images of alternately fixed and moving populations of molecules were used for this purpose. The simulated images were generated under conditions similar to those of the experiments (i.e., similar concentrations, diffusion coefficients, see below, and laser focus). The results of these simulations showed that an average of 5.0±0.4 bursts were produced by moving molecules while fixed molecules yielded an average of 5.6±0.2 bursts per molecule (i.e., corresponding to the full width of a fixed spot in the slow-scan direction). While the number of bursts per molecule was found to decrease with increasing concentration (as the spots and streaks begin to overlap) the values for fixed and moving species were found to be similar to within ~10 %. It was therefore assumed that one molecule produces an average of 5 bursts, providing a direct conversion from burst count to population of molecules in each image.

4.4.3 Absolute Molecular Populations

The mean populations of fixed molecules obtained from the spot analysis for 5x, 10x, 20x and 40x BPPDI- and R6G-doped films are shown in Figures 3A,B (data labeled "Fixed"). The variability observed in the number of fixed molecules in each case falls outside the Poisson limit, a clear indication of some variability in the samples. Nevertheless, the BPPDI data depict a clear increase in the population of fixed molecules in films that have been extracted to a greater extent. Statistical analysis of the data shows that there is a positive correlation in the data at the 86 and 53% confidence levels, respectively. The R6G data exhibit a marked increase in the population of fixed

molecules over that observed for BPPDI at all but the highest level of oligomer extraction. The trend in population with increased oligomer extraction is also less obvious for R6G. Furthermore, neither sample exhibits a detectable trend in the population of fixed molecules as a function of sample depth probed (see Table 4-1). This latter observation is consistent with uniform dye loading throughout the PDMS films. It also suggests that the substrate-film and film-air interfaces play little role in determining the populations of entrapped and mobile molecules.

BPPDI								
	Fixed				**Moving**			
	5x	10x	20x	40x	5x	10x	20x	40x
Top	33±4	55±6	56±4	67±5	90±40	180±30	280±30	220±10
-0.5	37±6	65±8	54±7	81±3	110±10	210±60	290±40	260±5
-1	50±6	71±9	51±7	79±7	110±20	210±40	280±50	250±10
-1.5	50±4	63±7	49±5	80±7	100±30	230±20	280±60	230±20
	Total							
	5x	10x	20x	40x				
Top	130±40	230±30	330±40	290±10				
-0.5	140±10	270±60	340±50	340±10				
-1	160±20	280±40	330±50	320±20				
-1.5	150±30	290±10	330±60	310±20				
R6G								
	Fixed				**Moving**			
	5x	10x	20x	40x	5x	10x	20x	40x
Top	57±4	74±5	73±4	66±4	85±20	110±10	120±20	130±10
-0.5	64±6	78±5	75±5	81±6	90±20	130±10	120±20	140±5
-1	63±4	82±5	81±6	78±8	70±10	130±10	130±20	170±10
-1.5	56±4	83±9	85±7	83±6	70±10	130±10	130±30	170±20
	Total							
	5x	10x	20x	40x				
Top	140±20	180±10	200±30	200±10				
-0.5	150±20	210±10	190±20	220±10				
-1	140±10	210±20	210±30	250±20				
-1.5	120±20	210±10	210±30	250±20				

Table 4-1 Mean populations and 90% confidence intervals from spot and burst counting data.

The population of moving molecules in each case was found by subtracting the population of fixed molecules from the population of total molecules determined in the "burst" analysis described above. Figure 4-3A,B also plot the populations of moving molecules (data labeled "Moving"). Mean values and 90 % confidence intervals are shown for 5x, 10x, 20x and 40x spin extracted films. These data depict a clear increase in the population of moving molecules for both BPPDI- and R6G-doped samples, as a function of the number of spin extractions. Statistical analysis of the data shows that there is a positive correlation at the 66 and 90 % confidence intervals respectively. In contrast to what was observed for fixed molecules, the population of moving molecules in R6G-doped samples is noticeably smaller than in the BPPDI-doped samples. As shown in Table 4-1, no detectable trend with respect to sample depth was observed.

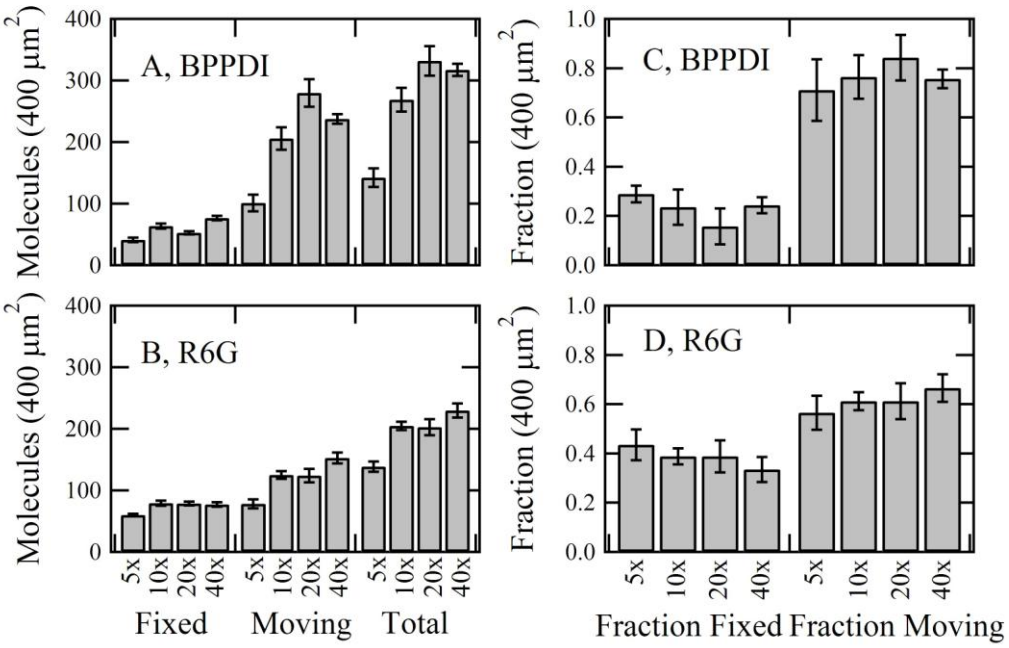

Figure 4-3 A), B) Absolute populations of fixed, moving and total molecules (per 400 μm^2) for BPPDI- and R6G-doped films, respectively. C), D) Relative populations of fixed and moving molecules determined from the corresponding absolute populations. Four different sample types are depicted in each case, corresponding to 5x, 10x, 20x and 40x extracted films. The population of fixed molecules was determined by the cross-correlation method. The total population of molecules was determined by the Bayesian burst analysis, under the assumption that both fixed and moving molecules produce five fluorescent "bursts" each. The total population of molecules exhibits a clear increase with increasing number of extractions for both BPPDI- and R6G-doped samples. In contrast, the relative populations of fixed and moving molecules are observed to decrease and increase, respectively, with oligomer extraction. The error bars represent the 90% confidence interval around the mean.

Figure 4-3A,B also plot the mean values and 90% confidence intervals for the total population of molecules in each image region (data labeled "Total"). These values were calculated from the number of bursts obtained from the Bayesian analysis discussed above. Once again, a clear upward trend in the population of BPPDI (75% confidence)

and R6G (84% confidence) molecules in the PDMS matrix is observed as a function of oligomer extraction. The concentrations of BPPDI and R6G molecules were found to increase by 120% and 70%, respectively, between 5x and 40x samples. Interestingly, the concentration of molecules loaded into the film was found to be only ~ 26 % smaller for R6G than for BPPDI. Given that the R6G concentration employed to load the films was ten times smaller than in the case of BPPDI, this suggests R6G loading is approximately three-fold more efficient than BPPDI loading. As expected from the populations of fixed and moving molecules, no depth dependence in the total concentration of molecules was observed (see Table 4-1). While oligomer extraction is believed to occur primarily in near-surface regions,[8, 11, 15] the uniformity in the populations of fixed, moving and total molecules as a function of film depth suggests both oligomer extraction and dye loading occur uniformly throughout the full 1.4 μm thickness of the films.

Interestingly, the concentration of molecules in the film can be calculated from the number of molecules counted per image. Accounting for the sample volume (2.48 x 10^{-13} L) and assuming a maximum of ~ 350 molecules per image, a peak concentration of ~2.3 nM is obtained. This corresponds nicely with concentrations often used for single molecule investigations.

4.4.4 Relative Molecular Populations

The absolute population data discussed above indicates that the populations of both fixed and moving molecules increase with increasing extraction of oligomers. Since the total population of molecules increases with oligomer extraction, these trends would be expected, assuming the fixed and mobile populations comprise constant fractions of the total. However, by recharacterizing the population data in terms of the fraction of

fixed and mobile molecules, different trends appear. Figure 4-3C and D depict these data. As shown in these plots, the relative population of fixed molecules actually decreases for both BPPDI and R6G as oligomer extraction increases. Statistical analysis of the data shows that a negative correlation exists at the 27 and 97% confidence intervals. Furthermore, the increase observed in the relative population of mobile molecules is still present, but less pronounced, than in the plots of absolute populations. Here the statistical analysis shows that the trend in the data is positive at the 27 and 97% confidence intervals for BPPDI and R6G, respectively.

4.4.5 Bulk Rhodamine 6G Experiments

Bulk fluorescence studies of R6G-doped PDMS films were employed to further explore the dependence of PDMS properties on oligomer extraction and to verify some of the trends observed in the single molecule data. The data from the bulk studies (Figure 4-4) depict a clear monotonic increase in fluorescence with oligomer extraction. Films extracted for 30 min and 1 h exhibited 20 % and 42 % average increases, respectively, in fluorescence over those extracted for only 15 min, consistent with an increase in dye concentration in extracted PDMS.

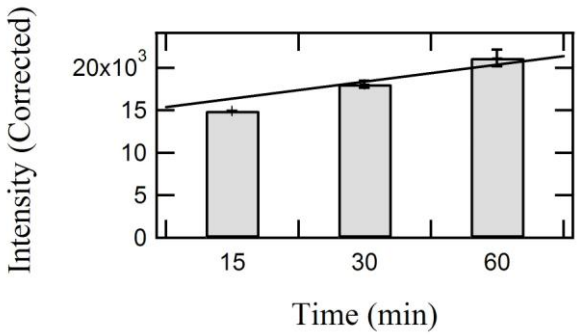

Figure 4-4 Results of the bulk R6G experiment discussed in section 4.4.5. A clear increase in fluorescence intensity is observed.

4.4.6 Single Point Time Transients

The data presented above depict clear changes in the populations of fixed and mobile species with increasing oligomer extraction. Such trends most certainly reflect changes in the properties of the PDMS that may also lead to changes in the rate of molecular diffusion and the molecular entrapment time within the films.[24]

Fluorescence autocorrelation methods were employed to more clearly explore the impact of oligomer extraction on molecular mobility and entrapment in BPPDI-doped PDMS. To this end, single point time transients were recorded from randomly selected locations in the films. The transients were subsequently autocorrelated and fit to the following model (EQ 4-3), which incorporates terms for both molecular diffusion in three dimensions and molecular entrapment:

$$C(\tau) = \frac{A_d}{1 + D\tau/s^2} \frac{1}{\sqrt{1 + D\tau/z^2}} + A_e \exp(-\tau k)$$

EQ 4-3

Here, D represents the diffusion coefficient, A_d and A_e the contributions of diffusion and entrapment, respectively, to the autocorrelation amplitude, and *k* represents the combined rate constant for fluctuations due to trap escape, blinking,[25] bleaching and molecular reorientation.[26,27] The first term in EQ 4-3 describes diffusion in the xy plane, with s^2 representing the transverse beam variance. This term also incorporates a component describing diffusion in the z direction, with z^2 representing the depth of focus in the longitudinal direction. The second term describes molecular entrapment in the films but may also include contributions from the other sources noted above.

Single point time transients (~ 1h in duration each) were obtained from a minimum of four locations at each depth within the PDMS films. The results obtained by fitting the autocorrelated transients to EQ 4-3 are given in Table 4-2. These data show that the rate of BPPDI diffusion increases with increasing oligomer extraction. The mean diffusion coefficients in 5x, 10x, and 20x films were found to be 8(±1) x 10^{-10} cm^2/s, 9(±1) x 10^{-10} cm^2/s and 11(±2) x 10^{-10} cm^2/s, respectively (error bars represent the 90% confidence intervals). While a clear trend was observed with oligomer extraction, autocorrelation data obtained as a function of depth within the films showed no change in the diffusion coefficient, as is consistent with the population data described above.

	D(10^{-10} cm^2/s)	A_d (rel.)	K
5x	8±1	0.38±0.05	0.10±0.03
10x	9±1	0.41±0.05	0.10±0.03
20x	11±2	0.40±0.05	0.10±0.02

Table 4-2 Values and 90% confidence intervals obtained by fitting autocorrelated time transients to Eqn. 3. A_d is reported relative to the total autocorrelation amplitude.

At first glance, the similar values obtained for A_d and A_e (see Table 4-2) and their lack of variation with oligomer extraction appears to contradict the imaging data, which show a much greater population of mobile molecules that also increases with oligomer extraction. However, as shown by Ye, et al.,[28] molecules that are randomly oriented but rotationally and translationally immobile contribute more strongly (by a factor of ~2) to the autocorrelation amplitude than do rapidly reorienting molecules. Earlier investigations of the polarization dependence of BPPDI fluorescence excitation show that molecules entrapped in dry PDMS thin films are rotationally immobile, exhibiting only occasional orientational jumps.[17] Accounting for these differences in the contributions of fixed and mobile species to the autocorrelation data indicates that mobile molecules also dominate the autocorrelation data. The population of moving molecules contributing to the autocorrelation data is estimated to comprise ~60 % of the total, while the population of moving molecules determined from the imaging data is, on average, ~75 % of the total. The residual difference likely arises from differences in the time scales over which these two methods probe the populations of fixed molecules. Specifically, the imaging data reflects the population of molecules entrapped over relatively long periods of time.

4.5 Discussion

Several conclusions may be drawn from the above results. First, measurable populations of fixed and mobile molecules are found within the PDMS films for both neutral, hydrophobic BPPDI and cationic, hydrophilic R6G dopants. Second, the absolute populations of the fixed and mobile species all increase with increasing oligomer extraction, reflective of a concomitant increase in the overall uptake of the dyes by the PDMS matrix. Third, while the relative population of mobile molecules also increases

with increased oligomer extraction, the relative population of fixed molecules is observed to decrease, suggestive of greater molecular mobility in extracted PDMS films. Fourth, the greater mobility of BPPDI molecules in extracted films is confirmed by an increase in their diffusion coefficient with increased oligomer extraction. Fifth, no dependence on film depth is observed in any of the above data for the 1.4 μm thick films investigated. Taken together, these results demonstrate that there is a significant change in the physical properties of the PDMS matrix with oligomer extraction. Furthermore, these changes occur uniformly throughout the depth of the films investigated. These changes have a direct and important impact on the ability of the PDMS films to absorb organic dyes and on the abilities of these dyes to migrate through and become entrapped in the matrix.

The observation of both fixed and mobile molecules in the PDMS films suggests the existence of open voids within the matrix that facilitate molecular mobility but can also lead to molecular entrapment. The mobility of large organic dyes in solvated PDMS films has been described previously,[17] as has the entrapment of such molecules.[17] The lack of an observed depth dependence to these populations indicates that neither the substrate-PDMS interface nor the PDMS-air interface play important roles in molecular mobility and entrapment for either BPPDI or R6G. As proposed previously,[17] fixed BPPDI molecules are believed to be physically entrapped in small voids within these materials.[5] Likewise, the R6G molecules are also expected to become physically entrapped. Unlike BPPDI, however, the cationic nature of R6G also allows it to electrostatically bind to the PDMS matrix. The greater fraction of fixed R6G molecules indicates that electrostatic effects are likely important. According to the manufacturer, PDMS (Sylgard 184) may contain up to ~60 % silica by weight. While the silica has

been passivated by trimethylsilylation, it is very likely some unreacted silanol groups remain on the surfaces of incorporated silica particles.[29] Such groups are expected to carry a negative charge, providing sites to which cationic R6G can bind.[30,31]

The conclusion that both dyes can become physically entrapped in the PDMS is consistent with prior results presented in the nanofiltration literature.[5] As indicated in recent work, PDMS materials are expected to incorporate voids that are 1-1.5 nm in size,[5] similar to the dimensions of BPPDI and R6G, suggesting that they could easily become entrapped in the smaller voids and may more easily move through the larger ones. For the purposes of the present work, however, it is important to note that no previous studies (to our knowledge) have addressed the possible impacts of oligomer extraction on the size distribution of the voids.

Evidence that the relative populations of mobile and entrapped molecules increase and decrease, respectively, with increasing oligomer extraction provides valuable information on the mechanisms of mobility and entrapment in these materials. For the mobile fraction, it may be hypothesized that small PDMS oligomers serve as a solvent and facilitate molecular mobility. The data presented allow for immediate rejection of this hypothesis as mobile molecules would then be expected to become less prevalent as more oligomers are extracted. Likewise, the population of entrapped molecules would also be expected to increase.

4.5.1 Model for Extraction-Dependent Entrapment and Mobility

The observations presented above instead suggest an alternative model for molecular diffusion and trap escape in PDMS. Figure 4-5 presents a pictorial view of the model. The matrix within cured, unextracted PDMS films is proposed to consist of a

cross-linked PDMS matrix incorporating entangled, low molecular weight oligomers. Molecular mobility and access to what little open void volume exists in these materials is highly hindered. Furthermore, the voids that are present are likely to have a distribution peaked at relatively small average size. Molecules that find open voids frequently become entrapped because their size may closely match the size of the voids[5] and/or because their escape may be blocked by the dense, intertwined matrix.

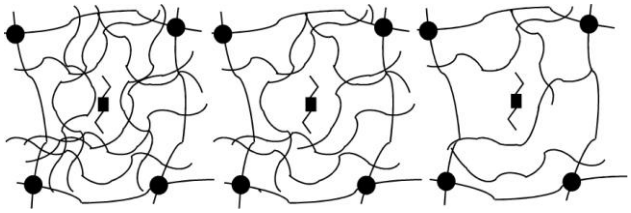

Figure 4-5 Model for the dye-doped PDMS matrix as a function of oligomer extraction. Initially, (left) the PDMS contains cross-linked sites (black circles) and many unreacted oligomers that are intertwined within the crosslinked matrix. Contained within the matrix are BPPDI molecules (black square with tails) that are either entrapped at fixed locations or diffusing (not shown). As some of the low molecular weight oligomers are removed (middle), the distribution of void sizes in the PDMS shifts to larger values. Fewer fixed molecules and more diffusing molecules are observed. Highly extracted films (right), incorporate the largest voids, resulting in the fewest fixed molecules and the largest number of diffusing molecules. The greater open void volume in the extracted films allows for an increase in the total concentration of dyes in the PDMS.

As the PDMS is extracted, the void size distribution shifts to larger values (see middle panel, Figure 4-5). The smallest voids begin to open up, allowing entry of more dye molecules, while larger voids only increase in size. The total concentration of dyes within the PDMS increases due to the greater accessible void volume created by oligomer extraction. The large voids also become interconnected during extraction, providing new

pathways through which the molecules can diffuse. Importantly, the shift in the distribution of void sizes leads to a decrease in the population of voids having the right size to trap the probe dyes. Therefore, as oligomers are removed, the dye molecules become more mobile. As noted above, there must be some "solvent" present to facilitate molecular mobility. In this model, we hypothesize that the "free" ends of the otherwise cross-linked PDMS chains comprising the matrix serve as the solvent and facilitate dye molecule motions.

At some point, all "free" low molecular weight oligomers will be extracted from the films (see right panel, Figure 4-5). When this occurs, the total population of molecules should cease to increase and the fractions of entrapped and mobile molecules should become invariant with further extraction attempts. The material density has reached its lower limit at this point (i.e., corresponding to the greatest possible void volume). Previous work suggests the limit of oligomer extraction in PDMS is ~ 3-5 % by weight.[6, 8, 14-16] Unfortunately, clear evidence that this limit has been reached has not yet been obtained in our thin films.

4.6 Conclusions

In conclusion, bulk and single molecule fluorescence methods have been used to explore the impacts of oligomer extraction on the properties of cured PDMS films. Both neutral and cationic fluorescent dyes were employed. Quantitative counting of fluorescent spots in images of dye-doped PDMS showed that the absolute populations of fixed molecules increased with increasing oligomer extraction for both BPPDI- and R6G-doped samples. Likewise, the total population of mobile molecules was also observed to increase with oligomer extraction in both cases, as was the population of mobile

molecules. The single molecule results indicated the BPPDI and R6G concentrations in the films increased by 120% and 70%, respectively, across the range of films studied. Bulk R6G fluorescence results obtained on PDMS monoliths provided further proof that the dye concentration within the PDMS increased with the extent of oligomer extraction. In contrast to the absolute populations, the relative populations of fixed and mobile molecules were observed to decrease and increase, respectively, consistent with an extraction-dependent increase in the mobility of the molecular dopants. The observed extraction-dependent increase in the diffusion coefficient for BPPDI provided further evidence of an increase in molecular mobility. A model was developed to describe these extraction-dependent changes in materials properties. This model predicts that extraction of the low molecular weight oligomers increases the open void volume within the PDMS, allowing PDMS chain ends to become more mobile. The greater open void volume and increased PDMS chain mobility increases dye loading and dye mobility, while simultaneously leading to a reduced population of voids having an appropriate size to trap the dye molecules.

The data presented here clearly show that the concentration of small organic molecules that can be loaded into PDMS films depends on the degree to which low molecular weight oligomers have been extracted from the samples. These results are of significance for any technique that utilizes PDMS as an extraction or separation medium. In applications where the absorption of small organics is desired (i.e., solid phase microextraction and pervaporation), oligomer extraction represents a simple means to increase the uptake of organics. In addition, the mobility of molecules incorporated in the PDMS increases with the extent of extraction, providing a means to increase the

speed of such applications. Conversely, the present results also suggest that the extraction procedures commonly used to increase the hydrophilicity of PDMS microfluidic chips may result in loss of analyte by increased absorption into the PDMS, thus affecting important figures of merit for PDMS based microfluidic separations. Finally, the partial extraction of unreacted low molecular weight oligomers from PDMS nanofiltration membranes may afford tunability of pore size.

4.7 References

(1) Kumar, A.; Whitesides, G. M. *Appl. Phys. Lett* **1993**, *63*, 2002-2004.

(2) McDonald, J. C.; Whitesides, G. M. *Acc. Chem. Res.* **2002**, *35*, 491-499.

(3) Kaur, V.; Malik, A. K.; Verma, N. *J. Sep. Sci.* **2006**, *29*, 333-345.

(4) Yahaya, G. O. *J. Membr. Sci.* **2008**, *319*, 82-90.

(5) Robinson, J. P.; Tarleton, E. S.; Ebert, K.; Millington, C. R.; Nijmeijer, A. *Ind. Eng. Chem. Res.* **2005**, *44*, 3238-3248.

(6) Vickers, J. A.; Caulum, M. M.; Henry, C. S. *Anal. Chem.* **2006**, *78*, 7446-7452.

(7) Briseno, A. L.; Roberts, M.; Ling, M.-M.; Hyunsik Moon; Nemanick, E. J.; Bao, Z. *J. Am. Chem. Soc.* **2006**, *128*, 3880-3881.

(8) Lee, J. N.; Park, C.; Whitesides, G. M. *Anal. Chem.* **2003**, *75*, 6544-6554.

(9) Mukhopadhyay, R. *Anal. Chem* **2007**, *79*, 3248-3253.

(10) Toepke, M. W.; Beebe, D. J. *Lab Chip* **2006**, *6*, 1484-1486.

(11) Lee, J. N.; Jiang, X.; Ryan, D.; Whitesides, G. M. *Langmuir* **2004**, *20*, 11684-11691.

(12) Millet, L. J.; Stewart, M. E.; Sweedler, J. V.; Nuzzobc, R. G.; Gillette, M. U. *Lab Chip* **2007**, *7*, 987–994.

(13) Deng, T.; Wu, H.; Brittain, S. T.; Whitesides, G. M. *Anal. Chem.* **2000**, *72*, 3176-3180.

(14) James, P. M.; II, E. M. B.; Dawson, B.; Logan, J. A. *J. Macromol. Sci.-Chem* **1974**, *A8*, 135-155.

(15) Chang, J. W.; Gorur, R. S. *IEEE Transactions on Dielectrics and Electrical Insulation* **1994**, *1*, 1039-1046.

(16) Mark, J. E.; Zhang, Z. M. *J. Polym. Sci., Polym. Phys. Ed.* **1983**, *21*, 1971-1979.

(17) Lange, J. J.; Culbertson, C. T.; Higgins, D. A. *Anal. Chem.* **2008**, *80*, 9726–9734.

(18) Freund, J. E.; Walpole, R. E. Mathematical Statistics, 4 ed.; Prentice Hall, Inc.: Englewood Cliffs, N.J., 1987.

(19) Xie, A.; Liu, B.; Hall, J. E.; Barron, S. L.; Higgins, D. A. *Langmuir* **2005**, *21*, 4149-4155.

(20) Everett, T. A.; Twite, A. A.; Xie, A.; Battina, S. K.; Hua, D. H.; Higgins, D. A. *Chem. Mater.* **2006**, *18*, 5937-5943.

(21) Wang, H.; Bardo, A. M.; Collinson, M. M.; Higgins, D. A. *J. Phys. Chem. B* **1998**, *102*, 7231-7237.

(22) Martin-Brown, S. A.; Fu, Y.; Saroja, G.; Collinson, M. M.; Higgins, D. A. *Anal. Chem.* **2005**, *77*, 486-494.

(23) O'Dell, W. *Template Matching*, http://rsbweb.nih.gov/ij/plugins/template-matching.html, 2005.

(24) Watson, J. M.; Zhang, G. S.; Payne, P. A. *J. Membr. Sci.* **1992**, *73*, 55-71.

(25) Ha, T.; Enderle, T.; Chemla, D. S.; Selvin, P. R.; Weiss, S. *Chem. Phys. Lett.* **1997**, *271*, 1-5.

(26) Ha, T.; Glass, J.; Enderle, T.; Chemla, D. S.; Weiss, S. *Phys. Rev. Lett.* **1998**, *80*, 2093-2096.

(27) Gilliland, J. W.; Yokoyama, K.; Yip, W. T. *Chem. Mater.* **2004**, *16*, 3949-3954.

(28) Ye, F.; Collinson, M. M.; Higgins, D. A. *Anal. Chem.* **2007**, *79*, 6465-6472.

(29) Sun, Y.-M.; Chen, J. *J. Appl. Polym. Sci.* **1994**, *51*, 1797-1804.

(30) Wirth, M. J.; Swinton, D. J.; Ludes, M. D. *J. Phys. Chem. B* **2003**, *107*, 6258-6268.

(31) Zhong, Z.; Lowry, M.; Wang, G.; Geng, L. *Anal. Chem.* **2005**, *77*, 2303-2310.

5 Potential Dependent Dehybridization of ssDNA Hairpins Functionalized on a Single Carbon Nanofiber

5.1 Introduction

Until this point, the research presented in this dissertation focused on detecting and monitoring the physical properties of single molecules and the environments in which they reside. As an extension of single molecule research, the present chapter describes detection of small groups of molecules hybridized onto single carbon nanofibers (CNF). Specifically, single stranded DNA (ssDNA) hairpins, called molecular beacons (MBs), are explored.[1]

Recently, this research has become very important due to the rise in accidental outbreaks of harmful bio-organisms like E. Coli. Additionally, terrorism is a constant threat in the global community and intentional contamination of our food supply is a possibility. Accidental or intentional outbreaks of harmful bio-organisms have caused many people to become ill or, in some cases, to die. Compounding the issue is the significant economic impact that an outbreak can have. One of the most recent outbreaks, an E. Coli O157 H7 outbreak from spinach, caused a loss of 50 – 100 million dollars for the company responsible.[2,3] In 2001, the USDA estimated that five major foodborne diseases kill 5000, hospitalize 325,000 and sicken 76 million people annually. In addition, they estimate that these diseases cost the nation at least 6.9 billion dollars each year in productivity losses, medical treatments and premature deaths.[4] To this end, a testing program that can provide early detection of such pathogens will reduce the

spread of contaminated goods, which will, in turn, minimize health hazards and economic losses. To do this, techniques that detect small amounts (even 10 cells)[5] of bio-organisms must be developed.

The approach developed here is to create a stand-alone lab-on-a-chip device, like that shown in Figure 5-1, which incorporates many different sample handling and analysis steps, including assays to detect DNA fragments from harmful bio-organisms (Figure 5-1H).[6-9]

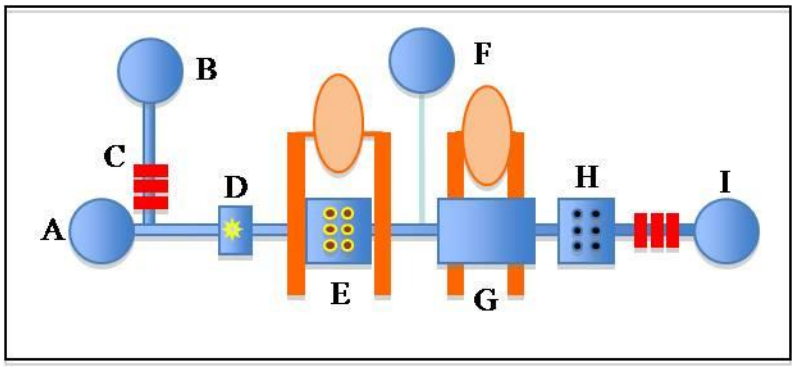

Figure 5-1 Here a diagram of what a stand-alone lab-on-a-chip might look like is presented. Samples could be loaded onto the device through a sample inlet (A) and pumped down the chip in buffer (B) using a micropump (C). The cells could then be counted using a laser (D). Next electrochemical cell lysis (E) could occur. The cell lysate could be mixed with PCR components (F) and amplified by PCR (G). Next the CNF array characterized in these experiments would be used to detect the amplified cell lysate (H). Finally, waste could be directed through another pump and out of the chip through a reservoir (I).

Briefly, foodstuff samples will be loaded onto a microfluidic chip. Sample preparation will first involve cell lysis, followed by different analysis schemes, which could include an immunoassay or a nucleic acid assay. The nucleic acid assay (Figure 5-1H), the focus of the work here, consists of an array of encapsulated vertically aligned carbon nanofibers (VACNFs), which have been functionalized with ssDNA molecules.

The ssDNA serves as a selective probe for DNA from a specific micro-organism. The simplest design of this device would allow for diffusion to carry the DNA across the array and down to the ssDNA. While, this is a perfectly viable way to achieve detection of DNA lysate, the amount of time required for the DNA to diffuse to the ssDNA would be prohibitive. In addition, the DNA may not be in the proper conformation to bind to the ssDNA on the VACNF array. To overcome both of these slow processes a series of potentials could be applied to the array. Positive potentials could be implemented to draw the DNA strands from solution down to the electrodes. Also, negative potentials will dehybridize the ssDNA functionalized onto the ends of the CNFs allowing the DNA, which has just been drawn to the surface, to bind to the ssDNA. To model the dehybridization and binding process, MBs are employed. Understanding the process through which this dehybridization occurs is crucial to ensuring the proper function of the microarray[10]. The results presented here are the first demonstration of potential dependent dehybridization of MBs on single CNFs. Historically, MBs in solution[11-13] and as molecules attached to planar electrodes[14] are well studied, but the behavior of MBs on the ends of single CNFs is not well researched. In these experiments, many different and exciting conclusions were drawn.

5.2 Experimental

All of the chip preparation for the potential dependent dehybridization of ssDNA studies was performed by Qin Li and Lateef Syed from the Li group. The details of the sample preparation are found below.

5.2.1 Metal Catalyst Deposition

The first step in VACNF fabrication involves sputter coating a silicon wafer with chromium and nickel. This is accomplished with a Gatan ion beam sputter coater. Clean silicon wafers are coated with 50 nm of chromium and 22.5 nm of nickel using an ion beam with an energy of 10.0 keV. The sample is rotated at 35 rpm, tilted at 5^{o} and rocked at a rate of 12 ^{o}/s. This produces a coating rate of 1.2 Å/s for chromium and 0.6 Å/s for nickel.

5.2.2 Carbon Nanofiber Growth

After the metals are deposited, vertically aligned carbon nanofibers (VACNFs) can be grown on the coated silicon wafer. Fiber growth is accomplished using an Aixtron Black Magic plasma enhanced chemical vapor deposition (PECVD) system. First, the nickel catalyst coated in the previous step is annealed at 500 ^{o}C for 60s. Then, the wafer is exposed to C_2H_2 and NH_3 with flow rates of 63 and 250 sccm, respectively. The sample is then heated to 800 ^{o}C while the plasma is started (40 W drive). Once at temperature, fiber growth occurs for 15 min. This process yields a VACNF array with fiber diameters of 50 – 100 nm and lengths of ~5 μm, as verified by SEM.

5.2.3 SiO_2 Encapsulation

In order to provide mechanical stability to the array and to insulate the fibers everywhere but at their ends, the fibers are coated with SiO_2 using chemical vapor deposition (CVD) system in a home built system with a tube furnace from Thermo Electron Corporation. After evacuating the chamber to <100 mTorr, the chamber is

heated to 715 ^{o}C. Tetraethoxysilane (TEOS) is bled into the chamber at ~400 mTorr. Deposition occurs for 6 h to yield carbon nanofibers that are fully encapsulated in TEOS.

5.2.4 Molecular Beacons

The probe molecules used in these studies are a combination of a fluorophore, a quencher and ssDNA. On the 5' end, a molecule of 9'-(9H)xanthene)-6-carboxylic acid (FAM 6) is attached. On the 3' end, an amide/$(CH_2)_7$ group is present to provide a means to attach the MB to a VACNF. Also on this end, the Dabcyl dT is included as a quencher for the FAM 6. In order to fine tune the dehybridization of the MBs on single VACNFs, several different molecular beacons were used. The loop portions of the different MBs are identical, while the probe regions (underlined portion) contain different numbers of bases. The sequence of each strand is shown in Figure 5-2.

6-FAM-AAGAACAGCAAAGAGCAAGCTTCTT-Dabcyl-dT-AminoC7-3'
6-FAM-AAGAAGAAGACAGCAAAGAGCAAGTCTTCTTCTT-Dabcyl-dT-AminoC7-3'
6-FAM-AAGAAGAAGAAGAAGCAGCAAAGAGCAAGCCTTCTTCTTCTTCTT-Dabcyl-dT-AminoC7-3'

Figure 5-2 The sequences of the molecular beacon molecules employed in these studies is shown here.

5.2.5 Attachment of Molecular Beacons to Carbon Nanofibers

Finally, the silica coated VACNF array is polished with 1 μm alumina particles for 3-4 h. After rinsing with DI water, the chip is chemically etched with 1M NaOH while applying a potential of 1.5 V for ~30 s. This process is necessary to expose the distal ends of the carbon nanofibers. Once this is accomplished, a solution is prepared of 52.2 mM 1-ethyl-3-(3-dimethylaminopropyl) carbodiimide hydrochloride (EDC) and 23.0 mM sulfo-N-hydroxysulfosuccinimide (NHS) dissolved in 0.01 M phosphate buffered saline (1x PBS) containing 0.138 M NaCl, 2.7 mM KCl with pH 7.4. Then 25

μL of 10 μM MB in PBS is mixed with 25 μL of the PBS/NHS/EDC solution. Functionalization is accomplished by placing this solution on the chip, which is kept in the dark at 40 ^{o}C for 24 hours.[5,14,15] Following functionalization, the chip is rinsed with deionized water. Finally, after all sample preparation procedures a fully functionalized CNF array, shown in Figure 5-3, is obtained. Here a single CNF is shown with folded and unfolded ssDNA molecules attached. Depending on the stem length, a small fraction of the MBs may be dehybridized at room temperature (see Figure 5-3). The hybridized/dehybridized populations are expected to follow a Boltzmann Distribution.

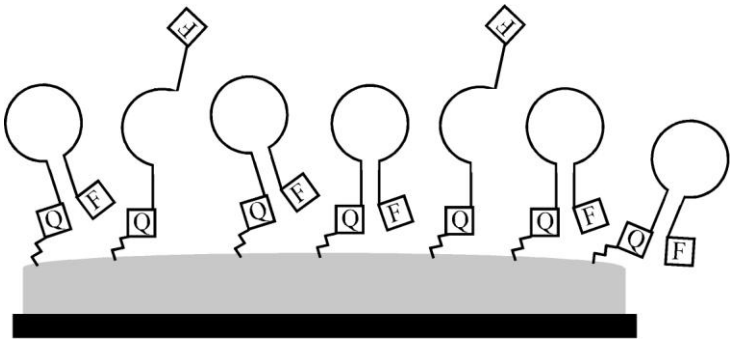

Figure 5-3 After the CNF array has been synthesized and encapsulated, the molecular beacons (hairpins) are attached. Pictured here the tip of one CNF (gray) embedded in TEOS (black). The molecular beacons at room temperature are mostly folded. A small number of open beacons are observed at room temperature due to a Boltzmann Distribution.

5.2.6 Cell Design

In order to understand the potential dependent dehybridization process, the CNF array is included in an electrochemical cell. The chip acts as the working electrode through which electrochemical experiments are run. To simultaneously monitor the electrochemistry in the cell and detect the fluorescence from the FAM-6 labeled MBs, an elegant cell had to be designed. The cell, provided by Prof. Bruce Gale's group at the

University of Utah and pictured in Figure 5-4, is made up of multiple layers of glass and PDMS. A microscope slide (gray, top and bottom) is first patterned with chrome wires (heavy black lines, bottom) that extend from the middle of the chip, where the electrochemical cells (circles, bottom) are, to the ends of the slide. At this end, the connection end, of these wires, the reference and counter electrodes from the potentiostat are connected. In the electrochemical cells, at the opposite ends of the wires, small dots of silver and platinum are placed to serve as the pseudo-reference and counter electrodes, respectively. A thin piece of PDMS (diagonal pattern, top and bottom), which has been previously patterned to form the solution cell and microfluidic channels (clear channels) is then placed onto the microscope slide on top of the wires. Additionally, larger PDMS blocks are added to the chip at the ends of the microfluidic PDMS chip to provide an easy means to attach tubes for solution delivery.

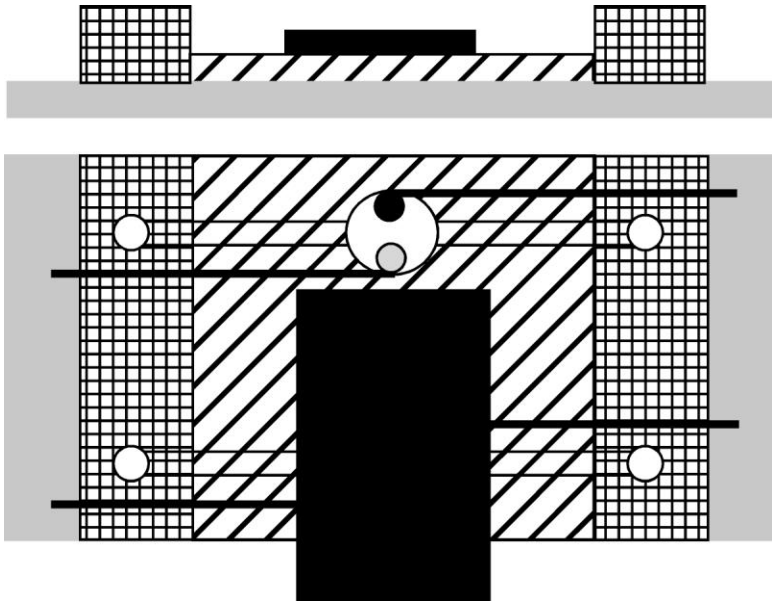

Figure 5-4 In order to probe the potential dependent dehybridization of the MBs, a small microfluidic chip is employed. Here, both the side view (top) and top view (bottom) are displayed. In the top, the substrate (gray) supports a thin PDMS layer (diagonal pattern) that contains the electrochemical cells and microfluidic channels

for buffer delivery. To feed solution into the channels, a large block of PDMS (grid) is attached to the chip to act as tubing connectors. Finally, the CNF array (black) is attached to the top of the thin PDMS layer. From the top we can see the same set-up. Here it is also possible to see the silver reference (gray circle) and the platinum counter (black circle) electrodes contained inside the electrochemical cell (white circle, center). Each of the wires (heavy black lines) connect the electrodes to external connections. The CNF array silicon wafer (black) is then laid over one of the electrochemical cells. An electrode is attached to the portion extending over the side of the chip to complete the working electrode.

Finally, the functionalized silicon wafer (black, top and bottom) is attached to the PDMS chip, by pressing firmly into position. The channels seal themselves by adhesion of the PDMS to the silicon wafer. When oriented properly, as in Figure 5-4 top, the electrochemical cell makes a window through which a microscope objective can interrogate the chip.

5.2.7 Bulk Fluorescence

In order to verify proper functioning of the MBs, solution-phase melting curves were obtained.

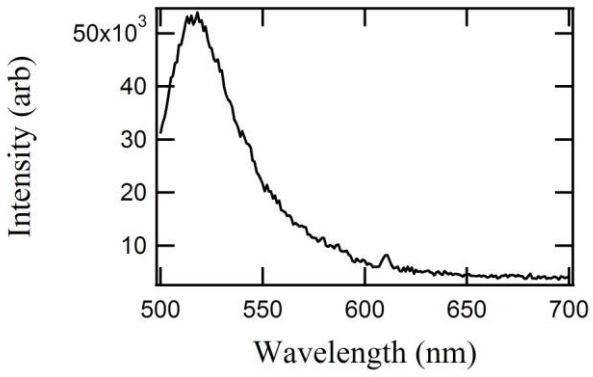

Figure 5-5 In order to characterize the melting curves of the molecular beacons, bulk spectra were obtained as shown here.

A commercial fluorescence spectrophotometer (Spex Fluoromax 2) was used to monitor the fluorescence of the MB solutions while the temperature was varied over an approximately 80^{o}C range (7 ^{o}C to ~85 ^{o}C). The temperature was altered using a water bath (Neslab). Water from the bath was pumped into a home built cuvette holder and water jacketed cuvette. Excitation was accomplished using 488 nm light. Both excitation and emission slits on the instrument were set to a 2 nm spectral bandpass. Spectra were obtained from 100nM MB solution in 0.2x PBS buffer with 1mM $MgCl_2$. The latter was added because it is known to stabilize the dehybridized MB.[1,12-14] Solution emission was recorded from 500-800 nm, with a 1 nm increment and an integration time of 0.1 s per data point.

5.2.8 Microscope Set-Up

As with all the other experiments in this dissertation, a Nikon (TE 300) microscope was employed. In all experiments, sample excitation was accomplished using light from a solid state laser (488 nm). A 488 nm laser line filter was used to ensure the removal of other laser lines from the excitation light. An appropriate dichroic beamsplitter (Chroma Z505RDC) was employed. An air objective (Nikon fluor, 0.55 numerical aperture, 50x magnification), produced a nearly diffraction limited focus of ≈ 540 nm $1/e^2$ radius in the sample and was used to excite the fluorophores and also collect their fluorescence. In all experiments, the incident laser power was maintained at 3 μW (estimated from measurements made external to the microscope). Finally, a 488 nm holographic notch filter was added between the output of the microscope and all other detectors and optics. For imaging and time transients, the light also passed through a 535 nm bandpass filter having a 50 nm passband. For these experiments the single-photon-

counting avalanche photodiode described above, section 2.1, was used as the detector. For spectra, the light passed only through the holographic notch filter before entering the spectrograph (Acton Research) and a liquid nitrogen cooled CCD (Princeton Instruments).

5.2.9 Potential Dependent Dehybridization Experiments

In order to monitor the potential dependent dehybridization of MBs functionalized onto single CNFs, individual CNFs were first located in the microscope by recording a fluorescence image of a 20 x 20 μm region. Individual CNFs were then selected and positioned, one at a time, in the focus of the microscope. MB fluorescence was then monitored over time (i.e., by recording a time transient). The bin time was varied between experiments, but was most commonly set to 100 ms/bin. While simultaneously monitoring the fluorescence of the MB, electrochemical potentials are applied to the working electrode (i.e., the CNF array). Initially, the cell was maintained at the open circuit potential (OCP) in the dark. The shutter was opened at the start of the experiment and the potential was immediately stepped from OCP to a negative potential, commonly -0.8 V. This potential was chosen because it allowed for the greatest magnitude in potential without electrolyzing the buffer in the cell. The potential was maintained at this value for a user-defined timeframe, commonly 30 s, referred to here as the pulse width. After the pulse width was achieved, the potential was instantaneously stepped to a positive potential that was equal in magnitude to the previously applied negative potential (in this case 0.8 V). This potential was then maintained for another 30s. This process was repeated a user-defined number of times (typically 5). After completion of the experiment, the cell was returned to the OCP. In many cases, photobleaching was found

to be a complicating factor in monitoring the dehybridization process. To minimize its effects, the shutter was often maintained in a closed state and briefly pulsed open for 2 s at the end of the pulse width. The other settings for the potentiostat are summarized in Table 5-1.

Initial E	OCP
High E	+ 0.8 V
Low E	- 0.8 V
Initial Step	Negative
Steps	5
Width	30 s
Sample Interval	0.01
Quiet Time	0 s
Sensitivity	1e-5

Table 5-1 Common settings for the potentiostat used in the potential dependent dehybridization studies. These parameters are a basic setting and can be changed to accommodate different experimental conditions. However, caution must be excercised in setting the sensitivity to any other value, as many other settings cause electrical errors and will ruin the device.

5.3 Results and Discussion

5.3.1 Molecular Beacon Melting Curves

In order to fully understand the properties of all of the MBs during the dehybridization process, bulk melting curves were obtained. Here, solutions of MB were dissolved in 0.2x buffer to mimic the conditions inside the electrochemical cell on chip. The temperature of the solution was changed from ~7 ^{o}C to ~85 ^{o}C. The fluorescence spectrum at each temperature was collected and integrated. The integrated intensities of all solutions at each temperature are shown in Figure 5-6.

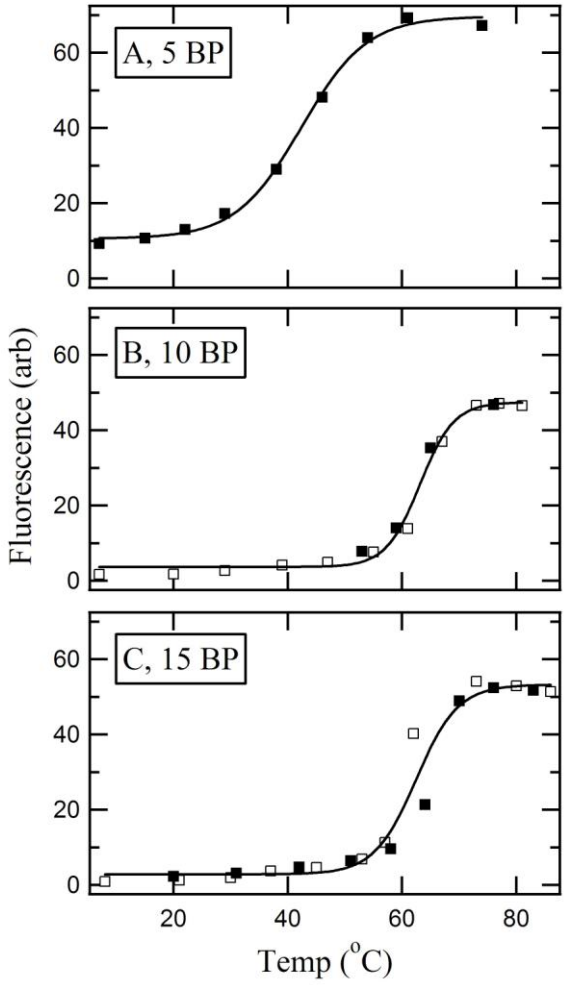

Figure 5-6 Here melting curves of MBs having stem lengths of 5 (top), 10 (middle) and 15 (bottom) bases are shown. The inflection point of the sigmoidal curve shows the approximate location of the melting point. Filled squares show data obtained from heating the MB from a low temp, while open squares show data obtained from cooling the MB from a high temperature.

The curves show some interesting features, the most striking being the 5 Base Pair Stem Length (BPSL) MB solution has the highest fluorescence intensity at low temperatures. This is most likely due to the fact that there are significantly more molecules, as compared to the 10 and 15 BPSL curves, that are unfolded at these temperatures. This is due to the fact that the overall bond strength of the 5 BPSL MB is

weaker than those of the 10 and 15 BPSL whose fluorescence is almost identical at low temperature. The melting temperature of the MB can be determined by estimating the inflection point of the sigmoidal curve of the data.[12] This analysis shows that the 10 and 15 BPSL MBs unfold at a higher temperature than the 5 BPSL MB. This provides further evidence of the fact that the overall bond strength of the 10 and 15 BPSL MBs is stronger than that of the 5 BPSL MB. This behavior is intuitive since the 10 and 15 BPSL MBs have a greater total bond energy, assuming constant bond energies for both G-C and A-T bonds, than the 5 BPSL MB. Additionally, the inflection point of the sigmoidal curve of the 5 BPSL MB shows a broad transition from low intensities to high intensities. This suggests that the 5 BPSL MB has a less specific melting temperature due to the weakened overall bond strength. Conversely, the 10 and 15 BPSL MBs unfold in a step-wise fashion at a very narrow temperature range. Melting curves obtained from heating the MB solutions and also from cooling previously heated MB solutions overlap well which indicates that there is little hysteresis in the system indicating good reversibility. These results are important for experiments performed in the fluidic device.

The dehybridization process on the chip occurs by electrostatic repulsion of the charged ssDNA backbone from the electrode surface. The rehybridization process occurs in a similar manner, but results from attraction of the ssDNA backbone towards the positive electrode surface. These interactions are analogous to increasing and decreasing, respectively, the temperature of the solution. Understanding which MB dehybridizes at what types of energy input will help to design the on chip experiments. Ideally, complete dehybridization of all CNF bound MBs would occur by switching the potentials across a very narrow range. The results of the bulk melting curves indicate that the 5 BPSL MB is

not a good MB to fufill this criteria. In addition, the 10 and 15 BPSL MBs have higher contrast ratios and lower background fluorescence intensities at low temperatures. Both of these characteristics make 10 and 15 BPSL MBs suitable for on-chip use.

Finally, close inspection of the 10 and 15 BPSL MB melting curves (Figure 5-6 middle and bottom, respectively) shows that the 10 BPSL MB melts at a lower temperature than the 15 BPSL MB. This is due to the fact that loop of the 10 BPSL MB contains one less base than the other MBs. This results in a deviation from the trend that more bases in the stem yields a higher melting temperature. These results are also verified by simulations.[16]

5.3.2 Imaging and Spectra

To better understand the localization and surface coverage of the MBs on the CNF array, fluorescence images obtained from raster scanning experiments with the microscope set-up described in section 5.2.8 were collected. Images were obtained to locate individual CNFs to obtain their MB spectra and to record potential dependent dehybridization time transients. Images of CNF arrays without MB give images like that shown in Figure 5-7A.

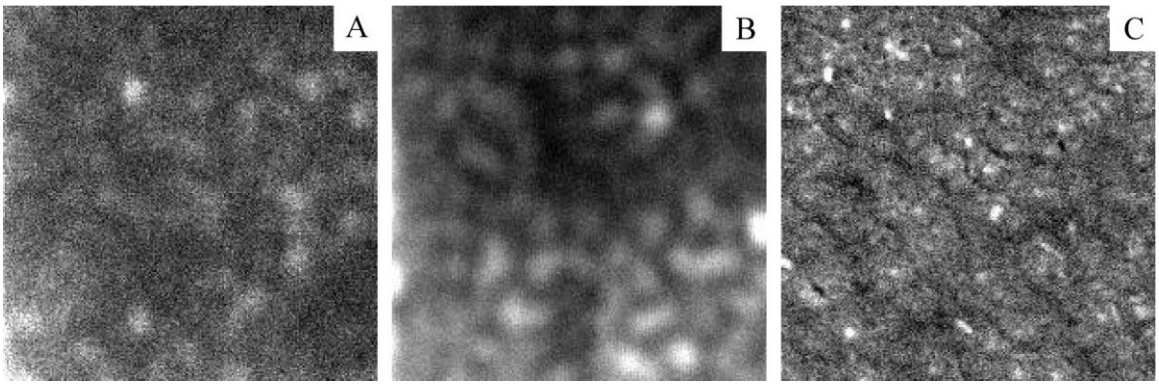

Figure 5-7 Luminescence images obtained from a blank (A) and MB functionalized (B) CNF array (showing ~20 and ~60 fibers respectively) is displayed. An SEM

image (showing ~60 fibers) of an approximately equivalent area (obtained by Lateef Sayed) is shown in (C). The image size is 20 x 20 µm. The intensity scale in counts/pixel extends from 27-106 for (A) and 530-1193 for (B).

In Figure 5-7A, low intensity (~100 counts/pixel) spots are obtained which, are due in part to auto-fluorescence of the CNFs, but mostly from scattered excitation light and contaminant emission. Conversely, functionalized CNF arrays produce images like that shown in Figure 5-7B. Here, the intensity is much higher (~500 counts/pixel) consistent with the presence of MBs. Interestingly, these images are typical for MB functionalized CNF arrays at room temperature and without applied potentials. This corresponds to the minimum fluorescence intensity collected from MBs in solution at low temperature.

The images obtained from microscopic analysis also correlate nicely with Scanning electron microscopy images obtained by Lateef Sayed, see Figure 5-7C. The quantity of spots (Figure 5-7A,B) and fibers (Figure 5-7C) are approximately equivalent. Cross correlation analysis of the image, analogous to those performed in Chapters 3 and 4, with a kernel having a 5 pixel radius, correlation values between 0.3 and 1 and areas from 1 to 999 pixels, yields ~20 fibers for the blank array (Figure 5-7A) and ~60 fibers for both Figure 5-7B and C.

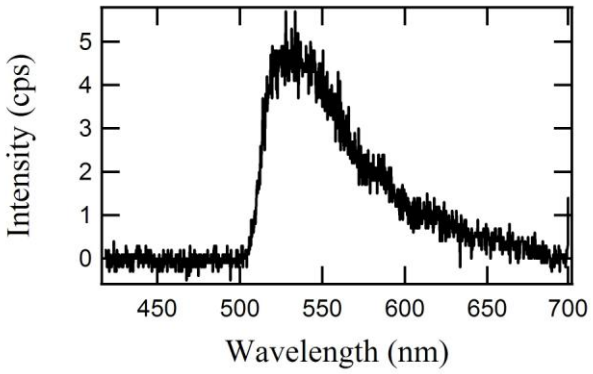

Figure 5-8 The fluorescence spectrum of FAM-6, the fluorophore attached to the MB, is displayed. This spectrum was obtained with an integration time of 10 s.

Additionally, fluorescence spectra of MB-functionalized single CNFs were used to verify the presence of MB and to validate the functionalization procedure. To do this, the sample was moved to a user-defined position, where fluorescence can be detected. The fluorescence spectrum obtained from a bright spot like that shown in Figure 5-7B is shown in Figure 5-8. The peak is centered at ~535 nm, which corresponds well with the bulk spectra obtained from the MBs, see Figure 5-5. The asymmetric peak shape is due to the throughput of the microscope and dichroic beamsplitter employed.

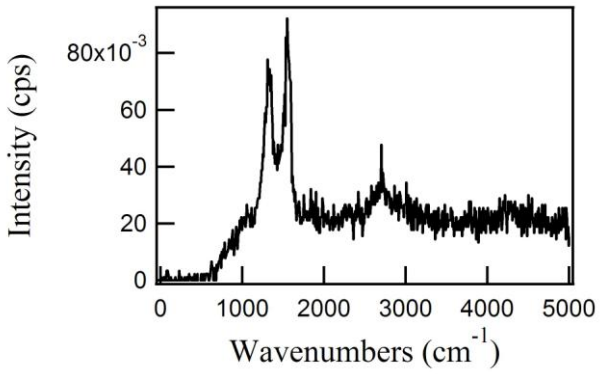

Figure 5-9 Shown here is a spectrum of Raman scattering obtained from an as-grown CNF array. This spectrum was obtained with an integration time of 15 min.

Finally, the typical spectra of spots from blanks like that shown in Figure 5-7A is significantly different from spectra obtained from the unfunctionalized and/or non encapsulated CNF arrays. A typical spectrum from these samples (Figure 5-7C) is shown in Figure 5-9. These spectra are dominated by Raman scattering from the CNFs. Additionally, the sharp peaks observed in these spectra correspond well with the D and G bands, which occur at ~1350 cm^{-1} and ~1580 cm^{-1} respectively, from previously published Raman spectra of non encapsulated CNF arrays.[17]

5.3.3 Time Transients

In addition to fluorescence imaging and spectra, fluorescence time transients are useful in determining the source of the emission from MB-labelled CNFs. If a functionalized CNF array is maintained at room temperature, under buffer, with no potentials applied to the system, the emission of the MBs shows a slow double exponential decay, with τ_1 = 250 s and τ_2 = 33 s, of fluorescence which is attributed to photobleaching. The emission starts at some high intensity and quickly decays to background. The decay is roughly exponential, which indicates that there are multiple fluorophores in the excitation volume simultaneously. This behavior is indicative of irreversible photobleaching of the fluorophores in the sample. It further validates the hypothesis that the signal obtained from functionalized CNF arrays is not due to scattering from the fibers. If the emission were due to scattering, the intensity of the emission would not decay quickly over time as observed, but would instead remain constant in time. This behavior would only be observed in the absence of other effects such as heating. If the fibers efficiently absorb much of the laser light irradiating the sample, then they could likely heat and bend causing fluctuations in the signal in time. However, calculations which account for the heat capacity of the buffer and the amount of heat generated by the laser beam, show that this is not likely.

After characterizing the MBs as above, the potential dependent dehybridization studies could be performed. These experiments require continuously monitoring the fluorescence of the MBs while simultaneously varying the electrochemical potentials. Results of an experiment of this kind are shown in Figure 5-10. Here, the potentials applied to the system (versus the quasi Ag/AgCl reference electrode) are shown in gray,

while the fluorescence from the MB is shown in black. The experiment proceeds as described in Section 5.2.9. Several important conclusions can be drawn from this data. First, the time constant for the rate of fluorescence decay, $\tau = 100$ s, for each positive potential step is much shorter than that obtained from MB photobleaching. This indicates that the intensity decrease in the signal, for each positive potential step, is not due to photobleaching of the MB. Unfortunately, the affects of photobleaching are observed over the course of the entire time transient. The overall decrease in signal from ~4400 to ~3800 counts is due to irreversible photobleaching of the MB as discussed in Section 5.3.3. To help minimize photobleaching, all experiments were performed under a nitrogen atmosphere with nitrogen purged solutions. These treatments minimize the oxygen in the system and hopefully, bleaching. Unfortunately, even with these precautions, photobleaching is impossible to completely remove from the experiment.

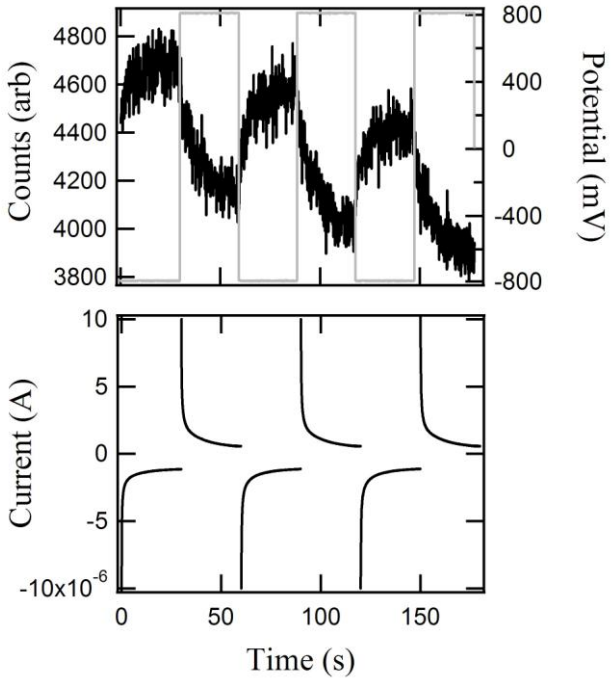

Figure 5-10 Here a time transient obtained from a potential dependent experiment is displayed (top). The fluorescence intensity trace (black) shows fluctuations that

correspond to the applied potential trace (gray). The potentials shown here are versus the quasi Ag/AgCl reference electrode. In addition, the corresponding chronoamperometry data (bottom) is displayed.

Importantly, the data in Figure 5-10 (top) show that the potential dependent opening/closing is very reversible. The fluorescence fluctuations for each of the potential steps are approximately equal in magnitude, indicating that the original intensity is reattained (after accounting for photobleaching) with every potential cycle. This is important to the lifetime of the chip. The dehybridization process must be reversible in order for one device to be used for multiple analyses.

In addition, examination of the chronoamperometry data, Figure 5-10 bottom, associated with this particular experiment shows another important detail. In these experiments, the only current produced from the applied potentials should be due only to formation of the electrical double layer. Specifically, this charging current results from the movement of ions in the supporting electrolyte towards or away from the fiber. This current should decay quickly, with $\tau = 0.5$ s. This charging current should not result in any change in the fluorescent signal since there should be no redox chemistry occurring.

Fluorescence	
Rising	Falling
5.3±0.2	9.7±0.8
Current	
Negative	Positive
τ_1	τ_1
0.38±0.07	0.49±0.08
τ_2	τ_2
5.2±0.3	7.4±0.5

Table 5-2 Here time constant values (s) of exponential fits to both fluorescence and current data from time transient experiments are shown. The fluorescence data is

easily fit to single exponential decays in both rising and falling portions of the data. However, the timescales of the processes are different. Additionally, the current data is fit to a double exponential function with both a very fast and a slow component. The slow component of negative currents corresponds to the timescale of the fluorescence rises.

Analysis of the exponential decays of the fluorescence and double exponential decays of the current, Figure 5-10, associated with the time transients, Table 5-2, shows that there is a correlation between the slow component of the current and both rising and falling fluctuations in the fluorescence. This indicates that there may be some electrochemical enhancement and degradation of the fluorescent signal occurring for the rising and falling fluorescence fluctuations, respectively. The fast current decays, ~0.5 s, show no correlation with fluorescence but most likely correspond to the charging of the double layer. In addition, it should be noted that this behavior is site specific. In the analysis of other data sets, the correlations observed in Table 5-2 are not observed.

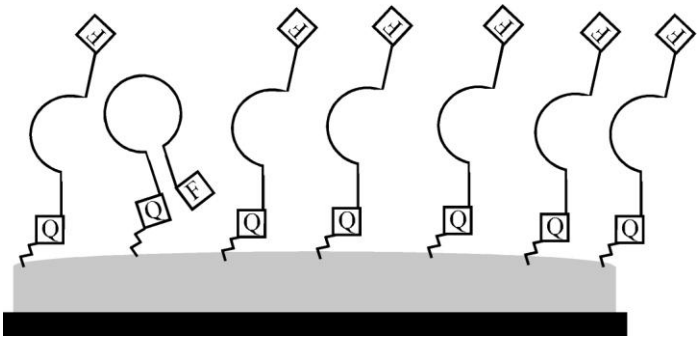

Figure 5-11 When a negative potential is applied to the functionalized CNF array, the MBs dehybridize causing the fluorophore (F) to move away from the CNF and quencher (Q).

The model for how this process occurs is straightforward. At room temperature, most of the ssDNA molecules, following a Boltzmann-like Distribution, are folded as in Figure 5-3. In this instance, the fluorophore and quencher are in close proximity to each

other, thus no fluorescence is obtained. When a negative potential is applied to the CNF, the resulting electric field repels the negative charges on the backbone of the MB, causing the molecule to dehybridize. This process then results in opening of the MBs, as in Figure 5-11. Separating the fluorophore from the quencher allows fluorescence to occur. This model explains the potential dependent quenching of the MB which accounts for the fluorescence fluctuations detected in the time transients. Again, the process is reversible, so when the potential is stepped back to a positive value, the field attracts the negative charges on the backbone, bringing the fluorophore and quencher together again, quenching the fluorescence.

Unfortunately, each MB-labeled CNF chip can only be used for a very limited number of potential dependent dehybridization studies. A significant decrease in fluorescence was observed from the entire chip over the course of only 10-15 potential cycles (i.e. -0.8 to +0.8 V). The fluorescence was found to be greatly reduced, even in regions that had not previously been exposed to laser light. We attribute this behavior to some long term electrochemical destruction of the MBs, possibly due to redox reactions of either the CNF-MB linker or the FAM-6. In the former case, the MBs could be released from the CNF surface. In the latter case, the fluorescence intensity would decrease due to chemical changes of the dye. For now, this is an unfortunate limitation of these devices in their current state.

In addition, the lifetime of these devices is severely limited for single fiber analysis by contamination. In all cases, the CNF array is robust enough to allow for its re-use in subsequent analyses. Polishing to remove the used MB and re-functionalizing the chip yields a new device very quickly. However, over time the chip adsorbs a lot of

contaminant from contacting solutions and surfaces. This is most likely due to the fact that carbon is an excellent adsorbent of contaminants. The CNFs adsorb and store many contaminants, particularly organic molecules, that they come into contact with. This is analogous to the behavior of activated charcoal in commercial water filtration systems. Over time, the background of the array builds up to a level that makes the chip unusable for microscopic analysis.

5.4 Conclusions

In these studies, the potential dependent dehybridization of MBs attached to single CNFs was explored for the first time. Bulk analysis of melting curves of MBs show that increased numbers of bases in the stem length lead to sharper transitions from folded to unfolded conformations. Also, the energy required to cause dehybridization increases with increasing numbers of bases in the stem of the MBs, indicating that the overall bond strength of the 10 and 15 BPSL MBs is greater than that of the 5 BPSL MB. These studies were used to confirm the beacon function. In addition, a CNF array was fabricated with MBs functionalized onto the ends of single CNFs. Potentials were then applied to the functionalized CNF array in an electrochemical cell contained on a microfluidic device. This configuration enabled the visualization of potential dependent dehybridization of the MBs on a single CNF through a microscope for the first time. It has been shown that a strong correlation exists between the applied potentials and fluctuations in the fluorescence signal. The rate at which these fluorescence fluctuations occur is faster than the time scale of fluorescence photobleaching, indicating that there are electrochemical processes which cause dehybridization of the MBs. We hypothesize that the processes responsible for the fluorescence fluctuations are de/rehybridization of

the MBs and that this is caused by electrostatic repulsion and attraction of the negative backbone of the MB. The folding and unfolding caused by these interactions moves the fluorophore and quencher molecules away from and in proximity to each other, respectively. These actions are the source of the fluctuations observed in the described time transient experiments. These experiments are the first demonstration of potential dependent dehybridization of MBs functionalized onto single CNFs. In the future, this technology will be used to detect harmful bioorganisms in foodstuffs and other samples before a hazardous outbreak occurs. Continued work is necessary to understand the mechanisms by which these devices are fouled.

5.5 Chapter 5 References

(1) Bonnet, G.; Tyagi, S.; Libchaber, A.; Kramer, F. R. *Proc. Natl. Acad. Sci.* **1999**, *96*, 6171–6176.

(2) California Food Emergency Response Team; California Department of Public Health, 2007.

(3) Associated Press. In *MSNBC*, 2006.

(4) Dyckman, L. J.; Office, Gen. Acc., Ed., 2001.

(5) Wolter, A.; Niessner, R.; Seidel, M. *Anal. Chem.* **2008**, *80*, 5854–5863.

(6) Yang, L.; Bashir, R. *Biotechnology Advances* **2008**, *26*, 135–150.

(7) Umek, R. M.; Lin, S. W.; Vielmetter, J.; Terbrueggen, R. H.; Irvine, B.; Yu, C. J.; Kayyem, J. F.; Yowanto, H.; Blackburn, G. F.; Farkas, D. H.; Chen, Y.-P. *Journal of Molecular Diagnostics* **2001**, *3*, 74-84.

(8) Boon, E. M.; Salas, J. E.; Barton, J. K. *Nature Biotechnol.* **2002**, *20*, 282-286.

(9) Heaton, R. J.; Peterson, A. W.; Georgiadis, R. M. *Proc. Natl. Acad. Sci.* **2001**, *98*, 3701–3704.

(10) Vainrub, A.; Pettitt, B. M. *Biopolymers* **2003**, *68*, 265–270.

(11) Darby, R. A. J.; Sollogoub, M.; McKeen, C.; Brown, L.; Risitano, A.; Brown, N.; Barton, C.; Brown, T.; Fox, K. R. *Nucleic Acids Res.* **2002**, *30*, e39.

(12) Schofield, P.; Pell, A. N.; Krause, D. O. *Appl. Environ. Microbiol.*, **1997**, *63*, 1143–1147.

(13) Tsourkas, A.; Behlke, M. A.; Rose, S. D.; Bao, G. *Nucleic Acids Res.* **2003**, *31*, 1319-1330.

(14) Wei, F.; Qu, P.; Zhai, L.; Chen, C.; Wang, H.; Zhao, X. S. *Langmuir* **2006**, *22*, 6280-6285.

(15) Wei, F.; Sun, B.; Guo, Y.; Zhao, X. S. *Biosens. Bioelectron.* **2003**, *18*, 1157-1163.

(16) Zuker, M., http://www.idtdna.com/analyzer/Applications/OligoAnalyzer/, 2009.

(17) Chuang, C.-C.; Liu, W.-L.; Chen, W.-J.; Huang, J.-H. *Appl. Surf. Sci.* **2008**, *254*, 4681–4687.

6 Conclusions and Future Directions

6.1 Conclusions

In this dissertation, single molecule methods have been used to probe the mobility and entrapment of dye molecules as a function of solvent loading and oligomer extraction in PDMS films. It has also been shown how ssDNA can be dehybridize from a single carbon nanofiber using electrochemistry. All of these projects work to provide an understanding of materials and mechanisms of fundamental transport of single molecules in the hopes that other researchers will be able to use the results we have obtained to better engineer materials and devices.

6.1.1 Single Molecule Studies of Solvent-Dependent Diffusion and Entrapment in Poly(dimethylsiloxane) Thin Films

Single molecule imaging and single point fluorescence time transient measurements have been used to characterize the diffusion and entrapment of the uncharged dye BPPDI in cured PDMS films under dry and IPA loaded conditions. The results show that the population of mobile BPPDI molecules is strongly dependent upon IPA loading but that the rate of molecular motions, as reflected in the diffusion coefficients obtained, is not. Furthermore, a nonzero population of immobile molecules is found in the films even at the highest IPA loadings. The population of immobile molecules is also shown to depend upon whether the dye was originally cast with the PDMS precursor, prior to curing or added to the film after curing. These observations are

attributed to physical entrapment of the dye within PDMS film micropores under dry conditions. Dye mobility at intermediate and high IPA loadings results not from a solvent-induced decrease in PDMS film viscosity but rather from the formation of solvent-filled micropores. However, even under IPA saturated conditions, some BPPDI molecules are found to be immobile, reflecting the presence of some isolated micropores within the PDMS.

The results obtained provide a better understanding of how dye molecules move through and interact with the PDMS matrix. Along with the methods employed, they promise to aid in the development of PDMS chips for microfluidic separations, PDMS membranes for vapor phase extraction and pervaporation processes, and PDMS fibers for solid phase microextraction. Future work will include exploration of ionic interactions between charged molecules with the PDMS matrix and investigation of ways in which to block the adsorption of small organics, perhaps by filling the open pore volume of the matrix.

6.1.2 Single Molecule Studies of Oligomer Extraction and Uptake of Dyes in Poly(dimethylsiloxane) Films

Bulk and single molecule fluorescence methods have been used to explore the impacts of oligomer extraction on the properties of cured PDMS films. Both neutral and cationic fluorescent dyes were employed. Quantitative counting of fluorescent spots in images of dye-doped PDMS showed that the absolute populations of fixed molecules increased with increasing oligomer extraction for both BPPDI- and R6G-doped samples. Likewise, the total population of mobile molecules was also observed to increase with oligomer extraction in both cases, as was the population of mobile molecules. The single

molecule results indicated the BPPDI and R6G concentrations in the films increased by 120 % and 70 %, respectively, across the range of films studied. Bulk R6G fluorescence results obtained on PDMS monoliths provided further proof that the dye concentration within the PDMS increased with the extent of oligomer extraction. In contrast to the absolute populations, the relative populations of fixed and mobile molecules were observed to decrease and increase, respectively, consistent with an extraction-dependent increase in the mobility of the molecular dopants. The observed extraction-dependent increase in the diffusion coefficient for BPPDI provided further evidence of an increase in molecular mobility. A model was developed to describe these extraction-dependent changes in materials properties. It was concluded that extraction of the low molecular weight oligomers affords increased open void volume within the PDMS, allowing PDMS chain ends to become more mobile. The greater open void volume and increased PDMS chain mobility affords greater dye loading, and greater dye mobility while simultaneously leading to a reduced population of voids having an appropriate size to trap the dye molecules.

The data presented here clearly show that the concentration of small organic molecules that can be loaded into PDMS films depends on the degree to which low molecular weight oligomers have been extracted from the samples. These results are of significance for any technique that utilizes PDMS as an extraction or separation medium. In applications where the absorption of small organics is desired (i.e., solid phase microextraction and pervaporation) oligomer extraction represents a simple means to increase the uptake of organics. In addition, the mobility of molecules incorporated in the PDMS increases with the extent of extraction, providing a means to increase the

speed of such applications. Conversely, the present results also suggest that the extraction procedures commonly used to increase the hydrophilicity of PDMS microfluidic chips may result in loss of analyte by increased absorption into the PDMS, thus hurting important figures of merit for PDMS based microfluidic separations. Finally, partially extracting unreacted low molecular weight oligomers from PDMS nanofiltration membranes allows for tenability of the pore size of the PDMS.

6.1.3 Potential Dependent Dehybridization of ssDNA Hairpins Functionalized on a Carbon Nanofiber Array

Potential dependent dehybridization of molecular beacons (MBs) at the ends of single CNFs has been observed for the first time. Bulk analysis of the melting curves of the MBs show that increased numbers of linkers lead to sharp transitions from folded to unfolded conformations. In addition, a CNF array was fabricated with MBs functionalized onto the ends of the fibers. This configuration is the first experiment to perform these experiments on the ends of CNFs. Potentials applied to an electrochemical cell contained on a microfluidic device enabled the visualization of potential dependent dehybridization of the MBs through a microscope. It has been shown that a correlation exists between the applied potentials and fluctuations in the fluorescence signal. The rate at which these fluorescence fluctuations occur is also faster than the time scale of fluorescence phhotobleaching indicating that there are electrochemical processes which cause dehybridization of the MBs. In the future, this technology may be used to detect harmful bioorganisms in foodstuffs and other samples before an outbreak occurs. Continued work is necessary to understand the mechanisms by which these devices are fouled.

6.2 Future Directions

In all of the projects discussed in this dissertation, much work remains to be done. Suggestions for possible future experiments that may help answer many of the questions left unanswered are given below.

6.2.1 PDMS: Curing Agent to Polymer Ratio

An exhaustive analysis of what effect the curing agent to polymer ratio of Sylgard 184 mixtures has on the structure of cured PDMS would be valuable. This is an area where researchers already know that mixing a smaller ratio of the two components yields films that are very "sticky", but little information is known about the chemical interactions that occur that cause this behavior. As was observed in Chapter 4, these simple experimental parameters may lead to quite drastic changes in the PDMS properties. In this case, pore formation of the PDMS may change quite drastically. Small ratio mixtures may lead to extremely large pores, while large ratio mixtures may yield pores small enough that no probe molecule can be included.

6.2.2 PDMS: Curing Time/Aging Effects

Another fundamental experiment would include an exhaustive exploration of the curing time and aging effects of the PDMS process. In all cases presented here, the curing time was constant at 24 h, but it is uncertain if this time is necessary. Shorter curing times may yield films that are equivalent to those studied here. In addition, after the PDMS has cured initially, a long time scale curing process takes place. This process may again have dramatic impacts on the pore size of the polymer structure especially if extracted.

6.2.3 PDMS: Fluorescently Modified Chains

In another experiment it may be worthwhile to synthesize PDMS chains that have a fluorophore already included. This may prove tricky in practice to ensure that the concentration of fluorophore is not too high, but the information obtained could be extremely useful. If time transients are collected from films as they cure, an exact mechanism of pore and film formation may be obtained. More importantly, after the PDMS films have cured, it would be possible to measure the PDMS chain's motion due to thermal perturbations. Many simulations show PDMS to be quite flexible through the chain backbone, but this has not been observed experimentally.

6.2.4 PDMS: Transition Metal Films

Recently, as noted in Chapter 3, researchers have begun modifiying PDMS to become more resistant to adsorption/absorption of small molecules. Most notably this is done through the coating of PDMS interfaces with transition metal complexes.[1] This has been shown to block the uptake of small molecules from microfluidics channels, but the exact cause of this process is unknown. It would be interesting to learn if the mechanism of blocking the uptake of small molecules is due to some electrostatic interactions between the material and the single molecules, or if the transition metal complexes simply physically occupy the pores and open volume of the PDMS where uptake occurs. Understanding this process may yield less expensive, greener coatings of PDMS devices.

6.2.5 PDMS: Surfactant Films

Finally, researcher have shown that filling microfluidic channels with surfactants causes a spontaneous surface coating of the microchannel walls.[2] This is ideal for

microfluidics separations since the surfactants spontaneously orient themselves with the tails intertwined into the PDMS and the hydrophilic heads staying in solution. It would be interesting to find out what other effects this process has on the properties of the PDMS.

6.2.6 Potential Dependent Dehybridization of ssDNA

There is much information that needs to be learned about the basic mechanisms of potential dependent dehybridization of ssDNA inside the microfludic chip that is discussed. Through the course of the work presented here, it is obvious that the applied potentials damage the ssDNA molecules. The fluorescence intensity of images and time transients decays dramatically over short amounts of time. This effect is observed in all areas of the array, most notably areas that have not been irradiated before. Since this is the case, it is apparent that this behavior is not due to photobleaching, but to some other degradation process. Identification of this process will be crucial to ensuring that devices with long lifetimes are fabricated.

6.3 Chapter 6 References

(1) Roman, G. T.; Culbertson, C. T. *Langmuir* **2006**, *22*, 4445-4451.

(2) Roman, G. T.; McDaniel, K.; Culbertson, C. T. *Analyst* **2006**, *131*, 194–201.